

ASD-TDR-62-399

Husson

**STRESS WAVE PROPAGATION AND SPALLATION
IN UNIAXIAL STRAIN**

EFFECTS OF AIR IN BARREL Pg. 75

TECHNICAL DOCUMENTARY REPORT NO. ASD-TDR-62-399

September 1962

Pg 33

Directorate of Aeromechanics
Aeronautical Systems Division
Air Force Systems Command
Wright-Patterson Air Force Base, Ohio

pg 22

$$P = \frac{U_s U_p}{V_0} = U_s U_p \rho_0$$

Project No. 6906, Task No. 690601

$$\frac{V_0 - V_1}{V_0} = \frac{U_p}{U_s}$$

(Prepared under Contract No. AF 33(616)-6373
by Massachusetts Institute of Technology,
Cambridge, Massachusetts;
Walter Herrmann, Emmett A. Witmer, John H. Percy,
Aron H. Jones, authors)

20070921507

NOTICES

When Government drawings, specifications, or other data are used for any purpose other than in connection with a definitely related Government procurement operation, the United States Government thereby incurs no responsibility nor any obligation whatsoever; and the fact that the Government may have formulated, furnished, or in any way supplied the said drawings, specifications, or other data, is not to be regarded by implication or otherwise as in any manner licensing the holder or any other person or corporation, or conveying any rights or permission to manufacture, use, or sell any patented invention that may in any way be related thereto.

Qualified requesters may obtain copies of this report from the Armed Services Technical Information Agency, (ASTIA), Arlington Hall Station, Arlington 12, Virginia.

This report has been released to the Office of Technical Services, U.S. Department of Commerce, Washington 25, D.C., in stock quantities for sale to the general public.

Copies of this report should not be returned to the Aeronautical Systems Division unless return is required by security considerations, contractual obligations, or notice on a specific document.

FOREWORD

This report was prepared by Massachusetts Institute of Technology, Cambridge, Massachusetts, under USAF Contract AF 33(616)-6373. This contract was initiated under Project No. 6906, "Nuclear Weapon Effects on Space Vehicles," Task No. 690601, "Determination of High Altitude Nuclear Weapon Effects on Space Vehicles." The work was administered under the direction of the Directorate of Aeromechanics, Deputy Commander/Technology, Aeronautical Systems Division, Wright-Patterson Air Force Base, Ohio. Capt. Raymond B. Walker was the project engineer for the Laboratory.

This report covers work done from March 1959 to March 1962.

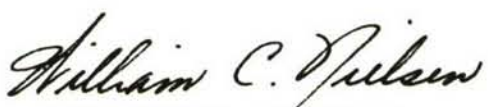
The authors are indebted to Dr. C. D. Lundergan of Sandia Corporation, Albuquerque, New Mexico for access to fracture and constitutive equation data. Programming of the finite difference method was carried out by Mrs. Margaret Korpi and Miss Margot O'Brien. The manuscript was ably typed by Mrs. Gertrude Hubbard. Computations were carried out in part at the MIT Computation Center, Cambridge, Massachusetts.

This report was prepared by the Aeroelastic and Structures Research Laboratory, Department of Aeronautics and Astronautics, Massachusetts, and is a part of the Air Force Systems Command applied research program 710A, "Nuclear Weapon Effects."

ABSTRACT

A discussion of the analytical methods of predicting uniaxial stress wave propagation and spall as a result of uniformly distributed intense impulsive loading is given. For the materials for which data currently exists, no strain-rate effects are observed on yield (i.e. two aluminum alloys) and the strain-rate effect on the fracture threshold is found to be small (copper). For such materials a detailed analytical treatment is possible, once the constants associated with the constitutive equation and fracture criterion are evaluated. The plate impact experiment provides a convenient means of evaluating these constants. Considerations entering into the interpretation of the plate impact experiment and a detailed analysis of the effect of air between the impacting plates are given.

This report has been reviewed and is approved.



WILLIAM C. NIELSEN
Colonel, USAF
Chief, Flight Dynamics Laboratory

TABLE OF CONTENTS

<u>Section</u>	<u>Page</u>
I Introduction	1
II Finite Difference Method	4
III Characteristics Method	14
IV Equation of State	21
4.1 Introduction	21
4.2 High Pressure Region	22
4.3 Low Stress Region	32
4.4 Medium Stress Region	41
V Examples of Wave-Propagation Calculations	44
VI Spall Fracture	49
6.1 Fracture Criteria	49
6.2 Summary	60
VII Effect of Air Between Impacting Flat Plates	62
7.1 Perfect Gas Analysis	63
7.2 Real Gas Analysis	69
7.3 Subsequent Wave Profiles	71
7.4 Summary	75
VIII Conclusions	78
References	80
Figures	35
Tables	121

LIST OF ILLUSTRATIONS

<u>Figure</u>		<u>Page</u>
3.1 Characteristic Net for Reflection at an Interface		85
3.2 Characteristic Net for Formation and Reflection of a Weak Shock		85
4.1 Elastic-Plastic Stress-Strain Schematic for Uniaxial Strain		86
4.2a Offset of the Hugoniot from the Adiabat in Pure Dilatation for 2024 Aluminum (from Fowles ¹⁷)		87
4.2b Offset of the Hugoniot from the Adiabat in Pure Dilatation for 6061-T6 Aluminum (from Lundergan ¹⁸)		88
4.3 Murnaghan Fit to the Dynamic Adiabat for Aluminum		89
5.1 Lagrangian Characteristic Mesh for Plate Impact		90
5.2a Wave Profiles at 2 μ sec After Impact. Copper Driver and Target Plates with an Impact Velocity of 12.6×10^3 cm/sec		91
5.2b Wave Profiles Continued. At 3 μ sec After Impact		92
5.2c Wave Profiles Continued. At 4 μ sec After Impact		93
5.2d Wave Profiles Continued. At 5 μ sec After Impact		94
5.2e Wave Profiles Continued. At 6 μ sec After Impact		95
5.2f Wave Profiles Concluded. At 7 μ sec After Impact		96
5.3a Comparison of Characteristic and Finite Difference Methods for Plate Impact Using the Murnaghan Equation		97

LIST OF ILLUSTRATIONS Continued

<u>Figure</u>		<u>Page</u>
5.3b	Concluded	98
6.1	Sections Through 1/4-inch-thick E.T.P. Half-Hard Copper Target Plates Struck by 1/8-inch-thick Driver Plates of the Same Material.	
	Ferric Chloride Etch	99
6.2	Tension Test Arrangement	100
6.3	Residual Strength of Spalled Targets	101
6.4	Spall Velocity as a Function of Driver Plate Velocity	102
6.5	Characteristic Mesh for the Elastic-Plastic Wave System in the Sandia Plate Experiments	103
6.6a	Stress-Time History at a Station at the Target Center	104
6.6b	Stress-Time History at a Station One Quarter of the Target Thickness from the Interface	105
6.7	Qualitative Upper Fracture Threshold Time Dependence for Half-Hard E.T.P. Copper	106
6.8	Edge Effect With Groove	107
7.1	Characteristic Mesh for Plate Impact with Air Present	108
7.2	Nondimensionalized Characteristic Mesh	108
7.3	Comparison of Perfect Gas and Real Gas Analyses of the Air Effect	109
7.4	Surface Trajectories in the Presence of Air	110
7.5	Interface Pressure Profiles in the Presence of Air	111
7.6	Effect of Air Between Impacting Plates	112
7.7a	Wave Profiles in the Target	113
7.7b	Wave Profiles in the Target	114
7.7c	Wave Profiles in the Target	115

LIST OF ILLUSTRATIONS Continued

<u>Figure</u>	<u>Page</u>
7.8 Eulerian Characteristic Mesh for Impact with Air Between Driver and Target	116
7.9 Wave Profile at Interface Relative to No-Air Impact Time	117
7.10 Wave Profiles at Fixed Time After No-Air Impact	118
7.11 Pressure Rise at the Interface for Thick and Thin Driver Plates	119
7.12 Approximate Regions of Effects of Air in Plate Impact	120

LIST OF TABLES

<u>Table</u>		
I	Equation of State Data for Copper	121
II	Equation of State Data for Aluminum	122
III	Summary of Data for the Second Order, U_s, U_p Relation for Aluminum	123
IV	High Pressure Equation of State of Copper	123
V	Principal Components of Stress Increment and Strain Increment in Uniaxial Strain	124
VI	Multiple Shock Reflection Parameters	125

LIST OF SYMBOLS

a, b, d	Equation of state coefficients
c	Sound speed
s, h	Equation of state coefficients
k	Boltzmann constant
r	Lagrangian coordinate
t	Time
v	Volumetric strain
E	Young's modulus
F	Uniaxial strain modulus
G	Shear modulus
K	Bulk modulus
L	Riemann variable
P	Pressure
Q	Artificial viscosity
R	Eulerian coordinate
S	Entropy
T	Absolute temperature
U	Velocity
V	Specific volume
W	Work
Y	Yield stress
α	Symmetry exponent
β	Volume ratio

γ	Gruneisen ratio, ratio of specific heats
ϵ	Strain
ζ, η	Viscosity coefficients
λ, μ	Lame constants
ν	Poisson's ratio
ξ	Murnaghan exponent
ρ	Density
σ	Stress
τ, α	Nondimensionalized coordinates
ω	Lattice vibration frequency
ε	Internal energy

SECTION I

INTRODUCTION

The prediction of the response of shell-like structures to intense distributed impulsive loads involves several distinct problems. In the initial phase, stress waves are propagated through the thickness of the structure. Reflection of these stress waves at an inner free surface, and interaction of stress waves, may lead to transient tensile stresses of sufficient magnitude to induce fracture and lead to spallation. In the case of multilayer structures, transient tensile stresses may lead to unbonding and separation of layers.

The subsequent response of the structure may include elastic vibration, or, in more severe cases, large permanent plastic deformation, possibly accompanied by failure of supporting substructure and/or tearing of the skin.

In predicting the total response of the structure, it is first necessary to carry out an analysis of stress wave propagation in order to determine if spall occurs, and to determine the kinetic energy distribution among the spall and remaining separated material layers. This information can then be utilized in an analysis of the subsequent deformation and rupture of the structure.

The present report is concerned only with the stress wave propagation and spallation problem. The deformation problem is considered in another report generated under the same contract.^{1*}

* Superscripts refer to references listed at the end of the report.

The impulsive loads considered in this study are, in general, distributed over the surface of the structure in such a way that the variation in intensity over an area of the surface with dimensions corresponding to several times the thickness of the structure is negligible. Thus the problem may be treated as locally one-dimensional, with slab symmetry if the structure is locally nearly flat, or with cylindrical or spherical symmetry if the structure is locally curved. The solution is then built up of a number of locally one-dimensional calculations. Methods of solution, in cases where local one-dimensional symmetry cannot be assumed, generally become so unwieldy that the above method leads to great simplification when it can be used.

Loads to be considered induce very intense stresses of very short duration. The "equation of state" of the structural materials in this range is strongly nonlinear, necessitating numerical methods of solution. On the other hand, stresses are found to attenuate rapidly to levels where elastic effects become appreciable, and elastic-plastic transitions must be considered.

The wave propagation problem has been handled by two methods, each of which has special merits making it useful in specific instances. The two methods are; a straight numerical solution of the nonlinear differential equations of motion in finite difference form, and a characteristics method. While both methods are well known, a section is devoted to each in the following, outlining details which are peculiar to the methods used here.

The equation of state of structural materials is discussed in some detail, particularly in regard to extension to elastic-plastic behavior. Copper and aluminum are considered as quantitative examples. Consequences of the

equations of state, and of the use of the two methods of solution are investigated.

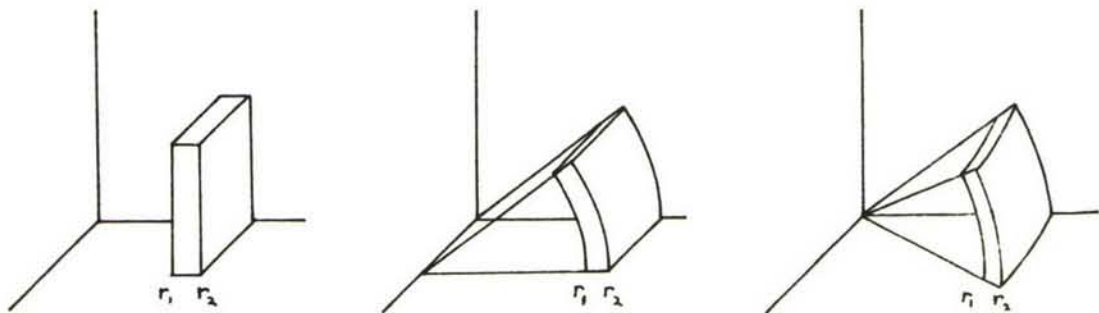
Using the above analytical methods, spall fracture criteria are examined, with a quantitative example for copper based on data of Lundergan,²² and the effect of air between impacting flat plates is analyzed.

SECTION II

FINITE DIFFERENCE METHOD

It is convenient to write the equations expressing conservation of mass, momentum, and energy in a one-dimensional medium in Lagrangian form. The coordinate system is thereby fixed in the medium and distorts with it. Problems associated with the transport of mass relative to the coordinate system are thereby eliminated. Consequently, the (Eulerian) position R of a particle is taken to be a function of time and Lagrangian coordinate r , here taken to be the initial position of the particle at time zero. It is generally not convenient to eliminate R altogether in a finite difference scheme and find the solution solely in terms of r and t . Consequently, the Eulerian coordinate $R(r, t)$ will be retained throughout the formulation.

The differential equations of motion are well known. They are derived by considering an element of the medium, and applying conservation principles. Generalizing to slab, cylindrical and spherical symmetry, the element becomes a flat slice, taken to be of lateral area π , a cylindrical shell of unit lateral width, with surface area $2\pi R$, or a spherical shell of surface area $4\pi R^2$, respectively.



The surface area of the element at position R thus becomes $\pi(2R)^{\alpha-1}$ where $\alpha = 1$ for slab, 2 for cylindrical and 3 for spherical symmetry.

Conservation of mass is expressed by the statement that the time rate of change of mass in a Lagrangian element is zero, i.e.,

$$\frac{\partial}{\partial t} \int_{r_1}^{r_2} \frac{1}{V} \pi(2R)^{\alpha-1} \frac{\partial R}{\partial r} dr = 0 \quad (2.1a)$$

where specific volume is denoted by V .

Conservation of momentum is expressed by the statement that the time rate of change of (radial) momentum of the element equals the net force on the element, i.e.,

$$\frac{\partial}{\partial t} \int_{r_1}^{r_2} \frac{1}{V} U \pi(2R)^{\alpha-1} \frac{\partial R}{\partial r} dr = (P_1 + Q_1) \pi(2R_1)^{\alpha-1} - (P_2 + Q_2) \pi(2R_2)^{\alpha-1} \quad (2.1b)$$

where U denotes velocity, P denotes pressure, and Q is an additional term denoting viscous forces.

Conservation of energy is expressed in the statement that the time rate of change of kinetic and internal energy of the segment must equal the net power flowing into the segment, i.e.,

$$\begin{aligned} & \frac{\partial}{\partial t} \int_{r_1}^{r_2} \frac{1}{V} \left(\frac{1}{2} U^2 + \mathcal{E} - W \right) \pi(2R)^{\alpha-1} \frac{\partial R}{\partial r} dr \\ &= (P_1 + Q_1) U_1 \pi(2R_1)^{\alpha-1} - (P_2 + Q_2) U_2 \pi(2R_2)^{\alpha-1} \end{aligned} \quad (2.1c)$$

where ϵ denotes internal energy and W here denotes energy per unit mass added to the medium from external sources.

If all quantities are continuous, the limiting process $r_1 \rightarrow r_2$ may be carried out in the usual way to produce the differential equations²

$$\frac{\partial}{\partial t} \left[\frac{1}{V} \pi(2R)^{\alpha-1} \frac{\partial R}{\partial r} \right] = 0 \quad (2.2a)$$

$$\frac{\partial}{\partial t} \left[\frac{1}{V} U \pi(2R)^{\alpha-1} \left(\frac{\partial R}{\partial r} \right) \right] = - \frac{\partial}{\partial r} [P + Q] \cdot \pi(2R)^{\alpha-1} \quad (2.2b)$$

$$\begin{aligned} \frac{\partial}{\partial t} \left[\frac{1}{V} \left(\frac{1}{2} U^2 + \epsilon - W \right) \pi(2R)^{\alpha-1} \frac{\partial R}{\partial r} \right] &= - \frac{\partial}{\partial r} [(P + Q) U] \\ &\times \pi(2R)^{\alpha-1} \end{aligned} \quad (2.2c)$$

This set of equations may be simplified by noting that the mass equation, Eq. 2.2a, may be immediately integrated to give

$$\frac{1}{V} \pi(2R)^{\alpha-1} \frac{\partial R}{\partial r} = k$$

where k is an integration constant. At $t = 0$, $R = r_0$, $V = V_0$ so that

$$k = (2r_0)^{\alpha-1} \pi/V_0$$

and

$$\frac{1}{V} R^{\alpha-1} \frac{\partial R}{\partial r} = \frac{1}{V_0} r^{\alpha-1} \quad (2.3a)$$

Substitution in Eqs. 2.2b and 2.2c then yields

$$\frac{\partial U}{\partial t} = - V_0 \frac{\partial}{\partial r} (P + Q) \cdot \left(\frac{R}{r} \right)^{\alpha-1} \quad (2.3b)$$

and

$$\frac{\partial}{\partial t} \left(\frac{1}{2} U^2 + \varepsilon \right) = - V_0 \frac{\partial}{\partial r} [(P + Q) U] \left(\frac{R}{r} \right)^{\alpha-1} + \frac{\partial W}{\partial t} \quad (2.3c)$$

Further manipulation then yields the familiar equations of motion

$$V = V_0 \frac{\partial R}{\partial r} \left(\frac{R}{r} \right)^{\alpha-1} \quad (2.4a)$$

$$\frac{\partial U}{\partial t} = - V \frac{\partial}{\partial R} (P + Q) \quad (2.4b)$$

$$\frac{\partial \varepsilon}{\partial t} = - (P + Q) \frac{\partial V}{\partial t} + \frac{\partial W}{\partial t} \quad (2.4c)$$

Together with the definition

$$\frac{\partial R}{\partial t} = U \quad (2.4d)$$

an equation of state describing material behavior

$$P = f(V, \varepsilon) \quad (2.4e)$$

and an equation defining the dissipative term Q in terms of the other variables, these are then sufficient to define a solution subject to given initial and boundary conditions.

The differential equations, Eq.2.4, may be differenced in a variety of ways. It is of course desirable that the difference equations correspond to the differential equations, Eq.2.4, to second order, i.e., a Taylor series expansion of the difference expression about a point should correspond to the differential expression in terms of first order. However, it is also considered desirable that the

difference equations should provide second order analogs of Eqs. 2.2 and 2.3, i.e., explicitly conserve mass, momentum, and energy, also to second order. This restricts the choice of difference equations somewhat.

The continuum is divided into finite segments Δr in (Lagrangian) space, and Δt in time. The usual notation

$$x_m^n = X(m\Delta r, n\Delta t)$$

is used. Providing all quantities are smooth and continuous, and vary sufficiently slowly over the finite-difference mesh (i.e., the mesh is chosen small enough), quantities may be averaged over each mesh.

Considering the segment $m\Delta r$ to $(m + 1)\Delta r$, Eq. 2.1a thus becomes

$$\frac{\partial}{\partial t} \left[\frac{\pi^2}{\alpha V} \frac{\alpha-1}{m+1/2} \left\{ (R_{m+1})^\alpha - (R_m)^\alpha \right\} \right] = 0$$

or using central time differencing

$$\frac{\frac{\pi^2}{\alpha V} \frac{\alpha-1}{m+1} \left[(R_{m+1}^{n+1})^\alpha - (R_m^{n+1})^\alpha \right] - \frac{\pi^2}{\alpha V} \frac{\alpha-1}{m+1/2} \left[(R_{m+1}^n)^\alpha - (R_m^n)^\alpha \right]}{\Delta t} = 0$$

which is a second order analog of Eq. 2.2a.

Neglecting second order terms, this may also be written

$$\frac{1}{V_{m+1/2}^{n+1}} (R_{m+1}^{n+1})^{\alpha-1} (R_{m+1}^{n+1} - R_m^{n+1}) = \frac{1}{V_{m+1/2}^n} (r_{m+1/2}^n)^{\alpha-1} (r_{m+1} - r_m) \quad (2.5a)$$

This is a second order analog of Eq. 2.3a. Equation 2.5a

could have been written down directly, since mass is conserved by definition of the Lagrangian mesh. However, proceeding in the same way, equations which are second order analogs of Eqs. 2.1b and 2.1c, 2.2b and 2.2c; and 2.3b and 2.3c may be derived. The analogs to Eq. 2.3b and 2.3c are

$$\frac{U_{m+1/2}^{n+1} - U_{m+1/2}^n}{\Delta t^{n+1/2}} = - \frac{V_{m+1/2}^0}{(r_{m+1} - r_m)} \left[\left(P_{m+1}^{n+1/2} + Q_{m+1}^{n+1/2} \right) \left(\frac{R_{m+1}^{n+1/2}}{r_{m+1/2}} \right)^{\alpha-1} - \left(P_m^{n+1/2} + Q_m^{n+1/2} \right) \left(\frac{R_m^{n+1/2}}{r_{m+1/2}} \right)^{\alpha-1} \right] \quad (2.5b)$$

$$\frac{\frac{1}{2} \left(U_{m+1/2}^{n+1} \right)^2 - \frac{1}{2} \left(U_{m+1/2}^n \right)^2 + \epsilon_{m+1/2}^{n+1} - \epsilon_{m+1/2}^n - \Delta W_{m+1/2}^{n+1/2}}{\Delta t^{n+1/2}} = - \frac{V_{m+1/2}^0}{(r_{m+1} - r_m)} \left[\left(P_{m+1}^{n+1/2} + Q_{m+1}^{n+1/2} \right) U_{m+1}^{n+1/2} \left(\frac{R_{m+1}^{n+1/2}}{r_{m+1/2}} \right)^{\alpha-1} - \left(P_m^{n+1/2} + Q_m^{n+1/2} \right) U_m^{n+1/2} \left(\frac{R_m^{n+1/2}}{r_{m+1/2}} \right)^{\alpha-1} \right] \quad (2.5c)$$

Neglecting only second order quantities, manipulation of these equations yields

$$V_{m+1/2}^{n+1} = V_{m+1/2}^0 \left(\frac{R_{m+1}^{n+1} - R_m^{n+1}}{r_{m+1} - r_m} \right) \left(\frac{R_{m+1/2}^{n+1}}{r_{m+1/2}} \right)^{\alpha-1} \quad (2.6a)$$

$$\frac{U_{m+1/2}^{n+1} - U_{m+1/2}^n}{\Delta t^{n+1/2}} = - V_{m+1/2}^{n+1/2} \left(\frac{P_{m+1}^{n+1/2} - P_m^{n+1/2} + Q_{m+1}^{n+1/2} - Q_m^{n+1/2}}{R_{m+1}^{n+1/2} - R_m^{n+1/2}} \right) \quad (2.6b)$$

$$\begin{aligned} \epsilon_{m+1/2}^{n+1} - \epsilon_{m+1/2}^n &= - \left(P_{m+1/2}^{n+1/2} + Q_{m+1/2}^{n+1/2} \right) \left(V_{m+1/2}^{n+1} - V_{m+1/2}^n \right) \\ &+ \Delta W_{m+1/2}^{n+1/2} \end{aligned} \quad (2.6c)$$

It may be easily verified that these correspond to Eqs. 2.4 to second order.

If quantities vary sufficiently slowly over the mesh, then, to second order

$$X_{m+1/2} = \frac{1}{2}(X_{m+1} + X_m)$$

The equations may be rendered explicit by moving Eq. 2.6b back half a mesh in space and time, and expressing Eq. 2.6a in its equivalent form

$$V_{m+1/2}^{n+1} = V_{m+1/2}^0 \frac{\left(\frac{R_{m+1}}{R_m} \right)^\alpha - \left(\frac{R_m}{R_{m+1}} \right)^\alpha}{\left(\frac{r_{m+1}}{r_m} \right)^\alpha - \left(\frac{r_m}{r_{m+1}} \right)^\alpha} \quad (2.7a)$$

$$\frac{U_m^{n+1/2} - U_m^{n-1/2}}{\Delta t^{n+1/2} + \Delta t^{n-1/2}} = \frac{P_{m-1/2}^n - P_{m+1/2}^n + Q_{m-1/2}^n - Q_{m+1/2}^n}{\frac{1}{V_{m+1/2}^n} \left(R_{m+1}^n - R_m^n \right) + \frac{1}{V_{m-1/2}^n} \left(R_m^n - R_{m-1}^n \right)} \quad (2.7b)$$

$$\begin{aligned} \varepsilon_{m+1/2}^{n+1} - \varepsilon_{m+1/2}^n &= \frac{1}{2} \left(P_{m+1/2}^{n+1} + P_{m+1/2}^n + Q_{m+1/2}^{n+1} + Q_{m+1/2}^n \right) \\ &\times \left(V_{m+1/2}^n - V_{m+1/2}^{n+1} \right) + \Delta W_{m+1/2}^{n+1/2} \end{aligned} \quad (2.7c)$$

These equations are then taken together with the difference forms of Eqs. 2.4d and 2.4e

$$\frac{R_m^{n+1} - R_m^n}{\Delta t^{n+1/2}} = U_m^{n+1/2} \quad (2.7d)$$

$$P_{m+1/2}^{n+1} = f(V_{m+1/2}^{n+1}, \varepsilon_{m+1/2}^{n+1}) \quad (2.7e)$$

Following von Neumann and Richtmyer,³ a smooth solution is ensured by a quadratic artificial viscosity term. Provision is also made for a linear artificial viscosity term.

$$Q_{m+1/2}^n = -\frac{1}{V_{m+1/2}^n} \left(\eta^2 |\Delta U| + \zeta c_{m+1/2}^{n-1} \right) \Delta U \quad (2.7f)$$

where

$$\Delta U = U_{m+1}^{n-1/2} - U_m^{n-1/2}$$

and

$$c^2 = dP/d\rho$$

represents sonic velocity. Constants η and ζ are normally set to zero when $\Delta U < 0$.

The conditional stability of the explicit equations is well known. An approximate stability criterion,

for nearly isentropic processes, derived in a manner analogous to that of von Neumann and Richtmyer³ has proved useful in many cases.

$$\Delta t^{n+1/2} = \frac{R_{m+1}^n - R_m^n}{c_{m+1/2}^n (1 + 2\zeta) + 4\eta^2 |\Delta U|} \quad (2.7g)$$

the minimum over all m being used to advance the calculation.

Equations 2.7f and 2.7g are not correctly centered, but this should not entail serious consequences since all quantities are necessarily varying slowly. (In the derivation of Eq.2.7g, quantities are taken as locally constant.) Correct centering of these quantities in Eqs.2.7b and 2.7c is much more important.

Equations 2.7 are similar to those used by Grandey,⁴ except for the centering of Q . It may also be noted that the equations reduce identically to those of Richtmyer⁵ with correct Q centering, when equal space and time increments and uniform initial specific volume are used.

If all quantities are known at time n (or initially at time zero, corresponding to initial conditions) Eq.2.7g is first used to determine the maximum allowable time interval to advance the calculation, followed in turn by Eqs.2.7b, 2.7d, 2.7a, and 2.7f to obtain $U^{n+1/2}$, R^{n+1} , V^{n+1} and Q^{n+1} , respectively over all m . Equations 2.7c and 2.7e are then solved as simultaneous equations for P^{n+1} for all m . This process is then repeated stepwise to produce the desired solution.

Boundary conditions are introduced through the initial conditions, e.g., layers of different materials are

introduced by specifying appropriate initial specific volumes, and providing for different equations of state in the appropriate meshes. Free surfaces may be introduced by setting the initial density and pressure to zero in the mesh adjacent to the surface. In practice it is somewhat more convenient to set the density and pressure in the mesh outside the boundary to zero at each time cycle by using (for a right-hand boundary)

$$\frac{U_M^{n+1/2} - U_M^{n-1/2}}{\Delta t^{n+1/2} + \Delta t^{n-1/2}} = V_{M-1/2}^n \frac{P_{M-1/2}^n + Q_{M-1/2}^n}{R_M^n - R_{M-1}^n} \quad (2.8)$$

in place of Eq.2.7b. This saves carrying an extra mesh outside each free boundary.

In addition, a "spall and join" routine is provided, which operates as follows. When the stress reaches some predetermined critical negative (tensile) value, the material is allowed to part and form two new free surfaces. If at some later time these free surfaces attempt to cross, then the correct interface condition is again used. At an unbonded interface, of course, the critical stress is zero, while in the interior of a material, the critical stress is the fracture stress.

SECTION III
CHARACTERISTICS METHOD

The method of characteristics is well known.² Restricting the discussion to one-dimensional slab symmetry and isentropic processes ($Q = 0$), the Lagrangian mass and momentum conservation equations, Eqs. 2.4a and 2.4b reduce simply to

$$\frac{\partial V}{\partial t} = V_0 \frac{\partial U}{\partial r} \quad (3.1a)$$

$$\frac{\partial U}{\partial t} = - V_0 \frac{\partial P}{\partial r} \quad (3.1b)$$

while the energy equation, Eq. 2.4c, becomes simply

$$\frac{\partial S}{\partial t} = 0 \quad (3.1c)$$

where S is the specific entropy. Using Eq. 3.1c, the equation of state, Eq. 2.4e reduces simply to

$$P = f(V) \quad (3.1d)$$

Providing that the Jacobian

$$\frac{\partial(U, V)}{\partial(r, t)} \neq 0 \quad ,$$

we can interchange dependent and independent variables in Eqs. 3.1a and 3.1b:

$$\frac{\partial r}{\partial U} = V_0 \frac{\partial t}{\partial V} \quad (3.2a)$$

$$\frac{\partial r}{\partial P} = - V_0 \frac{\partial t}{\partial U} \quad (3.2b)$$

Introducing new functions

$$c^2 = - V_0^2 \frac{\partial P}{\partial V} \quad (3.3a)$$

$$L = \int \frac{c \partial V}{V_0} = - \int \frac{V_0 \partial P}{c} \quad (3.3b)$$

Eqs. 3.2 transform to

$$\frac{\partial r}{\partial U} = c \frac{\partial t}{\partial L} \quad (3.4a)$$

$$\frac{\partial r}{\partial L} = c \frac{\partial t}{\partial U} \quad (3.4b)$$

The system, Eqs. 3.4, has fixed characteristics in the U, L plane given by the family of curves

$$U \pm L = \text{Constant} \quad (3.5)$$

Writing

$$U - L = \alpha$$

$$U + L = \beta$$

Eqs. 3.4 become

$$\frac{\partial r}{\partial \alpha} + c \frac{\partial t}{\partial \alpha} = 0 \quad (3.6a)$$

$$\frac{\partial r}{\partial \beta} - c \frac{\partial t}{\partial \beta} = 0 \quad (3.6b)$$

and the characteristic directions in the r, t plane are given by

$$\frac{\partial r}{\partial t} = \pm c \quad (3.7)$$

Here c may be identified as the Lagrangian sound speed.

While analytical solutions can be easily obtained for simple wave systems (e.g., Ref. 21), it is more convenient to use a simple numerical scheme for problems

involving more complex wave interactions and reflections.

The solution is represented by a finite number of characteristic lines defined by Eqs.3.5 and 3.7. Examples are shown in Figs.3.1 and 3.2 in which the numbering convention which has been used is illustrated.

Positive characteristics I^+ and negative characteristics I^- are numbered consecutively. Intersection points of characteristics I_m^+ and I_n^- in the r, t plane are denoted $S_{m,n}$, and quantities at each point $S_{m,n}$ are similarly subscripted $()_{m,n}$.

If quantities are known at a previous point $S_{m-1,n}$, $S_{m,n-1}$, Eqs.3.5 and 3.7 allow quantities at $S_{m,n}$ to be evaluated, i.e.,

$$(U + L)_{m,n-1} = (U + L)_{m,n} \quad (3.8a)$$

$$(U - L)_{m-1,n} = (U - L)_{m,n} \quad (3.8b)$$

P, V and c at $S_{m,n}$ may then be found from $L_{m,n}$ by Eq.3.3 once a suitable equation of state, Eq.3.1d, has been inserted.

Then

$$\frac{r_{m,n} - r_{m,n-1}}{t_{m,n} - t_{m,n-1}} = \frac{1}{2} (c_{m,n} + c_{m,n-1}) \quad (3.9a)$$

$$\frac{r_{m,n} - r_{m-1,n}}{t_{m,n} - t_{m-1,n}} = \frac{1}{2} (c_{m,n} + c_{m-1,n}) \quad (3.9b)$$

In this way a complete solution $U(r,t)$, $P(r,t)$ and $V(r,t)$ may be constructed from the initial conditions defining these quantities at $t = 0$.

Boundaries require special treatment. At a free surface, $P = 0$ and thus $c = c_0$, $L = L_0$ and $V = V_0$ where $()_0$

refers to conditions at $t = 0$ at the boundary. Thus U_{mm} may be found from Eqs.3.8a or 3.8b directly for a right-hand or left-hand boundary, respectively. In Lagrangian coordinates, the position of the boundary is fixed and $r_{mm} = r_{0,0}$. Thus, $t_{m,m}$ may be found from Eqs.3.9a or 3.9b for a right-hand or left-hand boundary, respectively.

At an interface between different materials, the conditions are more complex. Denoting quantities in the second material (considered to lie to the right as in Fig.3.1) by $(\cdot)'$, we have the condition that

$$P_{m,m} = P'_{m,m} \quad (3.10)$$

By virtue of Eqs.3.1d and 3.3 we may write

$$P = g(L) \quad (3.11)$$

so that the condition becomes

$$g(L)_{m,m} = g'(L')_{m,m} \quad (3.12a)$$

Furthermore one has the condition

$$U_{m,m} = U'_{m,m} \quad (3.12b)$$

In the left-hand material, Eq.3.8a applies, i.e.,

$$(U + L)_{m,m} = (U + L)_{m-1,m} \quad (3.12c)$$

In the present example, a simple wave is propagating to the right into the second material (Fig.3.1). Thus, $(U - L)$ is constant everywhere, and

$$(U' - L')_{m,m} = (U' - L')_{0,0} \quad (3.12d)$$

Equations 3.12 are four simultaneous equations for

the four unknowns $L_{m,m}$, $L'_{m,m}$, $U_{m,m}$, and $U'_{m,m}$. Similar equations may be easily written for the case of a wave moving to the left being refracted at an interface.

If surface positions are desired, the simplest scheme is to accumulate displacements at each mesh point, i.e.

$$R_{mm} = r_{mm} + \sum_{k=1}^m \frac{1}{2} (U_{kk} + U_{k-1,k-1}) (t_{kk} - t_{k-1,k-1}) \quad (3.13)$$

The calculation procedure can be mechanized to allow use of a digital computer. The most difficult task is to write the logic necessary to determine the configuration of the characteristic mesh in the r,t plane. Providing that the form of the characteristic mesh is known beforehand, this can be easily done. Two approaches have therefore been used. Programs have been written (for the Royal McBee LGP 30 computer), covering simple interactions as, for example, reflection of a wave fan at a free surface, or crossing of two wave fans. Also, Eqs. 3.8 through 3.12 have been programmed so that the computer may be operated in a semi-manual manner, i.e., quantities at points $S_{m,n-1}$ and $S_{m-1,n}$ are entered manually at the keyboard of the machine, and quantities at $S_{m,n}$ are then computed automatically upon selection of the correct equations, e.g., interior point, free surface, etc. In this way solutions may be built up quite rapidly with a minimum of complex computer logic.

The foregoing has been restricted to isentropic processes, and thus strong shocks cannot be handled by this analysis. It is possible to extend the method to include entropy variations,² in which case a third characteristic direction is found, representing particle paths, along which the entropy is constant. Strong shocks are then treated as

internal floating boundaries across which the Rankine-Hugoniot relations are used.

However, for weak shocks across which the entropy change is negligible, it is possible to use the weak shock approximation of Courant and Friedrichs,² within the framework of the foregoing isentropic theory.

Thus, when two positive characteristics meet (as in Fig.3.2), say I_k^+ , I_m^+ , a shock wave forms representing a jump in variables from $()_{k,n}$ to $()_{m,n}$. The velocity of the shock and hence its slope in the r,t plane is approximated by

$$\frac{\partial r}{\partial t} = \frac{1}{2}(c_{k,n} + c_{m,n}) \quad (3.14)$$

When several positive characteristics combine, the subscripts k,m refer to conditions on the I^+ characteristics of lowest and highest number respectively, involved in the shock formation. Points on the characteristic mesh involving a shock are labeled with three subscripts, k , m , and n , as shown in Fig.3.2 for a right going shock.

The weak shock may be regarded as a group of coincident characteristics, and a point $S_{\overline{k,m},n}$ may therefore be thought of as representing $(m-k)$ coincident points $S_{k,n}$, $S_{k+1,n} \dots S_{m,n}$. Thus, interaction of a right-going shock with a negative characteristic or a surface may be handled (in the computer) as a series of $(m-k)$ characteristic interactions, using Eqs.3.8. However, Eq.3.14 is substituted for Eq.3.9a, to obtain r and t .

A left-going shock may be treated in the same way; in this case the last two subscripts refer to the first and last I^- characteristics involved in the shock formation. The system requires use of four index registers in the computer,

a nonzero value in the first register signalling the existence of a right-going shock, and a nonzero number in the last register signalling the existence of a left-going shock.

SECTION IV

EQUATION OF STATE

4.1 Introduction

Strictly speaking, a real solid does not in general possess a simple equation of state in the sense that there exists a unique single-valued function relating the variables characterizing the state of the material. Due to effects such as strain hardening, phase changes and the possibility of nonequilibrium states, the relation among state variables is dependent on the entire history of the material up to the time under consideration. However, with certain necessarily gross assumptions regarding the initial state of the material before commencement of the process under analysis, and the allowable changes in the material during the process, it is possible to construct a relation among state variables at a particular time, which is a function of the detailed path of the process up to that time. The term constitutive equation may be applied to cover such relationships. Once such an equation has been constructed, it is quite possible to use it in a numerical solution of an initial value problem, particularly in a Lagrangian finite-difference scheme, since it is possible for the computer to keep track of the detailed history of each mass point.

At very high pressures, it is usually assumed that the deviatoric stress component, which the material may support, is negligible in comparison with the dilatational stress. If equilibrium is attained very rapidly (about 10^{-7} seconds) and if wave profiles are steady in time, then a simple single-valued entropic equation of state may be found from measurements on strong shock waves.⁷⁻⁹

It is here assumed that an extrapolation of this equation to low stresses is still valid for the dilatational component. This assumption is investigated later in this report by comparison with static compressibility and thermodynamic data at zero pressure.

If, further it is assumed that the deviatoric component of stress is limited by a yield condition and that the dilatational component of plastic strain is zero,¹⁶ it is then possible to deduce a relation between the longitudinal components of stress and strain from weak shock wave measurements. For a few aluminum alloys Fowles¹⁷ and Lundergan¹⁸ have shown that the resulting relation is comparable with static stress-strain relations obtained under conditions of uniaxial stress (engineering tensile test), indicating that equilibrium is also reached very rapidly in these materials.

4.2 High Pressure Region

The high pressure equation of state has been under investigation for some time.^{7,8,9} The experimental method involves inducing a plane shock wave propagating into un-stressed material under investigation by explosive or other means, and determining the shock velocity and material velocity behind the shock. If the shock wave profile remains constant in time, and equilibrium is achieved very rapidly behind the shock, the Rankine-Hugoniot relations then allow the compression, stress, and energy change across the shock to be related to the shock velocity U_s and the material velocity U_p behind the shock relative to the material ahead of the shock.

$$\frac{V_o - V}{V_o} = \frac{U_p}{U_s} \quad \begin{matrix} \text{Shock Vel.} \\ \text{Material Vel.} \end{matrix} \quad (4.1a)$$

PRESSURE

$$P_H = \frac{U_s U_p}{V_o} = U_s V_p \rho \quad (4.1b)$$

INTERNAL ENERGY

$$\varepsilon_H - \varepsilon_o = \frac{1}{2} P_H (V_o - V) \quad (4.1c)$$

Here $()_H$ refers to conditions behind the shock, and $()_o$ refers to ambient conditions in the unstressed material ahead of the shock.

The locus of $P_H(V)$ points determined from many such experiments with different shock strengths is termed the shock Hugoniot.

For many materials it is found experimentally that U_s is a linear function of U_p over a wide range, expressible by the relation

$$U_s = c + s U_p \quad (4.2)$$

Using Eqs. 4.1 and 4.2, $P_H(V)$ becomes

SONIC SPEED

$$P_H = \frac{c^2 (V_o - V)}{\{V_o - s(V_o - V)\}^2} \quad (4.3)$$

$s_{COPPER} = 1.497$

The shock Hugoniot determined in this way represents states which may be reached by a shock process from the unstressed state at ambient conditions. It is desirable to find a relationship between P , V , and ε for states neighboring the shock Hugoniot, which may be reached by neighboring adiabats or isotherms. Additional information is required. The usual procedure is to assume a functional form for the equation of state based on solid state theory. This has been done by Walsh et al.⁷ The theory will be briefly reproduced to facilitate later discussion.

The equation of state is assumed to take the form of the Mie-Gruneisen equation¹²

$$(P - P_K) = \gamma \left(\frac{\varepsilon - \varepsilon_K}{V} \right) \quad (4.4)$$

Here $(\)_K$ refers to the 0°K isotherm, and γ , the Gruneisen ratio, is the ratio of the thermal component of pressure to the lattice vibrational energy density.

The assumption is now made that at very high pressures the deviatoric stress which the material may support is negligible in comparison with the dilatational stress, and the state of stress may be simply characterized by a pressure. Under this assumption, Eq.4.4 may be written

$$(P_H - P_K) = \gamma \left(\frac{\varepsilon_H - \varepsilon_K}{V} \right) \quad (4.5)$$

While attempts have been made to estimate γ at very large compressions from experimental data,^{9,10} Walsh et al. use a relation between γ and P_K derived from solid state theory. Slater¹² has given

$$\gamma = - \frac{V}{2} \frac{\frac{\partial^2}{\partial V^2} (P_K)}{\frac{\partial}{\partial V} (P_K)} - \frac{2}{3} \quad (4.6a)$$

while Dugdale and MacDonald¹³ have given

$$\gamma = - \frac{V}{2} \frac{\frac{\partial^2}{\partial V^2} (P_K V^{2/3})}{\frac{\partial}{\partial V} (P_K V^{2/3})} - \frac{1}{3} \quad (4.6b)$$

Inserting Eq.4.6a or Eq.4.6b together with Eq.4.1

into Eq.4.5, and noting that

$$\epsilon_K = \int_V^{V_0} P_K(v) dv$$

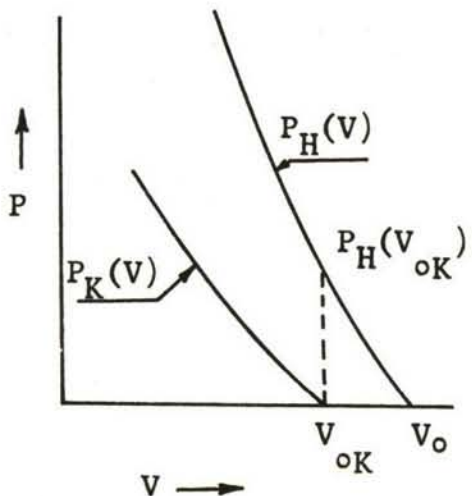
results in a differential equation for P_K , which may be solved (in this case numerically) with suitable initial values $P'_K, (\partial P / \partial V)'_K$, V' and ϵ' at some known point on the 0°K isotherm. The quantity $\gamma(V)$ may then be determined from Eq.4.6a or Eq.4.6b.

In order to obtain suitable initial conditions, it is necessary to introduce additional assumptions. At low pressures the deviatoric stress which the material may support is not negligible. Since Eq.4.4 applies only to pure dilatation, shock Hugoniot data obtained at low pressure cannot be used to proceed from known initial conditions at zero pressure. One might make some gross assumptions in order to arrive at suitable initial conditions at sufficiently high pressure,⁹ or it is necessary to make some assumptions regarding extrapolation of the shock Hugoniot data to zero pressure. The latter course has been used by Walsh et al.⁷ It is assumed that the U_s versus U_p curve may be linearly extrapolated to $U_p = 0$. For many materials, the intercept c corresponds quite closely to the adiabatic bulk sound speed deduced from static compressibility measurements.

Initial conditions then become $P'_K = 0, (\partial P / \partial V)'_{0\text{K}}$, $V_{0\text{K}}$, and $\epsilon_{0\text{K}}$, where $(\)_{0\text{K}}$ refers to conditions at the foot ($P = 0$) of the 0°K isotherm. It is possible to obtain $(\epsilon_0 - \epsilon_{0\text{K}})$ by integrating the Debye specific heat curve. The quantities $V_{0\text{K}}$ and $(\partial P / \partial V)'_{0\text{K}}$ may be estimated from Eq. 4.4, i.e. at $P = 0$, $V = V_{0\text{K}}$;

$$v_{oK} = \gamma_{oK} \frac{\varepsilon_H(v_{oK}) - \varepsilon_{oK}}{P_H(v_{oK})} \quad (4.7a)$$

$$\left(\frac{\partial P}{\partial V} \right)_{oK} = \frac{1}{v_{oK}} \left\{ v_{oK} \left(\frac{\partial P_H}{\partial V} \right)_{oK} + P_H(v_{oK}) \right. \\ \left. - [\varepsilon_H(v_{oK}) - \varepsilon_{oK}] \left(\frac{\partial \gamma}{\partial V} \right)_{oK} - \gamma_{oK} \left(\frac{\partial \varepsilon_H}{\partial V} \right)_{oK} \right\} \quad (4.7b)$$



These may be evaluated if suitable values of γ_{oK} and $(\partial \gamma / \partial V)_{oK}$ can be found. Assuming $(\partial \gamma / \partial V)$ constant in the small interval v_{oK} to v_o we have

$$\left(\frac{\partial \gamma}{\partial V} \right)_{oK} = \left(\frac{\partial \gamma}{\partial V} \right)_o \quad (4.8a)$$

$$\gamma_{oK} = \gamma_o + \left(\frac{\partial \gamma}{\partial V} \right)_o (v_{oK} - v_o) \quad (4.8b)$$

Assuming the Slater relation, Eq.4.6a, or Dugdale-MacDonald relation, Eq.4.6b, to be valid along an adiabat though v_o allows γ_o and $(\partial \gamma / \partial V)_o$ to be determined. Using Eq.4.3 and Eq.4.6a

$$\gamma_o = 2s - \frac{2}{3} \quad (4.9a)$$

$$\left(\frac{\partial \gamma}{\partial V}\right)_0 = \frac{1}{V_0} (s^2 + \frac{4}{3} s) \quad (4.9b)$$

Alternatively, using Eq.4.3 and Eq.4.6b

$$\gamma_0 = 2s - 1 \quad (4.10a)$$

$$\left(\frac{\partial \gamma}{\partial V}\right)_0 = \frac{1}{V_0} (s^2 - \frac{1}{3}s + \frac{5}{9}) \quad (4.10b)$$

It may also be noted that differentiation of Eq.4.4 at constant volume yields

$$\gamma_0 = V \left(\frac{\partial P}{\partial \epsilon} \right)_V = - \frac{V_0}{C_p} \left(\frac{\partial P}{\partial V} \right)_s \left(\frac{\partial V}{\partial T} \right)_P$$

$$\gamma_0 = - \frac{V_0 \propto K}{C_p} \quad (4.11)$$

where C_p is the specific heat at constant pressure, K is the adiabatic bulk modulus and \propto is the volumetric thermal expansion coefficient, all at zero pressure.

Walsh et al.⁷, and McQueen and Marsh⁸ have given analytical fits to $P_H(V)$ and to $\gamma(V)$ computed using the Dugdale-MacDonald relation, Eq.4.6b, and the thermodynamic definition of γ_0 , Eq.4.11, for a large number of metals. Equation 4.4 may be written as

$$(P - P_H) = \gamma \left(\frac{\epsilon - \epsilon_H}{V} \right) \quad (4.12)$$

It is often more expedient for computational purposes to express Eq.4.12 in the form

$$P = M(V) + \varepsilon \cdot N(V)$$

(4.13)

where in this case

$$M(V) = P_H(V) \left[1 - \frac{\gamma}{2} \frac{V_0 - V}{V} \right]$$

$$N(V) = \frac{\gamma(V)}{V}$$

It is generally convenient to fit M and N with polynomials in (V_0/V) . Equation 4.13 may then be used directly as an equation of state at high pressures.

The accuracy of the pressure offset from the experimental shock Hugoniot $(P - P_H)$ is equal to the accuracy with which γ has been determined. This depends in turn on the validity of the linear extrapolation of the U_s versus U_p data to $U_p = 0$, and on the validity of the relation between γ and P_K .

In order to investigate the uncertainties, Eq. 4.5 was reintegrated using both the Slater and Dugdale-MacDonald relations for γ , with particular attention to the low pressure region. In addition, since γ was found to vary only slowly with V , an integration was performed with γ held constant at γ_0 defined by Eq. 4.11.

Numerical results for copper are shown in Table I for relatively low pressures. Also shown are the relevant initial conditions. U_s versus U_p data obtained by McQueen and Marsh⁸ and Altshuler⁹ were fitted by Eq. 4.2. For the case of copper, the resultant value of c is in excellent agreement with the adiabatic sound speed computed from Bridgman's static compressibility data. Hugoniot pressures P_H listed in the table are computed from the resultant relation, Eq. 4.2. Walsh et al.⁷ noted that γ_0 computed from

the Dugdale-MacDonald relation, Eq.4.10a, are generally in slightly better agreement with thermodynamic data, Eq.4.11, than when computed from the Slater relation, Eq.4.9a. This is true in the case of copper, the Dugdale-MacDonald γ_0 being in excellent agreement with the thermodynamic γ_0 . Initial conditions for all three integrations of Eq.4.5 were therefore computed using the thermodynamic γ_0 , and the value of $(\partial\gamma/\partial V)_0$ from Eq.4.10b.

The differences in γ , and hence in the pressure offset using the Dugdale-MacDonald relation and the Slater relation respectively, amount to about 8 per cent at 100 kb and increase to 18 per cent at 900 kb. However, since the thermal pressure ($P_H - P_K$) over the range reaches a maximum of about 9 per cent of P_H at 300 kb, the computed values of P_K agree within 2 per cent up to 300 kb. Since the Slater γ increases slightly while the Dugdale-MacDonald γ decreases over this range, the constant γ gives results intermediate between the two.

Isentropes P_A computed from Eq.4.12 by setting

$$\epsilon = \int_V^{V_0} P \, dv$$

are also listed. The offsets of the isentropes from the Hugoniot ($P_H - P_A$) reach a maximum of 2 per cent at 250 kb, and are therefore negligible, a result which may be surmised from the fact that the entropy change is of third order in the compression, and hence negligible in this range. To all intents and purposes, it is permissible to neglect entropy changes and use the Hugoniot as equation of state below about 0.25 megabars in copper, where only adiabatic* wave propagation is involved. For greater offsets,

* Adiabatic is here used in the strict sense that no heat is added or subtracted by external sources.

such as isentropes or isotherms through zero pressure states at significantly different temperatures, improvement in precision is possible by the use of Eq.4.12, with, however, a probable uncertainty in pressure offset from the experimental Hugoniot of up to 20 per cent. In the present instance, taking γ constant in this range leads to results as good as any, with significant simplification to the equation of state.

Two checks on the linear extrapolation of U_s versus U_p data are possible. One may obtain isotherms (P_T) through V_0 , (i.e., at 298 °K) which are directly comparable to Bridgman's static compressibility data. One may also evaluate the internal energy as a function of volume ($E_{P=0}$) at zero pressure, which is directly comparable to zero pressure specific heat and thermal expansion data. In the latter case, thermodynamic data at high temperatures corresponds to increased specific volume. This corresponds to extrapolation to negative U_p or tension states.

Table I shows that the offset ($P_H - P_T$) is less than 3 per cent at 30 kilobars, the highest pressure at which reliable static data is available, and the difference between isotherms calculated on the basis of the three methods is consequently negligible. Comparison with static data of Bridgman¹¹ shows agreement within the combined experimental error.

Comparing values of $E_{P=0}$ shows that best agreement with thermodynamic data is shown by the Dugdale-MacDonald γ , the agreement again being within experimental error. This has also been noted by McQueen and Marsh.⁸ This agreement is very encouraging, since the offset from the (extrapolated) Hugoniot in this case is large.

One might therefore have some confidence in the

linear extrapolation of the U_p versus U_s fit. The assumption will later be made that the extrapolated isentrope applies to the dilatational components of stress and strain at low compressive and tensile stresses, and the above comparisons lend considerable support to such an assumption.

Similar results for aluminum are shown in Table II. U_s versus U_p data obtained by Walsh et al.⁷ and Altshuler⁹ were again fitted with a linear expression, Eq.4.2. In this case, agreement of c with the adiabatic sound speed from static compressibility tests is not so good. Also, the Slater γ_0 from Eq.4.9a is in better agreement with the thermodynamic γ_0 , Eq.4.11, than the Dugdale-MacDonald, γ_0 , Eq.4.10a. Initial conditions were nevertheless computed from the thermodynamic γ_0 and $(\partial\gamma/\partial V)_0$ taken from the Dugdale-MacDonald relation, Eq.4.10b.

Differences in γ , and offsets of the various curves from the Hugoniot are of the same order as for copper, and the same remarks apply. However, comparison of the computed 298 °K isotherm P_T with Bridgman's data reveals differences which are significant, in line with the disagreement in c . Also significant is the disagreement in computed $\epsilon_{P=0}$ and thermodynamic data. Thus, for aluminum the linear extrapolation of the U_s versus U_p data to $U_{P=0}$ does not appear to be as satisfactory, and the description of the low pressure and tensile region may also be considered to be less satisfactory than in the case of copper.

An examination of the experimental data indicates that a quadratic U_s versus U_p fit, constrained to pass through the Bridgman sound speed at $U_p = 0$ may prove more suitable. By carrying out a least squares fit, it was found that the expression

$$U_s = c + s U_p + h U_p^2$$

fitted the experimental data as well as the previous linear fit, with the advantage of agreeing with the Bridgman sound speed at $U_p = 0$. Table III shows resultant data at low pressures calculated with constant γ . In this case the computed P_T and $\varepsilon_{p=0}$ values show improved agreement with static compressibility and thermodynamic data.

At pressures much higher than 0.25 megabars, the offsets between the Hugoniot and adjacent adiabats become larger. Table IV shows Hugoniot data for copper, computed from Eq.4.2 fitted to data of McQueen and Marsh,⁸ and Altshuler et al.⁹ Also shown are 0 °K isotherms, Gruneisen ratios and temperatures computed by McQueen and Marsh⁸ using the Dugdale-MacDonald relation, and by Altshuler et al.,⁹ who included the contribution of the electron potential. The two results compare very well, so that it may be surmised that the effect of the electron potential is negligible up to 1.5 megabars. The differences resulting from the use of the Slater relation, Eq.4.6a, instead of the Dugdale-MacDonald relation are also small, the difference in γ not exceeding 20 per cent over the entire range.

4.3 Low Stress Region

Shock Hugoniots have been determined for a few materials in the low stress region using the same experimental techniques as in the high pressure region, i.e., by inducing a plane loading wave in the sample under study by explosive means or plate impact, and measuring wave and material velocities. Providing that the wave profiles are steady, it is usually assumed that the Rankine-Hugoniot relations may be used to deduce stress and specific volume behind the wave from the wave velocity and material velocity behind the wave. However, in this case, the stress so deduced is the stress along the axis of motion. Since the

material may be expected to support a shear stress which is not negligible in this region, the stresses along principal axes perpendicular to the motion will differ from the longitudinal principal stress. For this reason, only one-dimensional slab symmetrical motion will be discussed in connection with elastic-plastic wave propagation, since for cylindrical or spherical symmetry, additional terms appear in the equations of motion, Eq.2.4.

At low stresses, two loading waves are observed, one traveling at elastic longitudinal wave velocity, and a second slower wave identified as a plastic wave. The second wave travels into a stressed and moving medium, so that the mechanical Rankine-Hugoniot relations become

$$V_1 - V = V_1 \frac{U_p - U_{P_1}}{U_s - U_{P_1}} \quad (4.14a)$$

$$\sigma_H - \sigma_1 = \frac{(U_p - U_{P_1})(U_s - U_{P_1})}{V_1} \quad (4.14b)$$

where $(\)_1$ refers to conditions ahead of the wave and σ here refers to the stress component in the direction of motion. The locus $\sigma_H(V)$ is again termed the shock Hugoniot.

A number of workers have given a simple theory of uniaxial strain for an isotropic material, based on linearized elastic-plastic theory.^{15,16,17} This may be summarized as follows.

In uniaxial strain, the principal components of natural strain are $(\epsilon_x, 0, 0)$; the principal components of stress are $(\sigma_x, \sigma_y, \sigma_y)$. It follows that any component of the deviatoric stress may be written $\alpha(\sigma_x - \sigma_y)$ where α is an appropriate constant. It is assumed that yielding is not influenced by the dilatational component of stress, but

$$P = P_0 V_s U_p$$

$$P = \sigma$$

$$P_0 = \text{DENSITY}, U_p = U_{FS}/2$$

depends only on the deviatoric components, and consequently on the value of $(\sigma_x - \sigma_y)$. The yield condition may therefore be written

$$(\sigma_x - \sigma_y)^2 = Y^2 \quad (4.15)$$

Hooke's Law will be written

$$d\epsilon_i = \frac{1}{2G} d\sigma'_i + \frac{1}{3K} d\sigma \quad (4.16)$$

relating the principal components of natural strain increment to the principal components of the deviatoric stress increment $d\sigma'_i$ and the dilatational stress increment $d\sigma$ where $\sigma = 1/3(\sigma_x + 2\sigma_y)$. Here G is the shear modulus and K the bulk modulus.

If the strain increment is divided into elastic and plastic components,

$$d\epsilon_i = d\epsilon_i^e + d\epsilon_i^p \quad (4.17)$$

and if the usual assumption is made that no volume changes result from the plastic components of strain

$$d\epsilon_x^p + 2d\epsilon_y^p = 0 \quad (4.18)$$

the principal components of the stress increment and strain increment in the elastic and plastic ranges may be written as in Table V, which shows also their dilatational and deviatoric components.

If the values from Table V are introduced into Hooke's Law, Eq.4.16, the following relations result:

$$\text{Elastic } d\sigma_x = (K + 4/3G) d\epsilon_x \quad (4.19)$$

$$\text{Plastic } d\epsilon_x^e = \frac{1}{3K} d\sigma_x \pm \frac{3K - 2G}{9KG} dY \quad (4.20a)$$

$$d\epsilon_x^p = \frac{2}{3K} d\sigma_x \mp \frac{3K + 4G}{9KG} dY \quad (4.20b)$$

and on addition of Eq.4.20a and 4.20b,

$$d\sigma_x = K d\epsilon_x \pm 2/3 dY \quad (4.21)$$

The upper sign in the above equations is appropriate when $d\sigma_x$ is positive, the lower when $d\sigma_x$ is negative.

Now for loading below the elastic limit, Eq.4.19 may be immediately integrated to give

$$\sigma_x = (K + 4/3G) \epsilon_x \quad (4.22)$$

where it is assumed that the moduli are constant over the elastic range. Equation 4.22 above may also be written

$$\sigma_x = F \epsilon_x \quad (4.23)$$

where $F = (K + 4/3G)$ may be termed the longitudinal elastic modulus.

This relationship holds up to the yield point, Eq.4.15, where

$$\sigma_{x_1} = \frac{F}{2G} Y_1 \quad (4.24a)$$

$$\epsilon_{x_1} = \frac{1}{2G} Y_1 \quad (4.24b)$$

()₁ referring to initial yield.

Beyond this point the material behaves according to Eq.4.21. However, it is not possible to integrate this immediately since the elastic moduli may be expected to vary significantly with compression in the plastic range. The difficulty can be overcome by relating the plastic loading behavior to the pressure-volume relation for pure dilatation. In the case of pure dilatation, if dv is the volumetric strain increment consequent upon a change of hydrostatic pressure dP then

$$dP = K dv \quad (4.25)$$

Notice that in uniaxial strain

$$v = \epsilon_x \quad (4.26)$$

Suppose that at the yield point in uniaxial strain the volumetric strain is v_1 so that $v_1 = \epsilon_{x_1}$ and suppose that the hydrostatic pressure which would give rise to the same volumetric strain in the case of pure dilatation is P_1 . Then from Eqs.4.24, 4.25, and 4.26 it follows that

$$\sigma_{x_1} - P_1 = 2/3 Y_1 \quad (4.27)$$

Now using Eqs.4.25 and 4.26, if it is assumed that K has the same value in Eq.4.21 and Eq.4.25, Eq.4.21 may be rewritten

$$d\sigma_x = dP \pm 2/3 dY$$

If there is no strain hardening, so that $dY = 0$, integration from a lower limit at the yield point gives

$$\sigma_x - \sigma_{x_1} = P - P_1$$

or, from Eq.4.27

$$\sigma_x = P + 2/3 Y_1 \quad (4.28a)$$

where σ_x and P are values corresponding to the same volumetric strain.

If strain hardening is included, the same integration gives

$$\sigma_x - \sigma_{x_1} = P - P_1 + 2/3 (Y - Y_1)$$

so that Eq.4.28a may now be written

$$\sigma_x = P + 2/3 Y \quad (4.28b)$$

where Y is the value of the yield function $(\sigma_x - \sigma_y)$ in uniaxial strain at the stress σ_x .

Fowles¹⁷ has further extended the argument in order to relate Y in Eq.4.28b to the yield stress in an engineering tensile test (uniaxial stress) in the presence of strain hardening. However, within the region considered here, the plastic strain under conditions of uniaxial strain is quite small in comparison with that possible in a tensile test up to fracture. One might therefore expect that strain hardening effects are very small for a material such as that investigated by Fowles, as is shown in fact by his data.

Upon unloading from a plastic state $(\sigma_{x_2}, \epsilon_{x_2})$, the material behaves elastically according to Eq.4.19. Again assuming K and G constant over the elastic unloading range, but not necessarily the same as at initial loading, we have

$$(\sigma_{x_2} - \sigma_x) = F(\epsilon_{x_2} - \epsilon_x) \quad (4.29)$$

If there is no strain hardening and no Bauschinger effect, the reverse yield point may be reached when

$$\sigma_{x_3} = \sigma_{x_2} - \frac{F}{G} Y_1 \quad (4.30)$$

Further unloading will be plastic, defined by

$$\sigma_x = P - 2/3 Y_1 \quad (4.31)$$

as for loading. The resultant stress-strain path is sketched in Fig.4.1.

Taking the available data on low stress Hugoniots, i.e., that of Fowles¹⁷ for hardened and annealed 2024 aluminum alloy, and that of Lundergan¹⁸ for a hardened 6061 aluminum alloy, one may plot $(\sigma_x - P)$ versus specific volume, where P is taken from the isentrope computed in the previous section, Fig.4.2 a and b. Drawn horizontal lines correspond to two thirds of the yield stress at .2 per cent offset from static tensile test data reported for each material, while the horizontal dotted lines represent two thirds of the yield stress obtained by fairing a horizontal line through the initial portion of the engineering stress-strain curves obtained in a tensile test for each material. It may be seen that the latter provides a quite reasonable approximation to the Hugoniot data in each case, within the experimental uncertainty, although the experimental points do suggest some strain hardening for the 2024 alloy. One might thus conclude that Eq.4.28a provides a reasonable approximation for these materials for the plastic loading path.

The previous theory rests on infinitesimal strain theory. Backman¹⁹ has indicated the order of error to be

expected from neglect of the second order terms in uniaxial strain. Actually, the foregoing theory does accommodate some correction, in that variation in elastic moduli with compression is permitted, the variation being taken from experimental data on a pure dilatational compression.

Thus, for the initial elastic loading portion, it is assumed that the strain is infinitesimal up to the yield point 1 (Fig.4.1). For the hardest aluminum alloy,¹⁸ the volumetric compression $1 - V/V_0 = 0.006$ so that this assumption seems reasonable.

It is possible to compare the elastic modulus F computed from elastic wave speeds measured by Lundergan¹⁸ to F computed from K given by Bridgman's static compressibility data, corrected to adiabatic conditions, and Poisson's ratio τ measured in a static tension test.

The experimental evidence (Fig.4.2) on plastic loading suggests that no great error accrues from the use of Eq.4.28a either, rather, the correction to the last term of Eq.4.28a arising from the correct treatment according to second order theory is less than the sensitivity of the quoted experiments. Thus, while it is desirable to use a second order theory throughout, as has been done by Backman,¹⁹ for our present engineering purposes Eq.4.28a appears to suffice.

Upon elastic unloading from a plastic state, use of Eq.4.29 with a suitable value of F rests on the assumption that the change in strain between points 2 and 3 (Fig. 4.1) on the elastic unloading portion is infinitesimal. This seems reasonable. With such an assumption, Birch,²⁰ using second order strain theory, has shown that Eq.4.29 is

in fact correct, and that the relations among local elastic moduli are the same as in first order theory. He has further given the variation in elastic moduli with compression as

$$F = (1 - 2\epsilon)^{5/2} [\lambda + 2\mu - \epsilon(11\lambda + 10\mu)] \quad (4.32a)$$

$$K = (1 - 2\epsilon)^{5/2} (\lambda + \frac{2}{3}\mu) (1 - 7\epsilon) \quad (4.32b)$$

where λ and μ are the Lame' constants. Evaluating the Lame' constants from static isothermal infinitesimal strain data, K has been computed. Corresponding values of P have been found by integrating $K = -V [dP/dV]$, and are listed in Table III. The encouraging agreement with computed isotherms P_T suggests that Eq.4.32a may also be a realistic description of the variation of the longitudinal modulus with compression, (when corrected to adiabatic conditions).

No direct experimental evidence is currently available to check the assumptions inherent in Eq.4.31 for the unloading plastic path, and caution is hence necessary in its use.

The foregoing theory has also neglected strain rate effects. The agreement of the quoted data with the rate-independent theory given above indicates that this assumption may suffice for present purposes for aluminum. However, this may not hold true for other materials. In particular, rate dependent behavior may be expected in steels exhibiting an upper and lower yield point in simple tension.

Analysis of wave propagation including a relaxation function leads to unsteady loading wave profiles.^{23,24} Conversely, one might expect that rate effects are absent when steady loading wave profiles are observed. Under

unsteady conditions, the Rankine-Hugoniot relations, Eq. 4.14, can no longer be used directly to obtain stress-strain information from measured wave and rear surface velocities. More complex methods of deducing constitutive equation data from measurable quantities must be evolved to deal with such materials. Further discussion of this point is considered outside the scope of this report.

4.4 Medium Stress Region

It is useful to fit the dynamic adiabat by a simple expression, either for use in the elastic-plastic constitutive equation, or for use alone in approximate calculations when the expected stresses are such that entropy changes across shocks are small, but elastic behavior is insignificant. A suitable expression is the Murnaghan expression

$$P = A \left\{ \left(\frac{V_0}{V} \right)^{\xi} - 1 \right\} \quad (4.33)$$

The corresponding Bulk Modulus is

$$K = -V \frac{dP}{dV} = A \xi \left(\frac{V_0}{V} \right)^{\xi} \quad (4.34)$$

Since entropy changes are neglected, we may use the Hugoniot data directly in fitting the constants in Eq. 4.33. For the linear U_s vs U_p fit, the Hugoniot $P(V)$ is given by Eq. 4.3. The corresponding Bulk Modulus is

$$K = -V \frac{dP}{dV} = -c^2 \frac{\frac{V}{V_0} \left[1 + s \left(1 - \frac{V}{V_0} \right) \right]}{V_0 \left[1 - s \left(1 - \frac{V}{V_0} \right) \right]^s} \quad (4.35)$$

or

$$K = -c^2 f\left(\frac{V}{V_0}\right)$$

A simple means of fitting the constants of Eq. 4.33 to Eq. 4.35 suggests itself. From Eqs. 4.34 and 4.35

$$-\xi \log \left(\frac{V}{V_0}\right) = k - \log f\left(\frac{V}{V_0}\right) \quad (4.36)$$

where k is a constant.

Thus the slope of a plot of $\log (V/V_0)$ vs $\log f(V/V_0)$ immediately yields the value of ξ , and moreover departure of the curve from linearity indicates the range of validity of the fit. A sample plot is shown in Fig. 4.3 for aluminum, the constants c and s (Eq. 4.35) being taken from a fit to the data of Walsh et al.⁷ The Murnaghan expression Eq. 4.33 is a good fit over the range $1 > V/V_0 > 0.6$, i.e. over a much wider range than that in which entropy variations may be safely neglected.

Some interesting comparisons are possible. Ryabinin³⁹ has found a relationship between the Murnaghan exponent ξ and the Gruneisen coefficient γ through the Debye theory

$$\xi = 2\gamma + \frac{1}{3} \quad (4.37)$$

Using $\gamma \simeq 2$ (Table II) for aluminum leads to a value of $\xi = 4.33$, which is in excellent agreement with the value $\xi = 4.34$ from Fig. 4.3.

Borelius⁴⁰ has also connected the Gruneisen ratio to compressibility data by thermodynamic considerations, and has obtained an average value of $\gamma_0 = 2.2$ for face-

centered cubic metals and $\gamma_0 = 1.2$ for body-centered cubic metals, which is in fair agreement with values of γ_0 obtained by Walsh et al.⁷ One, therefore, expects that the Murnaghan exponent will be near $\xi = 4.7$ for face-centered cubic metals and $\xi = 2.7$ for body-centered cubic metals. This leads to some interesting possibilities in scaling behavior in one material to that in another of the same crystal structure. An application will be mentioned in Section VII.

SECTION V

EXAMPLES OF WAVE-PROPAGATION CALCULATIONS

In the previous three sections, a discussion was given of two computational methods, viz. the finite difference method and the characteristic method, and three equations of state, viz. the Mie-Gruneisen equation^{4.4}, the elastic-plastic equation, and the Murnaghan equation⁴⁻³³. Solution of a particular problem requires choice of the method of computation, and equation of state best suited to the conditions of the problem. In this section, a few example calculations will be described in some detail, which will illustrate some of the advantages and disadvantages of each method of solution. No attempt will be made to lay down general rules for choice of computational method or equation of state, however, and each problem must be considered separately in this regard.

Computations were performed for the following plate impact problem:

Driver Plate Thickness,	0.9527 cm	³⁷⁵ "
Driver Plate Velocity,	1.262×10^4 cm/sec	414 FPS
Driver Plate Material,	Aluminum	"
Target Plate Thickness,	1.2634 cm	⁴⁹⁷ "
Target Plate Material,	Aluminum	"

The expected peak stress is very low, about 10 kilobars, and the plate thicknesses are such that rarefactions will not be able to attenuate the shock initially propagating into the target plate. Stress profiles at various times were required for several reverberations of the waves in the target plate.

Due to the many elastic-plastic wave interactions which occur on reflection of the wave systems at free sur-

faces, and on crossing of wave systems, the characteristic method was expected to be very complex, and not suited to automatic computation. A semimanual method was used, as described in Section IV. The elastic and plastic portions of the equation of state (Fig.4.1) could be approximated by straight line segments, due to the very small curvature of these portions over the small compression range encompassed by this problem. Nevertheless, the characteristic mesh consisted of more than 200 wave interactions. Some of the characteristics are shown in Fig.5.1.

Corresponding stress-Lagrangian position profiles at several times after impact are shown in Fig.5.2. Also shown are profiles computed by the finite difference method using several mesh sizes. Finally for comparison, wave profiles computed by the finite difference method using the Murnaghan equation, i.e., material with zero shear strength, are shown.

Several interesting observations may be made. The elastic-plastic interactions lead to much more dispersion of the loading and unloading waves than in a material of zero shear strength. The elastic-plastic interactions also lead to a reduction in peak stress on each subsequent wave reverberation. Both the wave dispersion and attenuation are reproduced in the finite difference solutions. The fine details of the waves are not reproduced, the finite difference solutions tending to smooth the discontinuities. Nevertheless, the gross features of the wave profiles are reproduced to a surprising degree, even by the calculation with the coarsest mesh size. Thus the peak stress, wavelength and total momentum are all approximated quite closely. The details of the elastic-plastic waves are reproduced to different degrees by calculations with different mesh sizes.

Only the calculation with the finest mesh size (350 meshes total) was able to approximate the main elastic-plastic discontinuities reasonably well.

In choosing the calculation method and mesh size, it is necessary to decide on the detail desired in the solution. The characteristic solution gives the most detailed representation but is extremely cumbersome and tedious in the present case. It is doubtful if the fine detail shown by the characteristic solution would actually be observed in a polycrystalline material where a certain amount of dispersion and smoothing may be expected due to the presence of grain boundaries, different crystal orientations, natural viscosity, etc. For the finite difference method, the computation time increases approximately as the inverse of the square of the mesh size, if rezoning or the time saving devices are not used. Thus, for a mesh size $\Delta r = 0.0063$ cm, the computation time, using an I.B.M. 7090 digital computer, was about 40 minutes. For a mesh size $\Delta r = 0.0126$ cm, the computation time was about 11 minutes. For a mesh size $\Delta r = 0.063$ cm, the computation time was only 1.8 minutes, most of which was taken up in input and output routines.

Neglecting the shear strength in the present problem leads to rather considerable error, since both the peak stress induced by the impact and the wave velocities are incorrect. At later times, the wave profiles bear little resemblance to the correct solution. Even the calculation with the coarsest mesh (35 meshes total) but with the elastic-plastic equation of state, gives a much better representation of the wave profiles.

Another computation was performed for the following plate impact problem:

Driver Plate Thickness,	0.3175 cm
Driver Plate Velocity,	1.63×10^5 cm/sec
Driver Plate Material,	Aluminum
Target Plate Thickness,	12 cm
Target Plate Material,	Aluminum

In this case, the higher driver plate velocity is expected to lead to a peak stress of about 146 kilobars. Entropy variations are expected to be small. On the other hand, the peak stress is much larger than the yield stress. Therefore the Murnaghan equation is likely to be adequate. In this particular problem, shock attenuation by the following rarefaction was of interest, and successive reflection at the target plate surfaces was not required. The characteristic method is ideally suited to this problem, and Fowles²¹ has given a simple analytical solution neglecting entropy variations.

Comparisons of Fowles' solution with three finite difference solutions are shown in Fig.5.3 where pressure-Eulerian position profiles are shown for six times after impact. The solutions were obtained for mesh sizes $\Delta r = 0.0397$; 0.0794 ; and 0.1058 cm, for which the driver plate contained 8, 4, and 3 meshes, respectively.

Some of the features inherent in the finite difference method are illustrated by Fig.5.3. The shock is spread over about four meshes, and therefore the head of the shock is retarded, compared to the exact solution. The rarefaction is also distorted, the tail being retarded, although the artificial viscosity was set zero on rarefactions. The net effect is that the peak pressure is attenuated more rapidly than in the correct solution. Partially off-setting this effect is the fact that the finite difference solution overshoots the peak pressure at the shock, and introduces a

series of oscillations into the subsequent pressure profile.

Inherent in the finite difference solution, therefore, is an uncertainty in the peak pressure and pulse width, the uncertainty increasing with mesh size. Nevertheless the gross wave shape is reproduced quite well. Calculations of momentum distribution are therefore likely to be handled quite well by the finite difference method, but calculations involving fracture criteria are much more sensitive to the peak pressure and pulse width, and the finite difference method may not be adequate if accuracy is desired.

It should be pointed out that much greater accuracy is necessary when the peak stress is attenuated by a large amount. For example, if the initial induced stress at the interface is 100 kilobars, and the uncertainties introduced due to inaccuracies in the equation of state and by the finite difference method are five per cent, then if the peak stress is subsequently attenuated to 10 kilobars, the uncertainty in the result will be of the order of 50 per cent. In calculations of fracture thresholds under such conditions, therefore, it is necessary to ensure great accuracy if the results are to be meaningful, and characteristic methods are preferred.

Introduction of shear strength into the equation of state does not lead to any significant changes in the finite difference solutions in this case. Only small differences would be introduced into the characteristic solution. The finite difference solutions with the above mesh sizes are not capable of reproducing these differences.

Other examples of wave propagation calculations are included in the next two sections.

SECTION VI

SPALL FRACTURE

One of the most important aspects of the response of solid bodies to intense impulsive loads is that internal fractures may be produced. In some cases where the fractures are close to a surface, pieces of the solid may be torn loose and fly off at considerable speed. This phenomenon is broadly termed spallation.

In order to predict the occurrence of spall fracture, it is necessary to know the time dependent stress distribution through the solid body. This may be computed from the loading and boundary conditions once an adequate constitutive equation has been found for the particular material under study. It is also necessary to know the fracture criterion for the material, i.e., conditions under which mechanical failure occurs.

This section will be devoted to a brief discussion of fracture criteria, and their evaluation.

6.1 Fracture Criteria

The most commonly used fracture criterion considers that failure occurs when the greatest normal tensile stress reaches a critical value. This is by no means the only fracture criterion in use. Other criteria are based on critical values of shear stress, relative elongation, or work done in deformation. If attention is restricted to one particular configuration, in this case uniaxial strain, then any one of these criteria may be chosen providing that the criterion is evaluated under identical conditions of uniaxial strain. The most convenient parameter in this case is the normal stress.

While this leads to a self-consistent fracture criterion under conditions of uniaxial strain, it cannot necessarily be related directly to fracture criteria obtained in other configurations, e.g., uniaxial stress.

The most convenient experiment for evaluating the fracture criterion under conditions of uniaxial strain is the plate impact experiment. A flat target plate of the material under study, of lateral extent large compared to its thickness, is impacted face on by a thin, flat driver plate. Uniaxial strain is maintained near the center of the plates for a sufficient time to produce tension stresses in the interior of the target plate. The magnitude and duration of the tension stresses may be controlled by choice of driver plate velocity and plate thicknesses.

A number of such experiments have been performed at various laboratories. Figure 6.1 shows sections through 1/4-inch thick copper target plates impacted at increasing velocities by 1/8-inch thick copper driver plates by Lundergan et al.²² Great care was exercised in these tests to ensure that the impact was plane and that air between the plates was removed (See Section VII).

At a driver plate velocity of 0.52×10^4 cm/sec, only a few isolated cracks appear in the expected spall plane. At a driver plate velocity of 0.896×10^4 cm/sec the cracking is much more extensive. It is interesting to observe that not all of the cracks lie on a sharply defined plane, and do not all join to form a smooth fracture surface. Rather, cracks lie on different planes and tend to overlap, leaving small tongues of material connecting the spall to the remaining target. At higher driver plate velocities, the cracking is apparently more severe, until at a driver plate velocity above 1.141×10^4 cm/sec the spall is completely

severed from the remaining target.

From the photomicrographs (Fig.6.1), it is clear that the target sustains increasing damage as the driver plate velocity, and hence the induced stress, is increased. It is very difficult to assess the degree of damage from the photomicrographs. It was felt that the residual strength of the target on the spall plane would give a good indication of the degree of damage. Consequently, small tension specimens were cut from spalled target plates kindly supplied by Dr.C.D.Lundergan of Sandia Corporation, and the stress necessary to separate the spall from the target was measured in each case. Specimens were mounted in special jaws in a tensile testing machine as shown in Fig.6.2.

Results are shown in Fig.6.3. Data from specimens cut from the same target showed considerable scatter with a tendency for the residual strength to be somewhat higher near the edges of the spalled region than in the center. Some uncertainty may have resulted from the fact that ferric chloride etchant had been introduced into the cracks during the metallurgical examination, and the etchant may have reduced the residual strength of the specimens. However, it was felt that the effect of the etchant was small, and more or less uniform in all the specimens, and did not invalidate the general trend of the data.

The trend of the data is clear. For driver plate velocities below about 0.5×10^4 cm/sec no damage is evident on impacted target plates, and the strength should be that of the virgin material. Increasing damage is sustained with increasing driver plate velocity up to a velocity of about 0.8×10^4 cm/sec. Beyond this velocity, no further change is apparent in the residual strength, and the only observable effect is a slight widening of the cracks (Fig.6.1), up to a

driver plate velocity of 1.41×10^4 cm/sec, at which velocity the spall is completely detached. Corresponding thresholds may be arbitrarily defined: these will be termed the lower fracture threshold, below which no damage is apparent in the target; the upper fracture threshold, above which the cracks are completely formed; and the spall separation threshold, above which the spall separates. For driver plate velocities above the spall detachment threshold, the velocity of the ejected spall is roughly linearly related to the driver plate velocity (Fig.6.4).

In order to study the fracture phenomenon further, it is necessary to inquire into the stress-time history at the fracture location. Unfortunately, the Hugoniot (Section IV) for this material has not been measured in the low stress region. It is only possible to make rough estimates of the stresses with the aid of a constitutive equation constructed from the dilatational adiabat from Section 4.2, and a handbook value of the yield stress. While this will not lead to very accurate quantitative data on the fracture stress, it can serve to illustrate qualitative aspects of the phenomenon.

The characteristic net for a typical experiment will appear as in Fig.6.5, where it is assumed that no fracture has occurred. (Some of the characteristics have been omitted for clarity.) Corresponding plots of the stress-time history at locations at the center of the target plate, and one quarter of the target plate thickness from the interface have been plotted in Fig.6.6. Qualitatively, the stress time profiles are nearly square waves. The magnitude of the tensile stress is directly related to the driver plate velocity. The duration of the first tensile cycle is directly proportional to the distance of the location from the interface (or free back surface), provided that no fractures occur. Moreover, as long as no fractures occur, the positive and

negative cycles will repeat with only minor modification until waves from the edges of the plates destroy the uniaxial strain configuration and/or the target plate strikes some object in its flight path.

Using the approximate equation of state described above, the magnitude of the stress in the first tension cycle corresponding to the lower fracture threshold is about 8.5 kilobars, and corresponding to the upper fracture threshold is about 14 kilobars.

Despite the apparent simplicity of the test configuration, interpretation of the observed phenomena is not at all straightforward. The fact that the target sustains increasing damage in the range between lower and upper fracture thresholds, as defined above, suggests that the fracture phenomenon is time dependent. Such time dependence is, of course, familiar from tensile tests carried out by many experimenters,^{25,26} over time ranges varying from milliseconds to months. Simple reaction rate kinetics has been applied to such relatively long time fracture data, as well as creep data, with considerable success.

By considering the probability of bond rupture under an applied load, it is possible to deduce an expression for the fracture time t_c , following arguments such as those of Beuche,²⁷ of general form

$$t_c = \frac{1}{\omega} \exp\left(\frac{\varepsilon(\sigma)}{kT}\right) \quad (6.1)$$

where ω is the vibrational frequency of the crystal lattice, and is thus the number of times per second that a particular bond reaches a condition under which rupture may occur, k is the Boltzman constant, T is the temperature, and ε is the magnitude of the activation barrier, which is a function of the applied stress σ .

Many experimenters, including Zhurkov et al,²⁵ have found that experimental creep and fracture data could be fitted by an expression

$$t_c = \frac{1}{\omega} \exp \left(\frac{\varepsilon_0 - \beta\sigma}{kT} \right) \quad (6.2)$$

Other experimenters, including Dorn,²⁸ noted that creep data could be fitted by an expression equivalent to

$$t_c = \frac{1}{\omega} \exp \left(\frac{\varepsilon_0}{kT} - \beta'\sigma \right) \quad (6.3)$$

i.e., with the constant β of Eq.6.2 proportional to temperature. Measured values of ε_0 range from the activation energy of sublimation to that of self-diffusion. Anderson²⁹ in a discussion of some of the apparent discrepancies in the literature has postulated a dual mechanism, self-diffusion dominating at low rates and high temperatures, when Eq.6.3 may be applicable, and sublimation dominating at high rates, with Eq.6.2 as the governing equation. Without entering into a discussion of these points, it might be noted that under brittle fracture conditions found in spallation, the sublimation process is likely to be the dominant one. Moreover, all of the Sandia experiments quoted above involve low stresses, so that the local temperature during fracture is very slightly below ambient temperature in all cases, in which case Eq.6.2 and 6.3 are equivalent.

Extrapolation of Eq.6.2 below $0(10^{-3})$ seconds is not necessarily valid. Observed cracks under spall conditions (Fig.6.1) are transgranular and appear to run continuously for 10 to 20 grain diameters. For very short fracture times, the crack propagation speeds must be very high, near the sonic velocity of the material. Waldorf³⁰ has suggested that the stress necessary to propagate cracks at such ve-

locities must be higher than that given by Eq.6.2, although the rate of increase proposed by Waldorf seems too high. Valluri and Williams,³¹ in a discussion of spall fracture, point out that the lower limit on the fracture time must be of the order of the vibrational period of the crystal lattice, i.e. $0(10^{-13})$ seconds, and the corresponding stress must be the theoretical strength of the material, in this case about 200 kilobars. Experimental evidence in support of such a limit has recently been obtained by McQueen and Marsh,⁴¹ who have obtained a limiting tensile strength of 233 kilobars. This stress is again much higher than that predicted by Eq.6.2.

Unfortunately, relatively long time creep and rupture data is not available for the material under consideration, i.e. half-hard E.T.P. copper. However, the straight line in Fig.6.7 was plotted from Eq.6.2, using the sublimation energy, the lattice vibrational frequency, and a value of β such that the curve fitted the "static" ultimate stress (handbook value) in the range 1 to 10^2 seconds. The resultant value of β is of correct order as predicted by consideration of ionic volumes. The above considerations then lead to the expectation that the qualitative behavior at shorter times will be roughly as shown by the dotted extension in Fig.6.7.

Clearly Fig.6.7 is merely qualitatively correct, and is intended only to further the discussion of the fracture mechanism. The behavior suggested by Fig.6.7 would lead to a reasonably consistent explanation of the phenomena observed in spallation experiments.

For stresses below the lower fracture threshold, i.e. below about 8 kilobars, the time required for fracture would be in excess of $0(10^{-3})$ seconds. In the experiment, rarefaction waves from the edges of the plates attenuate stresses in the target in times of order 10^{-5} seconds. Thus no damage would be noticeable in the target.

On the other hand, if the tensile stress is in excess of the upper fracture threshold, i.e. about 14 kilobars, the fracture time would be less than $0(10^{-8})$ seconds, which is very short compared to the duration of the first tensile cycle, i.e. $0(10^{-6})$ seconds. Thus to all intents and purposes, fracture would occur instantaneously on the time scale of the experiment, and the fracture time can be ignored.

In the region between the lower and upper fracture thresholds, however, the fracture time would be significant, and would lead to just the type of behavior observed, i.e. increasing damage for increasing stress level. Interpretation of the fracture data in this region is very difficult because the loading is now no longer simple. As the cracks grow they will originate release waves which affect the stress wave propagation in the target, and the wave profiles shown in Fig.6.3 will be profoundly altered. There is also the possibility that subsequent reverberations of the stress waves would lead to further growth of the fractures.

The effect of loading time on the fracture formation process should be observable in the region between lower and upper fracture threshold, and various experiments have been proposed to observe the effect. The duration of the first tensile cycle can be varied by changing the geometrical scale of the experiment. Due to experimental difficulties, the scale could be conveniently altered at most by a factor of 200, i.e. first tensile cycle durations from about 2×10^{-8} seconds to 5×10^{-6} seconds. If Fig.6.7 is reasonably correct, the upper fracture threshold would alter by only 10 or 20 per cent in this range. Thus, determination of upper fracture threshold by measurements of residual strength (Fig.6.3) would have to be carried out very carefully, if a fracture time effect is to be observed. Conversely, if a fracture time effect is not observed in relatively crude ex-

periments, this would serve as verification that Fig.6.7 is qualitatively correct, i.e. that the slope in the vicinity 10^{-8} to 10^{-6} seconds is not very much greater than shown. Preliminary experiments^{22,32} have failed to detect a time dependence.

There is an important difference between the relatively long time tensile tests, results of which lead to expressions of the form of Eq.6.2, and the spall experiments. The former experiments are usually carried out under dead weight loading. Thus, once a mechanical instability has formed, the test is carried out to complete failure under constant load, or, as in the tests of Zhurkov,²⁵ under a load programmed to yield a constant nominal true stress, defined as the load divided by the neck area.

On the other hand, in the spall experiment, as the fractures develop, widening of the cracks may be expected to initiate release waves which will tend to attenuate the nominal stress. One thus expects a difference in behavior during the last stages of the fracture process. Above the upper fracture threshold, the cracks may be expected to grow very rapidly, but widening of the cracks may be expected to relieve the nominal stress almost immediately. Since cracks are initiated at suitable nuclei dispersed randomly in the material, and their propagation directions are influenced by local grain structure, the cracks are not all coplanar, and do not all join smoothly, and the small interconnecting tongues observed in Fig.6.1 remain. At this point the spall is moving at nearly driver plate velocity, while the remaining target is at nearly zero velocity. Metallurgical observations reveal that the tongues appear to have been drawn out plastically, and occasionally evidences of local melting are observed at the tips of ruptured

tongues. Thus the final stage of the fracture process appears to involve a "quasi-static" plastic extension of the tongues, and, when the imparted impulse is sufficiently high, a ductile rupture of the tongues occurs.

Complete separation of the spall from the target is generally complicated by edge effects. Figure 6.8 shows a section near the edge of the target plate. In the Sandia series of tests, a groove was cut to the expected depth of the spall in order to delimit the test area. Since the groove introduces a lateral free surface, which must remain at zero stress, the maximum tension stress, and hence the fractures, are not developed adjacent to the groove. This ring of undamaged material must thus be sheared if the spall is to be detached.

When no groove is provided, the cracks are limited to the area of the target plate which is subjected to the tension stress, and in order to detach the spall it is again necessary to shear material between the edge of the cracked region and the surface. In similar tests with and without grooves, roughly the same driver plate velocity was required to detach the spall. Tests have also been performed in which the test area was delimited by a circumferential cut clear through the target plate. The test specimen was a good fit in the surrounding plate. In this case, cracks are formed right up to the edge of the test piece and edge effects are eliminated. A reduction in spall detachment threshold of 15 per cent was observed.²²

It should be noted that the effect of the edge shear ring is relatively more important when the spall is thick, and when the spalled area is small. One would thus expect a size effect on spall detachment threshold. Such a size effect has in fact been observed.

While the lower and upper fracture thresholds may be defined in terms of the maximum developed tensile stress, and appear to be only weakly dependent on stress duration, the spall separation threshold will be a function of the target geometry and loading configuration. Not only will the spall separation threshold be a function of spall size, and edge restraint, but also of the number and strength of interconnecting tongues. Thus the grain structure, which determines the crack configuration should be very important. However, equally important will be the planarity of the stress wave system in the target plate. If the waves in the target plate are very perturbed, for example because of a rough or buckled driver plate or a roughened rear surface of the target, cracks would be nucleated at more widely separated points, and a much higher impulse would be required to separate the spall.

For stresses beyond the upper fracture threshold, it is unlikely that the tension stress, calculated by assuming that no fractures occur, would actually be experienced by the material on the spall plane. It is, therefore, not correct to speak of a spall separation threshold stress. Rather, based on the above hypothesis, the separation mechanism depends on the relative average velocities of the spall and remaining target. These in turn depend on the stress wave profiles in the spall and target at the time the fractures occur. A single quantity which is adequate to serve as a measure of the spall separation threshold has so far not been defined, but it is possible that the relative average velocity of spall and target may prove suitable for this purpose.

The spall velocity, when separation occurs, may also be expected to be a function of the edge restraint and

number and strength of interconnecting tongues. In experiments in which no delimiting grooves or rings are provided there is considerable scatter in the measured spall velocity, presumably due to random differences in edge restraint. In the Sandia series of experiments, the scatter is not too great (Fig.6.4). Extrapolation of the curve to the abscissa indicates that considerable energy is expended in forming the completed fracture. However, insufficient data is available to determine the amount of energy expended in the various modes, i.e. formation of the cracks, rupture of the tongues, shearing of the edge restraint, and contribution to the remaining target kinetic energy. More work is necessary to determine the energy balance before rational predictions of spall velocity can be made.

6.2 Summary

The preceding discussion has necessarily been qualitative and speculative, due to the lack of careful experimental data. Nevertheless a hypothesis has been advanced which is in accord with most of the experimental observations. The most important deductions of engineering importance are the existence of three thresholds; i.e., the lower and upper critical fracture threshold, and the spall separation threshold. Corresponding stresses may be assigned to the first two thresholds, but not to the last.

1. For stresses below the lower critical fracture threshold, no effect on the target material is evident, either under low powered metallurgical examination, or in load carrying capacity. This threshold is the simplest to determine experimentally.

2. For conditions above the upper critical fracture threshold, fully formed cracks are observed on the

spall plane, but the spall is not necessarily detached from the target. The residual load carrying capacity of the spall plane depends on the grain structure of the material and the planarity of the stress waves which gave rise to the cracks, and may vary very widely. The upper fracture threshold should be weakly dependent on loading time, and thus on the geometrical scale of the experiment, but for engineering purposes, it is likely that this variation can be neglected.

3. The spall separation threshold defines conditions under which the spall separates from the target. This threshold is of prime engineering importance, but is the most difficult to determine. A single quantity to serve as a measure of the spall separation threshold has so far not been found. The spall separation threshold will be a function of:

- a) the relative average velocity of spall and remaining target at the time of crack formation, and thus of the stress wave profiles.
- b) the strength of interconnecting tongues between adjacent cracks formed by the stress waves, and hence of the grain structure, and planarity of the stress waves which gave rise to the crack.
- c) the edge restraints.

Variations of more than an order of magnitude have been observed in this threshold.

4. The spall velocity will be a function of the kinetic energy entrapped in the spall, and hence on the wave profile at the time that the fracture is completed. The wave profile will be affected by the fact that energy is necessary to form the fracture.

SECTION VII

EFFECT OF AIR BETWEEN IMPACTING FLAT PLATES

An experimental technique, which has been widely used for studying wave propagation and spall fracture, involves impacting a flat plate of the material under study with a thin, flat driver plate. Many such experiments have been carried out in which the driver plate is propelled by an explosive charge or exploding foil, without provision for removing the atmospheric air between driver plate and target. Since the air is progressively compressed as the driver plate approaches the target, it might be expected that the wave profile induced in the target plate will differ significantly from that induced in the absence of air. It is desirable to investigate this effect.

Evidently, the motion of the air will be very complex, since the plates are of finite size, and the gap around the edges is usually unsealed. The resultant three-dimensional flow would be extremely difficult to analyze.

In order to fix an upper limit on the effect, a simple one-dimensional analysis was undertaken. This would be directly applicable if the edge gap were sealed. For an unsealed gap, the unsteady air motion is such that more air will flow from the gap near the edges of the plate, and the one-dimensional analysis would be approached only near the center of the plate. Near the edges, conditions would more nearly approach conditions with no air present, and the induced wave profiles would therefore vary from the center to the edges of the plate, leading to complex three-dimensional stress wave profiles in the target.

Attention was focused on impact in aluminum driver

and target plates, with expected peak pressures of the order of 100 kilobars. Thus a simple equation of state $P = f(V)$, fitted to the experimental Hugoniot (Section 4.2) was used, and wave propagation in the plates was analyzed using the method of characteristics (Section III). While the analysis can be easily extended to lower stresses by using an elastic-plastic equation of state, much higher pressures could be analyzed only if entropy changes are allowed, either by using the finite-difference method, or by extending the characteristic method to accommodate entropy variations.

7.1 Perfect Gas Analysis

In order to investigate the probable magnitude of the effect, it was first assumed that the air behaved as a perfect gas throughout the motion. It was also assumed that the driver plate started into motion impulsively. When explosive propulsion techniques are used, the driver plate acceleration is very high, so that the compression wave in the air ahead of the driver steepens into a shock very rapidly, and actual conditions probably approach the idealization after only a few millimeters of driver plate motion.

At the velocities investigated, the pressure in the air behind the first shock is quite low. It was assumed that the driver plate was in a stress-free condition at this time; i.e., that stress waves due to propulsion have damped out before the pressure in the entrapped air becomes appreciable.

The shock wave preceding the driver plate will reflect successively at the target and driver plates, raising the pressure in successive steps, and inducing stress waves in the plates (Fig. 7.1). Evans and Evans³³ have shown that under conditions of successive shock reflection between approaching rigid walls, the bulk of the entropy rise occurs

in the first four shock compressions, and that the subsequent motion is very nearly isentropic. Since the pressure in the air is still relatively low at this point, the problem was simplified as follows. The first four shock reflections were treated by the method of Evans and Evans, assuming the plates to be rigid, with the driver plate moving at constant velocity. In the subsequent motion, the air was assumed to behave isentropically, and the transit times of waves across the air gap were neglected, but the plates were considered compressible. A somewhat similar approximation has been made by Winter,³⁴ and has been found to give good results in an analysis of the motion of a rigid piston in an air-filled tube.

Evans and Evans give the following relations for the pressure P and specific volume V behind the n th shock relative to initial conditions:

$$\pi_n = \frac{P_n}{P_0} = \prod_{j=1}^n \left[\frac{\lambda + \mu + j}{\lambda + j - 1} \right]$$

$$\frac{\rho}{\rho_0} = \prod_{j=1}^n \left[\frac{\lambda + \mu + j - 1}{\lambda + j} \right]$$

where

$$\lambda = \frac{\mu + 1}{\pi_1 - 1} \text{ and } \mu = \frac{\gamma + 1}{\gamma - 1}$$

Here ρ is the density of the air, π_1 is the pressure ratio across the first shock and γ is the ratio of the specific heats of the air, taken to be 1.4. The value of π_1 is obtained from the initial driver plate velocity by the Rankine-Hugoniot relations (for the air shock). Representative results are listed in Table VI for several

driver plate velocities.

During the subsequent motion, the air is assumed to be described by the isentropic relation

$$\frac{P}{\rho^\gamma} = \frac{P_4}{\rho_4^\gamma} = \text{constant} \quad (7.1)$$

where $()_4$ pertains to conditions after the fourth shock reflection.

In order to use the method of characteristics, it is now only necessary to modify the interface condition Eqs. 3.12a and 3.12b, Section III, by specifying that the interface pressure is given by Eq. 7.1 and

$$\frac{\rho}{\rho_0} = \frac{2X_0}{R - R'} \quad (7.2)$$

Here R is the Eulerian position of the surface, $()'$ refers to the right-hand plate and $2X_0$ is the initial plate spacing before commencement of the motion, at which time the initial (ambient) air density is ρ_0 .

The resultant equations, one each of Eqs. 3.8, 3.9, and 3.13 for each plate, together with Eqs. 3.10, 3.11, 7.1, and 7.2 are implicit. The simplest practical method of solution is to estimate the positions of the surfaces by modifying Eqs. 3.9 and 3.13 to

$$\frac{r_{m,m} - r_{m-1,m}}{t_{m,m} - t_{m-1,m}} = c_{m-1,m} \quad (7.3)$$

$$R_{m,m} = R_{m-1,m-1} + U_{m-1,m-1} (t_{m,m} - t_{m-1,m-1}) \quad (7.4)$$

and similarly for the right-hand plate. The equations may now be rendered explicit. The solution is then refined by iteration using Eqs.3.9 and 3.13. It has been found that one iteration is generally sufficient.

It is clear that the above analysis is quite tedious, since each case must be analyzed separately. In order to investigate the behavior in some more detail, the problem was simplified as follows. Both plates were taken to be made of the same material. Furthermore, it was assumed that no characteristics reached the interface from elsewhere in the plates during the entire isentropic compression process, such as, for example, characteristics reflected from the free surface of the driver plate. The Eulerian characteristic net would therefore appear as in Fig.7.1.

The problem can then be rendered symmetrical by the transformation

$$u = U - \frac{1}{2} U_0 \quad (7.5a)$$

$$x' = R' - \frac{1}{2} (R_0 + R'_0) - \frac{1}{2} U_0 t \quad (7.5b)$$

and similarly for the left-hand (driver) plate. Here U_0 is the initial driver-plate velocity, R_0 and R'_0 are the initial surface positions, and initial conditions $()_0$ apply at time $t = 0$ when the driver plate motion starts. Isentropic compression thus begins at the fourth shock reflection, i.e. at $t = t_4$, $x' = X'_4$ given by

$$t_4 = \frac{2X'_0}{U_0} \left[1 - \frac{\rho_0}{\rho_4} \right] \quad (7.6a)$$

$$X'_4 = X'_0 \frac{\rho_0}{\rho_4} \quad (7.6b)$$

The Eulerian characteristic net now appears as in Fig.7.2.

The experimental Hugoniot (from Section IV) has been fitted by the empirical expression

$$P = A \left[\left(\frac{V_0}{V} \right)^\xi - 1 \right] \quad (7.7)$$

Thus the Riemann variable is given by Eq.3.3 as

$$L = \frac{2}{\xi - 1} \sqrt{\xi A V_0} \left(\frac{P}{A} + 1 \right)^{\frac{\xi-1}{2\xi}} \quad (7.8)$$

Confining attention to the right-hand plate, we have the definition

$$\frac{dx'}{dt} = u \quad (7.9)$$

Introducing nondimensional parameters

$$\tau = \frac{u_0 t}{x'_0} - 1 \quad x = \frac{x'}{x'_0} \quad (7.10)$$

Eq.7.9 becomes

$$\frac{dx}{d\tau} = \frac{u}{u_0} \quad (7.11)$$

Note that in these coordinates, impact in the absence of air would occur at $\tau = 0$, $x = 0$.

A simple compression wave is induced in the plate for which the Riemann invariant is

$$u - L = u_0 - L_0 \quad (7.12)$$

By Eqs.7.8 and 7.12, Eq.7.11 becomes

$$\frac{dx}{d\tau} = 1 - \frac{2\sqrt{\xi}}{\xi - 1} \sqrt{\frac{V_0 A}{u_0^2}} \left[1 - \left(\frac{P}{A} + 1 \right)^{\frac{\xi-1}{2\xi}} \right] \quad (7.13)$$

The surface pressure P is determined by the pressure of the entrapped air, which is a function of the spacing, i.e. by Eqs. 7.1 and 7.2

$$\frac{P}{P_0} = \pi_4 \left(\frac{x_4}{x} \right)^\gamma \quad (7.14)$$

So that, finally, the differential equation of motion of the surface is

$$\frac{dx}{d\tau} = 1 - \frac{2\sqrt{\xi}}{\xi - 1} \sqrt{\frac{V_0 A}{u_0^2}} \left\{ 1 - \left[\pi_4 \frac{P_0}{A} \left(\frac{x_4}{x} \right)^\gamma + 1 \right]^{\frac{\xi-1}{2\xi}} \right\} \quad (7.15)$$

This expression is best integrated numerically. Once $x(\tau)$ has been found, $P(\tau)$ may be found directly from Eq. 7.14.

Independent parameters in the solution are $(u_0^2/V_0 A)$ and (P_0/A) , i.e., the initial driver plate velocity and initial air pressure, nondimensionalized with respect to material properties of the plates. Equation 7.7 has the interesting feature that most face-centered cubic metals may be fitted by using a value of ξ near 4.3, while most body-centered cubic metals may be fitted by using a value of ξ near 2.7. The quantities x_4 and π_4 are, however, functions of u_0 . Care is necessary in scaling from one material to another, and such scaling is not generally convenient. Geometric scaling, expressed by Eq. 7.10 is, of course, very useful.

7.2 Real Gas Analysis

The chief objection to Eq.7.15 is that air temperatures become very high, and the perfect gas assumption made in its derivation may be expected to be poor. Computations based on real gas behavior were therefore carried out. The initial shock reflection process between rigid walls was computed using Feldman's Molier chart³⁵ according to the method of Stollery and Maul.³⁶ Results for several cases are given in Table VI for comparison with results of the perfect gas analysis.

In order to include real gas behavior in the subsequent motion, real gas properties for equilibrium air tabulated by Hilsenrath and Beckett^{37,38} were used in the numerical integration in place of Eq.7.14. In this case, individual solutions must be obtained for each initial pressure, although geometrical scaling is still valid.

Solutions using the perfect gas analysis and the real gas analysis are compared in Fig.7.3, using as an example aluminum plates with $\xi = 4.266$, $A = 188.96$ kilobars, and $V_0 = 0.359 \text{ cm}^3/\text{gm}$, and with initial conditions $P_0 = 1.013$ bars, or 1 atmosphere, and $U_0 = 1.5 \text{ mm}/\mu\text{sec}$. Pressures rapidly become very high. For high temperature air at very high density, the polytropic gas law with γ near 1.4 might be assumed to yield a reasonable approximation to the real gas properties. A further calculation was performed, treating the shock process by using real gas properties, but assuming the isentropic compression law to be given by the perfect gas law Eq.7.14. Thus, Eq.7.15 was reintegrated using π_4 and x_4 given by the real gas analysis of Stollery and Maul. The resultant curve is also entered in Fig.7.3. It may be seen that while the results of the perfect gas and real gas analyses show poor agreement, the results of the real gas

shock-perfect gas compression analysis compare quite reasonably with those of the real gas analysis. Subsequent solutions were therefore obtained using real gas properties for the shock process, and perfect gas properties for the subsequent isentropic compression.

Representative results are shown in Figs.7.4 and 7.5 in which the initial driver plate velocity is varied at a constant initial air pressure of one atmosphere, again taking as an example aluminum plates. Figure 7.4 shows surface trajectories. In the absence of air, the nondimensionalized trajectory would be a straight line inclined at 45 degrees, the impact occurring at $\tau = 0$, $x = 0$. Figure 7.5 shows corresponding pressure profiles. While the pressure rise occurs in about the same nondimensional time τ , at each of the initial driver plate velocities shown, the real time t is inversely proportional to the initial velocity. The effect of the air in degrading the wave profile is thus more serious at lower driver plate velocities.

Also shown in Figs.7.4 and 7.5 are profiles for an initial driver plate velocity of 1.5 mm/ μ sec, but for an initial pressure of 1/100 atmosphere. As expected, the effect of the air is much reduced. It was at one time thought that the effect of air in an explosively driven plate experiment, in which the driver plate travel is only about 2 cm, could be modeled by a plate experiment in an air gun, in which the driver plate travel is about 200 cm, by reducing the initial entrapped air pressure in the air gun in inverse proportion to the initial spacing. While it is evident from Eq.7.15 that such scaling is not valid, a more graphic illustration is afforded by Fig.7.6 in which the pressure profiles shown in Fig.7.5 have been expanded to a real time base. (Zero time has been assigned arbitrarily to each profile to

allow presentation on a common scale.) The pressure profile is considerably more degraded for the air gun case ($P_0 = 1/100$ atm, $2X_0 = 200$ cm). Results of analyses, using real gas properties throughout, are also shown for comparison.

7.3 Subsequent Wave Profiles

Thus far, only pressure profiles at the interface have been considered. A gradually increasing compression wave is induced in both the target and driver plates. As the compression waves propagate into the interior of the plates, they will steepen and eventually form shock waves. Thus, at some distance in the interior, the effect of the air is no longer discernible. In order to follow this process, the waves propagating into the plates were analyzed by the method of characteristics outlined in Section IV, treating shock waves as isentropic compressions in the weak shock approximation. Resultant pressure-real time profiles at various stations in the plates are shown in Fig. 7.7 for each of the four initial velocities investigated. Thus, at an initial driver plate velocity of $1.5 \text{ mm}/\mu\text{sec}$ for example, the compression wave has steepened into a shock in 2 mm of travel, except for a small forerunner. However, at an initial driver velocity of $0.35 \text{ mm}/\mu\text{sec}$, a shock is not fully formed until the pulse has propagated 40 mm.

If the driver plate thickness is greater than the distance which the compression wave must travel in order to steepen into a shock, then no effect due to the air will be apparent on the subsequent wave profile travelling into the target (except for a small effect due to the forerunner). However, if the driver plate thickness is less than this distance, then the release wave reflected from the free surface of the driver plate will be affected. Thus, if the

compression wave arriving at the free surface of the driver plate has some profile of finite width, this profile is transferred to the release wave reflected back into the driver plate. The release wave now will no longer steepen, but degrade further, and on passing into the target will be expected to show a different profile from that induced in the target in the absence of air.

An analytical solution of the problem requires solution of the characteristic net resulting from the reflection of the compression wave at the driver plate free surface. A sample calculation has been carried through for the following initial conditions $P_0 = 1$ atm, $2X_0 = 2$ cm, $U_0 = 1.5$ mm/ μ sec, and driver plate thickness 0.8 mm, again with aluminum plates. The characteristic mesh is shown in Fig.7.8.

The corresponding pressure-real time profile at the interface is shown in Fig.7.9. The solution (assuming an isentropic shock) for the no-air case is also shown for comparison. The pressure-Eulerian distance profile is shown in Fig.7.10, at a time 0.357 microseconds after impact in the absence of air (13.693 microseconds after start of driver plate motion). It may be seen that the only significant difference introduced by the presence of air is a rounding of the head of the rarefaction wave. However, this rounding leads to important differences as the rarefaction catches up to the shock, and the shock is attenuated. In particular, the peak pressure will be attenuated much sooner, and the peak pressure-distance curve will not exhibit a well-defined "catch-up" distance, the corner (see Section V) being rounded.

The passage of the release wave across the interface containing the air layer was accomplished in the above

calculation by simply ignoring the presence of the air, and allowing the characteristics to propagate across the interface without refraction. While this is a good approximation during the initial part of the pressure release process, it is not strictly valid for the final part. As the pressure at the interface drops, the air will expand, causing the driver plate to rebound. A partial analysis was undertaken in which the correct interface conditions (Eqs.3.8, 3.9, 3.10, 3.11, 3.13, 7.1, and 7.2) were used, iterating at each step. The solution followed the profile of Fig.7.9 down to about 10 kb, at which point the divergence became serious. The characteristic mesh is quite complex due to further wave reflections from the driver free surface, and the solution was discontinued at this point.

In the previous calculation, the first release wave from the free surface of the driver plate arrived back at the interface after the compression of the air had been completed, (see Fig.7.8). Thus, the compression was handled by Eq.7.15 and the reflection of the compression wave at the driver free surface was handled separately. More serious degradation of the wave profile is to be expected if the reflected release wave arrives at the interface before the peak pressure has been attained there. Equation 7.15 can now no longer be used, and a characteristic method using the correct conditions at the interface is required. A wave profile, computed on this basis for the following initial conditions is shown in Fig.7.11; $P_0 = 1 \text{ atm}$, $U_0 = 0.35 \text{ mm}/\mu\text{sec}$, $2X_0 = 2 \text{ cm}$, driver plate thickness 1 mm. The peak pressure attained is 22 per cent below that attained in the absence of air, or with a much thicker driver plate.

There will thus be three types of behavior which might be observed. If the driver plate is sufficiently

thick, virtually no effect due to the air will be apparent, since the compression steepens into a shock before reaching the free surface of the driver plate. For thinner driver plates, the wave induced in the target will show some rounding at the head of the rarefaction, and hence will attenuate somewhat more rapidly as the rarefaction overtakes the shock wave. For very thin targets, strong rarefaction waves arrive at the interface from the rear surface of the driver plate before the peak pressure has been attained, and the pressure attained in the absence of air is never attained at the interface. Approximate boundaries can be found for the regions in which each of these types of behavior may be expected, based on the previous calculations. These boundaries are shown in Fig. 7.12 for the range of velocities investigated in the present examples, and for aluminum driver plates, with an initial air pressure of 1 atmosphere. Geometric scaling is valid, and the driver plate thickness has thus been nondimensionalized with respect to one half the initial plate spacing (X_0). Points representing the conditions corresponding to the profiles of Figs. 7.9 and 7.11 have been inserted.

It must be noted that this diagram cannot be scaled to other materials or initial pressures, and in general, it is highly advisable to carry out a complete calculation for each case of interest.

In order to assess whether the effect of side leakage is important near the center of the plates, calculations were made of the distance travelled by sound waves during the compression cycle. Thus the quantity

$$\delta = \frac{d}{X_0} = \sum_n \frac{c^n \Delta t^n}{X_0} \quad (7.16)$$

where $c = \frac{dp}{dp} |_s$ is the sonic velocity in the air, was summed over all time steps n in the numerical integration of Eq. 7.15, from time t_4 . For each of the four initial velocities considered above at an initial pressure of one atmosphere, the nondimensional distance δ was in excess of 10. Thus, for example, for plates 5×5 cm in lateral extent, with a 2 cm initial spacing, release waves from the edges are able to travel to the center and back at least twice during the compression cycle. The idealized one-dimensional analysis therefore provides only an upper limit. In fact, considerable leakage must occur in most practical cases. However, without a detailed three-dimensional analysis of the air flow, it is not possible to determine the quantitative departure from the results of the idealized one-dimensional analysis.

7.4 Summary

It is convenient to summarize the main conclusions of the analysis as follows:

1. In analyzing the air effect, real gas effects must be included. Assuming perfect gas behavior for the shock compression phase leads to large errors.
2. The phenomenon may be scaled geometrically, in which case time must be scaled with the geometric scale ratio. Scaling of initial pressure and velocity involves plate material properties. Initial pressure and velocity, nondimensionalized by material properties, (P_0/A) and $(u_0^2/V_0 A)$, are independent parameters.
3. Degradation of wave profiles is more serious for lower initial velocities, and for more compressible materials (lower A). While the effects should be quite

small for most normal metal plate systems. except for very thin driver plates, the effect may be much more important for plastics.

4. Magnitude of the effect depends on the driver plate thickness, other initial parameters being constant. For relatively thick driver plates, no effect will be observable once the entire pulse has entered the target. For thinner driver plates, the only important effect will be the rounding of the head of the release wave entering the target, with a consequent large reduction in catch-up distance (start of attenuation of the shock by the release wave) and subsequent more rapid attenuation of the shock by the release wave. For very thin driver plates, the peak pressure at the interface will be attenuated by release waves reflected from the rear surface of the driver plate, and the peak pressure induced in the absence of air will never be attained. As the pulse propagates into the target, subsequent attenuation is also very much more rapid.

5. Since the most important effect of air is in altering the wave profile, it is not possible to counteract the effect by increasing the driver plate velocity. Such action will only lead to a distorted wave of higher amplitude, which cannot have the same attenuation characteristics as a pulse induced in the absence of air.

6. In almost all practical cases, it is expected that side leakage of the air will be important, and therefore the foregoing one-dimensional analysis will provide only an upper limit on the effect near the center of the plates. Leakage will affect areas near the edges of the plates to a much greater degree than in the center, and the wave profile will more nearly approach that induced in the absence of air. The result will be a complex three-dimen-

sional nonplanar wave system propagating into the target. Nonplanarity of the wave system may in itself affect such phenomena as spall.

7. In the light of the foregoing, it is concluded that if the present analysis shows that the air effect is important in a particular series of tests, then the resultant data from those tests is unreliable. The only course is to remove the air in the experiment.

SECTION VIII

CONCLUSIONS

In an analysis of the effect of a distributed intense impulsive load on a structure, it is necessary to compute the stress wave propagation through the thickness of the structure. Two methods, which have been discussed, are available viz. the finite difference method (Section II) and the characteristics method (Section III). Furthermore several approximate constitutive equations have been constructed (Section IV) which are valid in different ranges.

For two aluminum alloys for which data exists, little or no increase in yield strength is apparent, and it has been possible to relate the dynamic constitutive equation for moderate stresses to static material properties via second order finite strain theory.

Success of the analysis of stress wave propagation depends on the correct choice of computation method and constitutive equation. Several examples have been given (Section V), but no general rules can be formulated.

Spall fracture has been discussed in some detail (Section VI). For copper, for which some unambiguous experimental data is available, only a moderate increase in fracture threshold is observed at the high rates involved in spallation. The fracture threshold must be determined experimentally, the plate impact experiment being ideally suited to this purpose.

The effect of air in the plate impact experiment has been analyzed in detail (Section VII), but it is only possible to obtain an upper limit on the effect. Therefore, if an analysis shows the air effect to be important in a

particular experiment, the analysis cannot be used to correct the resultant data, rather the experiment should be repeated in a vacuum.

For materials other than the aluminum and copper alloys for which data exists, further experimental work is required to determine if their behavior is similar. The constants in the constitutive equation and fracture criteria for these materials must be evaluated experimentally before an analysis of stress wave propagation and spallation can be undertaken.

REFERENCES

1. Leech, J.W., Pian, T.H.H., Witmer, E.A., and Herrmann, W. Dynamic Response of Shells to Externally Applied Dynamic Loads. (to be published)
2. Courant, R. and Friedrichs, K.O. Supersonic Flow and Shock Waves. Interscience Publishers, Inc. New York, New York, 1948.
3. Von Neumann, J. and Richtmyer, R.D. A Method for the Numerical Calculations of Hydrodynamic Shocks. Journal of Applied Physics, Vol. 21, p. 232, 1950.
4. Grandey, R.A. Application of Finite Difference Methods to Problems in Two-Dimensional Hydrodynamics. Aeroneutronics Publication No. U-1130, Jan. 1961.
5. Richtmyer, R.D. Difference Methods for Initial Value Problems. Interscience Tracts in Pure and Applied Mathematics, No. 4, Interscience Publishers, Inc., New York, New York, 1957.
6. Witmer, E.A., Herrmann, W., Leech, J.W., and Pian, T.H.H. Responses of Plates and Shells to Intense External Loads of Short Duration. WADD Technical Report 60-433, April 1960.
7. Walsh, J.M., Rice, M.H., McQueen, R.G., and Yarger, F.L. Shock Wave Compression of Twenty-Seven Metals. Equations of State of Metals. Physical Review, Vol. 108, p. 196, 1957.
8. McQueen, R.G. and Marsh, S.P. Equation of State for Nineteen Metallic Elements from Shock Wave Measurements to Two Megabars. Journal of Applied Physics, Vol. 31, p. 1253, 1960.

9. Altshuler, L.V., Krupnikov, K.K., Ledenev, B.N., Zhuchikhin, V.I., and Brazhnik, M.I. Dynamic Compressibility and Equation of State of Iron under High Pressure. Soviet Physics JETP, Vol. 34, p. 606, 1958.
10. Altshuler, L.V., Kormer, S.B., Bakanova, A.A., and Trunin, R.F. Equation of State of Aluminum, Copper, and Lead in the High Pressure Region. Soviet Physics JETP, Vol. 11, p. 573, 1960.
11. Bridgman, P.W. Linear Compression to 30,000 Kg/cm² Including Relatively Incompressible Substances. Proceedings of the American Academy of Arts and Sciences, Vol. 77, p. 187, 1948.
12. Slater, J.C. Introduction to Chemical Physics. McGraw-Hill Book Co., Inc. New York, New York, 1939.
13. Dugdale, J.S. and MacDonald, D.K.C. The Thermal Expression of Solids. Physical Review, Vol. 89, p. 832, 1953.
14. Gilvarry, J.J. Gruneisen Parameter for a Solid under Finite Strain. Physical Review, Vol. 102, p. 331, 1956.
15. Wood, D.S. On Longitudinal Plane Waves of Elastic-Plastic Strain in Solids. Journal of Applied Mechanics, Vol. 19, p. 521, 1952.
16. Morland, L.W. The Propagation of Plane Irrotational Waves through an Elastoplastic Medium. Philosophical Transactions of the Royal Society of London, Series A, Vol. 251, p. 341, 1959.
17. Fowles, G.R. Shock Wave Compression of Hardened and Annealed 2024 Aluminum. Stanford Research Institute, TR 011-60, 1960.

18. Lundergan,C.D. The Hugoniot Equation of State of 6061-T6 Aluminum at Low Pressures. Sandia Corporation SC-4637(RR) 1961.

19. Backman,M.E. Plasticity and Non-Linear Elastic Strains. NAVWEPS 7648, April 1961.

20. Birch,F. The Effect of Pressure upon the Elastic Parameters of Isotropic Solids, According to Murnaghan's Theory of Finite Strains. Journal of Applied Physics, Vol.9, p.279, 1938.

21. Rowles,G.R. Attenuation of the Shock Wave Produced in a Solid by a Flying Plate. Journal of Applied Physics, Vol.31, p.655, 1960.

22. Lundergan,C.D., Smith,J., and Barker,L. Technical Status Report: First Meeting of the Working Committee on AFSWC Theoretical and Experimental Fracture Program. 22,23 March 1960.

23. Malvern,L.E. Plastic Wave Propagation in a Bar of Material Exhibiting a Strain Rate Effect. Quarterly for Applied Mathematics, Vol.8, p.405, 1951.

24. Rubin,R.J. Propagation of Longitudinal Deformation Waves in a Prestressed Rod of Material Exhibiting a Strain Rate Effect. Journal of Applied Physics, Vol.25, p.528, 1953.

25. Zhurkov,S.N. and Sanfirova,T.P. Relation Between Strength and Creep of Metals and Alloys. Soviet Physics; Technical Physics (Translation) Vol.3, p.1586 (1958).

26. Hsiao,C.C. Time-Dependent Tensile Strength of Solids. Nature, Vol.186, p.535 (1960).

27. Beuche,F. Tensile Strength of Plastics below the Glass Temperature. Journal of Applied Physics, Vol.28, p.784 (1957).
28. Dorn,J.E. Some Fundamental Experiments on High Temperature Creep. Journal of the Mechanics and Physics of Solids, Vol.3, p.85, 1954.
29. Anderson,W.H. Kinetics and Mechanism of Fracture in Solid Materials. Technical Status Report Presented at the First Meeting of the Working Committee on Fracture, 22-23 March 1961.
30. Waldorf,W.F.Jr. Interim Report - A High Temperature Theory of Crack Propagation. Republic Aviation Corporation Report No.MSD 276-952(203), Dec.1960.
31. Valluri,S.R. and Williams,M.L. A Criteria for the Upper Limiting Value of Fracture Stress under Conditions of Impact Loading for Semi-brittle and Brittle Materials. California Institute of Technology, GALCIT SM60-2, January 1960.
32. Keller,D.V. and Young,D.M. A Method for Determining Spallation Criteria in Solids. Air Force Special Weapons Centre, Technical Documentary Report No. AFSWC-TDR-61-102, November 1961.
33. Evans,C. and Evans,F. Shock Compression of a Perfect Gas. Journal of Fluid Mechanics, Vol.1, p.399, 1956.
34. Winter,D.F.T. Multiple Shock Compression Using a Piston of Finite Weight. Journal of Fluid Mechanics, Vol.5, p.264, 1960.
35. Feldman,S. Hypersonic Gas Dynamic Charts for Equilibrium Air. AVCO Research Laboratory, Research Report 40, January 1957.

36. Stollery, J.L. and Maul, D.J. A Note on the Compression of Air Through Repeated Shock Waves. Journal of Fluid Mechanics, Vo.4, 1958.
37. Hilsenrath, J. and Beckett, C.W. Tables of Thermo-dynamic Properties of Argon-Free Air to 15,000°K. AEDC-TN-56-12, ASTIA AD-98974.
38. Hilsenrath, J., Green, M.S., and Beckett, C.W. Thermo-dynamic Properties of Highly Ionized Air. AFSWC-TR-56-35, ASTIA AD-96303.
39. Ryabinin, Yu.N. Effect of Pressure on Some Properties of Solids. Soviet Physics Technical Physics, Vol.5, p.693, 1960.
40. Borelius, G. Changes of State of Simple Solid and Liquid Metals. Solid State Physics, Advances in Research and Applications, Vol.VI, p.65. Academic Press, New York, New York, 1958.
41. McQueen, R.G. and Marsh, S.P. Ultimate Yield Strength of Copper. Journal of Applied Physics, Vol.33, p.654, 1962.

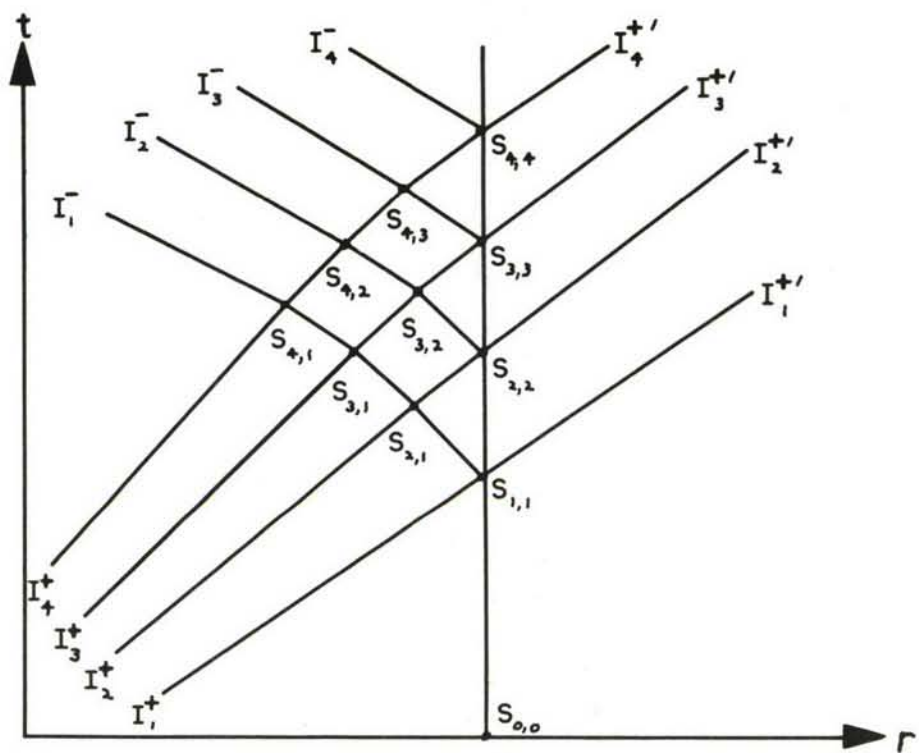


Fig. 3.1 Characteristic Net for Reflection at an Interface

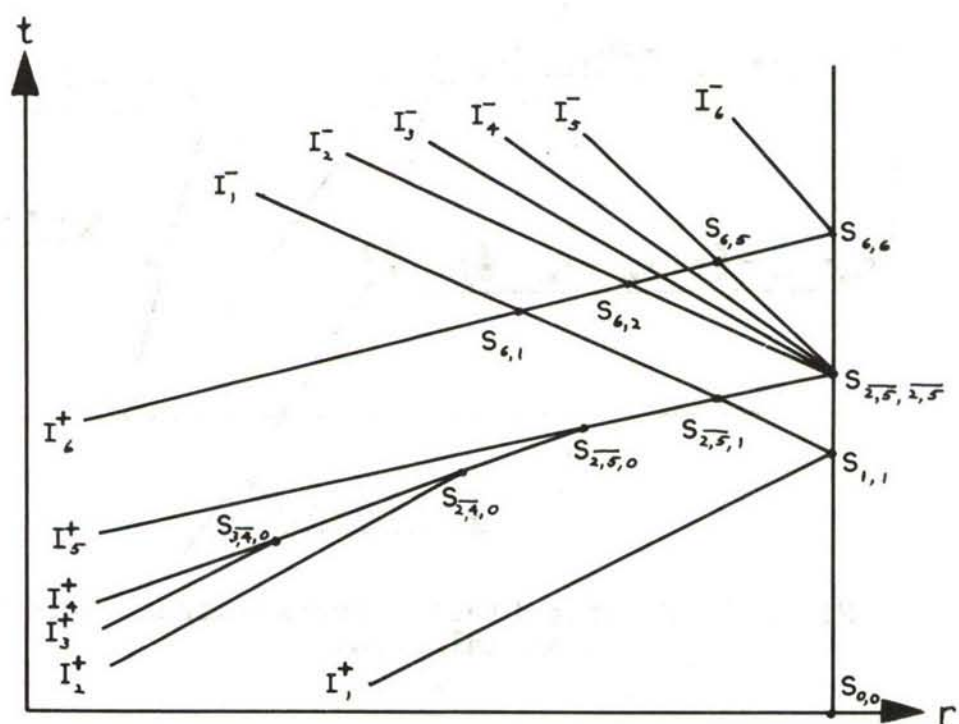


Fig. 3.2 Characteristic Net for Formation and Reflection of a Weak Shock

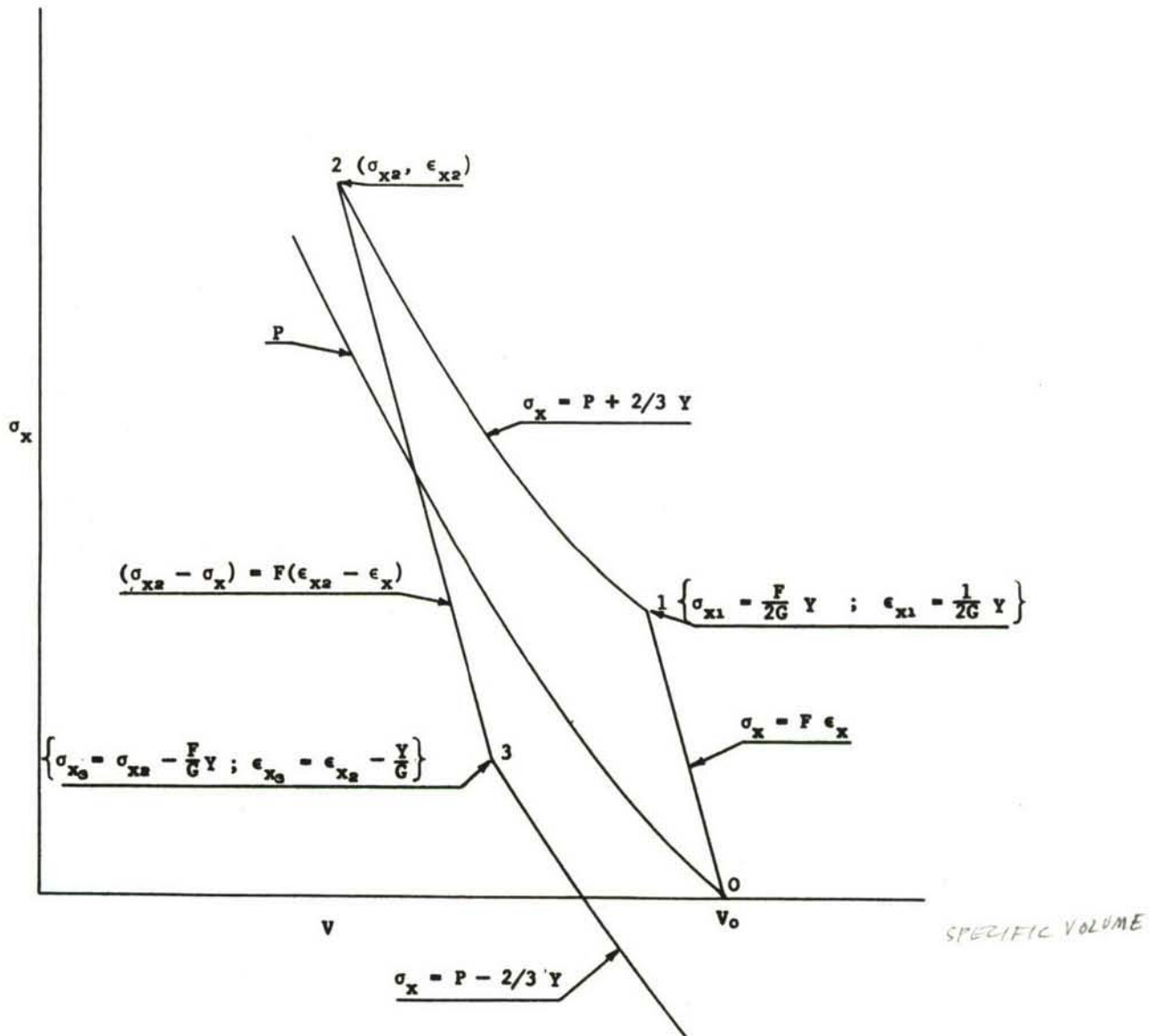


Fig.4.1 Elastic-Plastic Stress-Strain Schematic for Uniaxial Strain

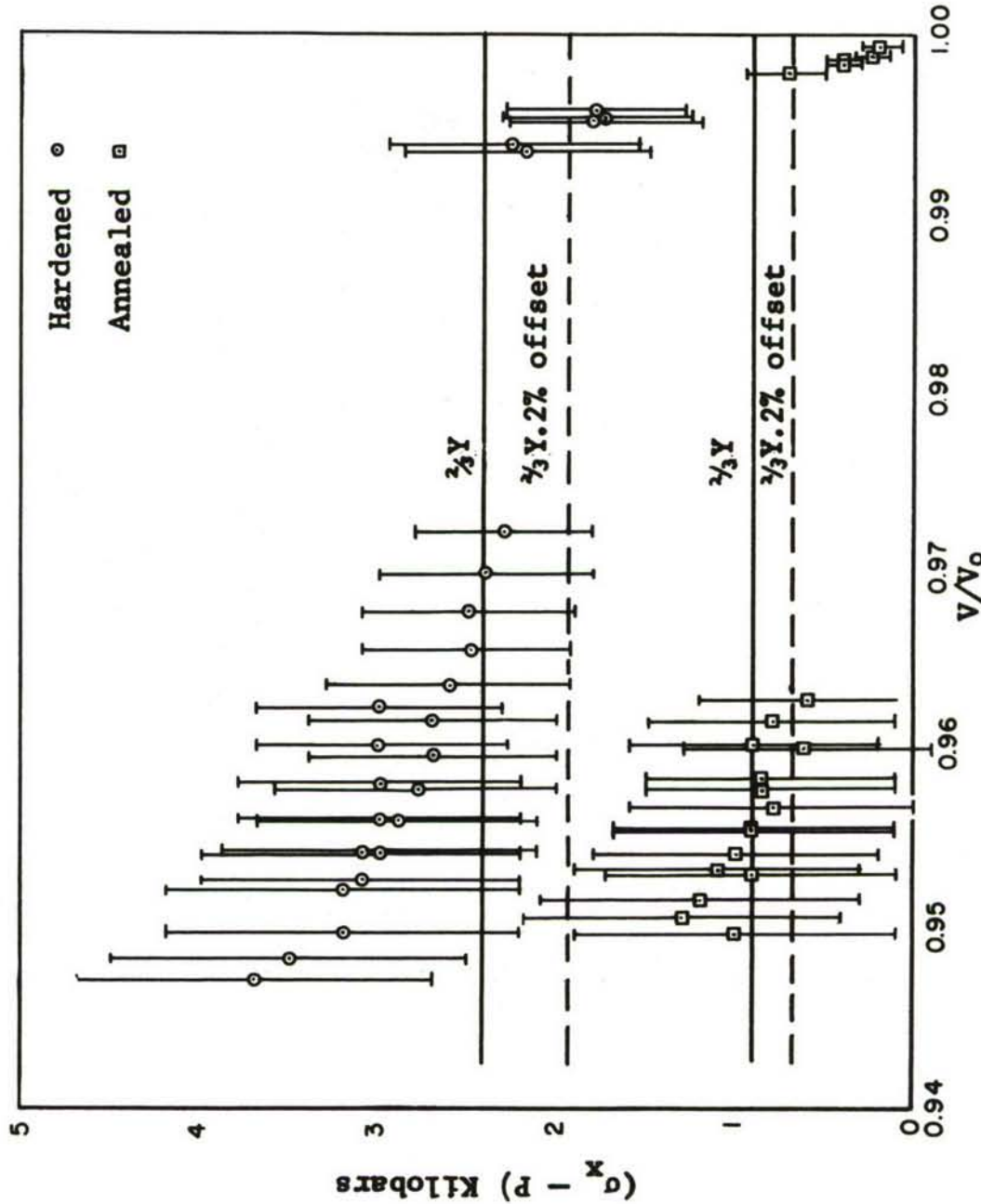


Fig.4.2a Offset of the Hugoniot from the Adiabat in Pure Dilatation for 2024 Aluminum (data from Fowles¹⁷)

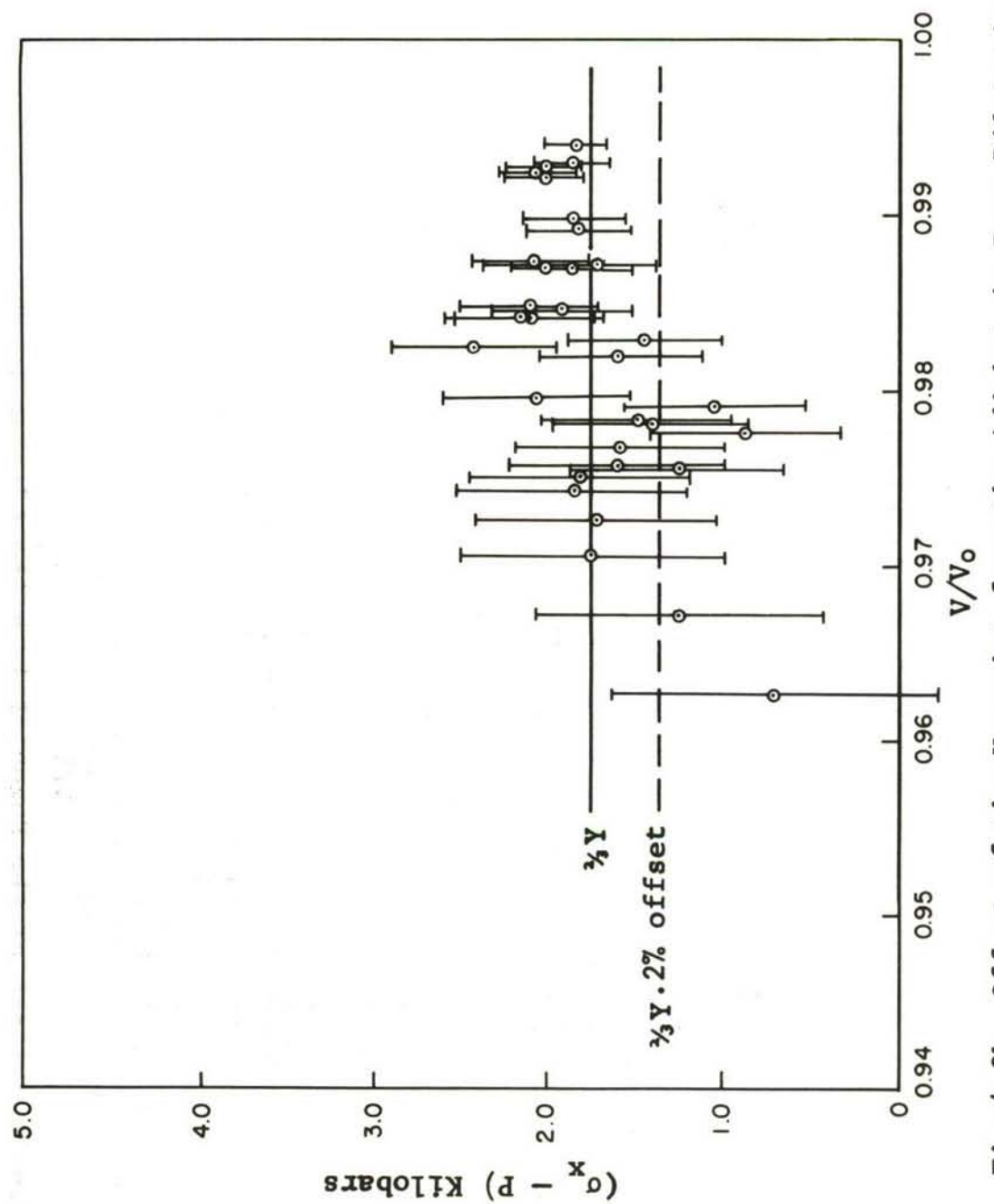


Fig.4.2b Offset of the Hugoniot from the Adiabat in Pure Dilatation for 6061-T6 Aluminum (data from Lundergan¹⁸)

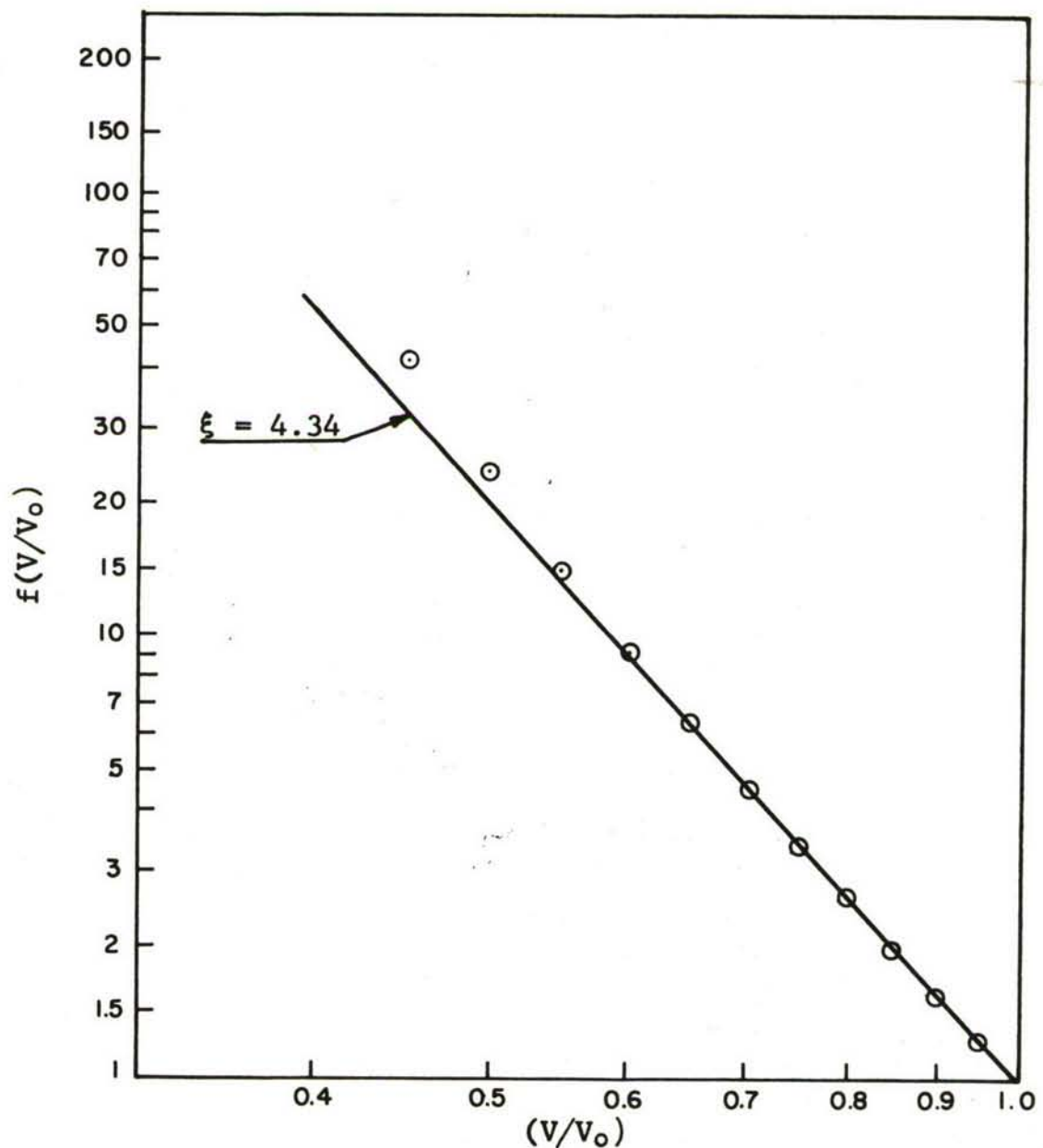


Fig.4.3 Murnaghan Fit to the Dynamic Adiabat for Aluminum

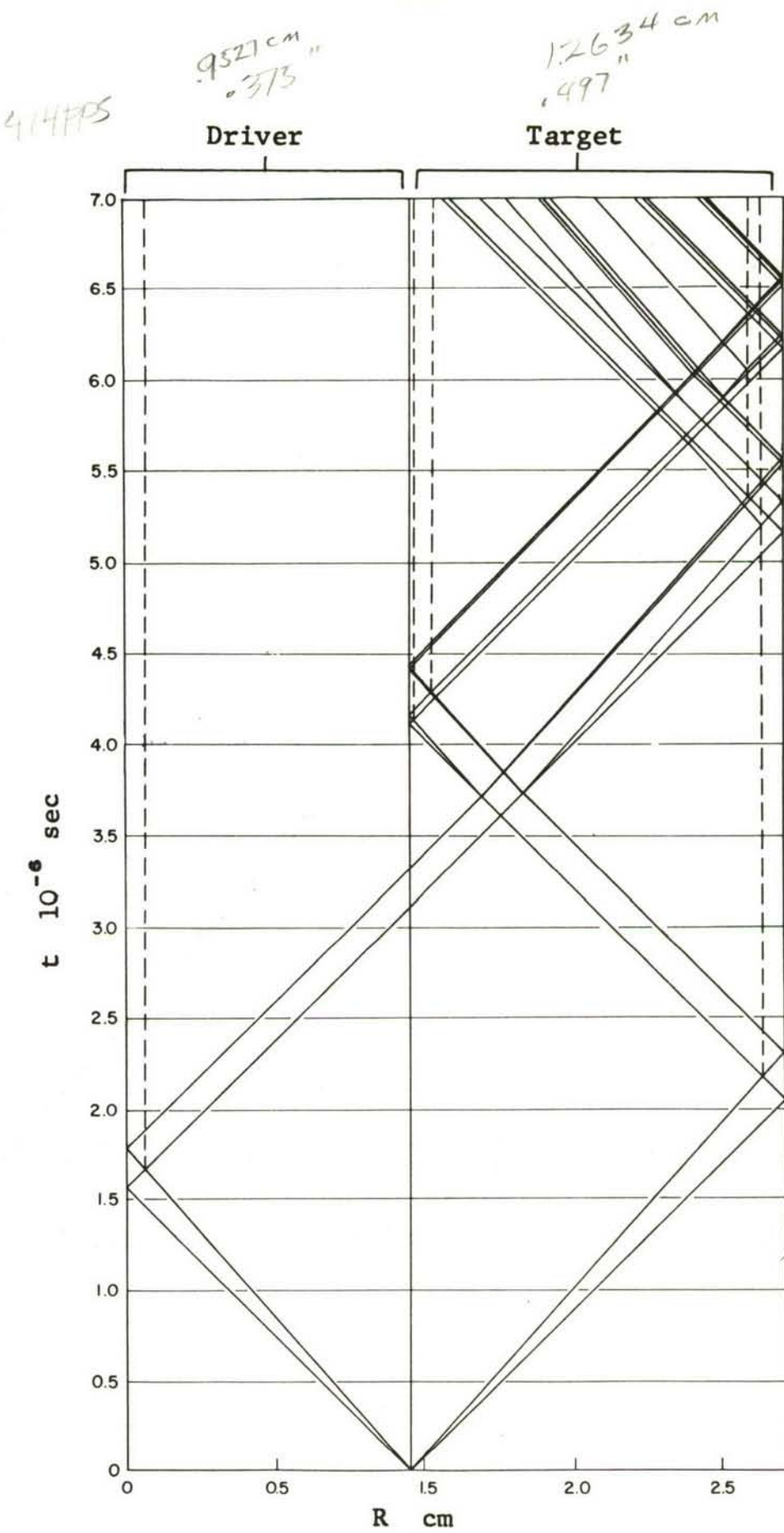
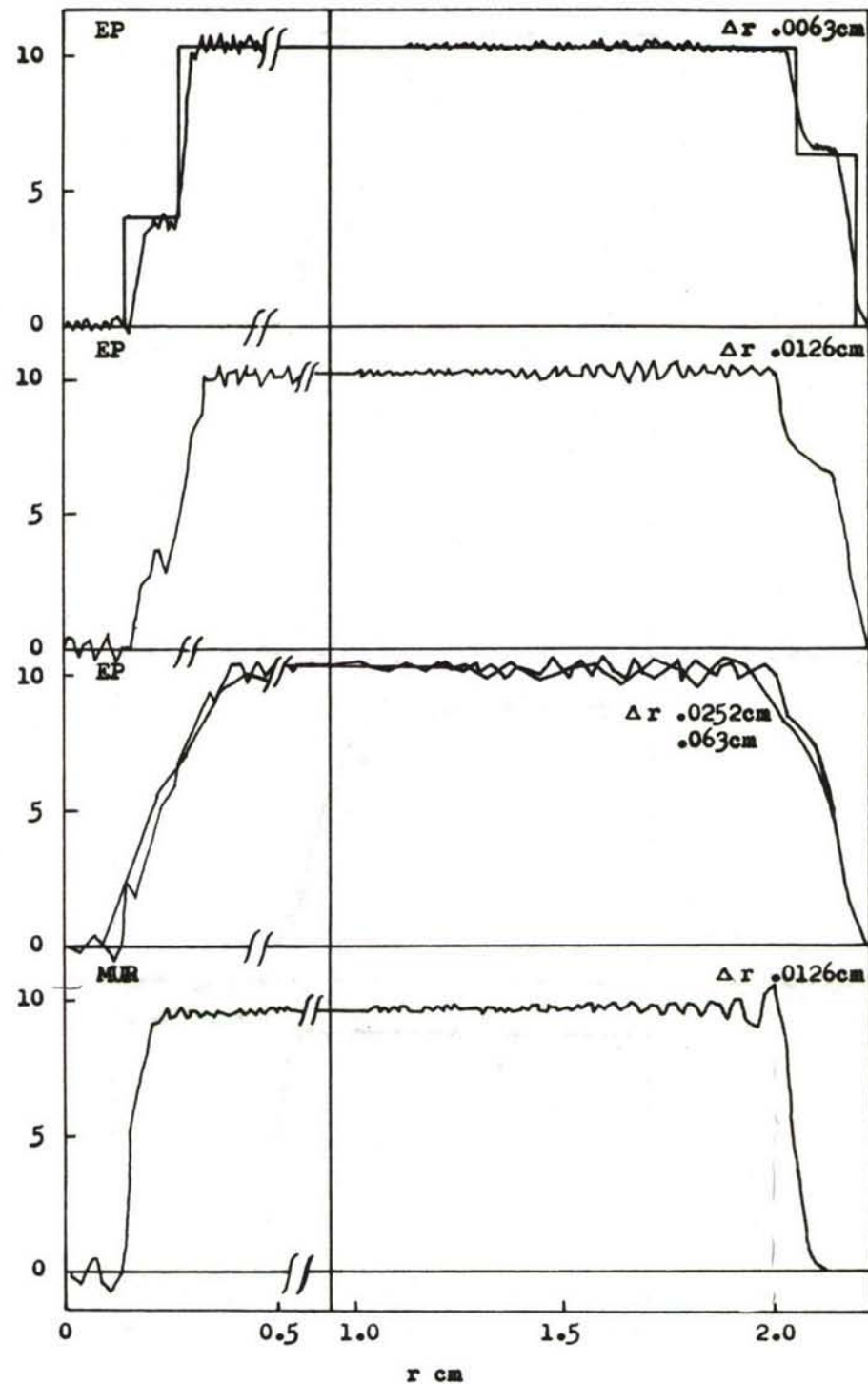


Fig.5.1 Lagrangian Characteristic Mesh for Plate Impact
ASD-TDR-62-399 90



$$V_s = \frac{2.1 \text{ cm.}}{2452 \times 2.54 \times 2} \approx 34000 \text{ FPS}$$

Fig. 5.2a. Wave Profiles at 2 μ sec After Impact. Copper Driver and Target Plates with an Impact Velocity of 12.6×10^3 cm/sec (414 FPS)

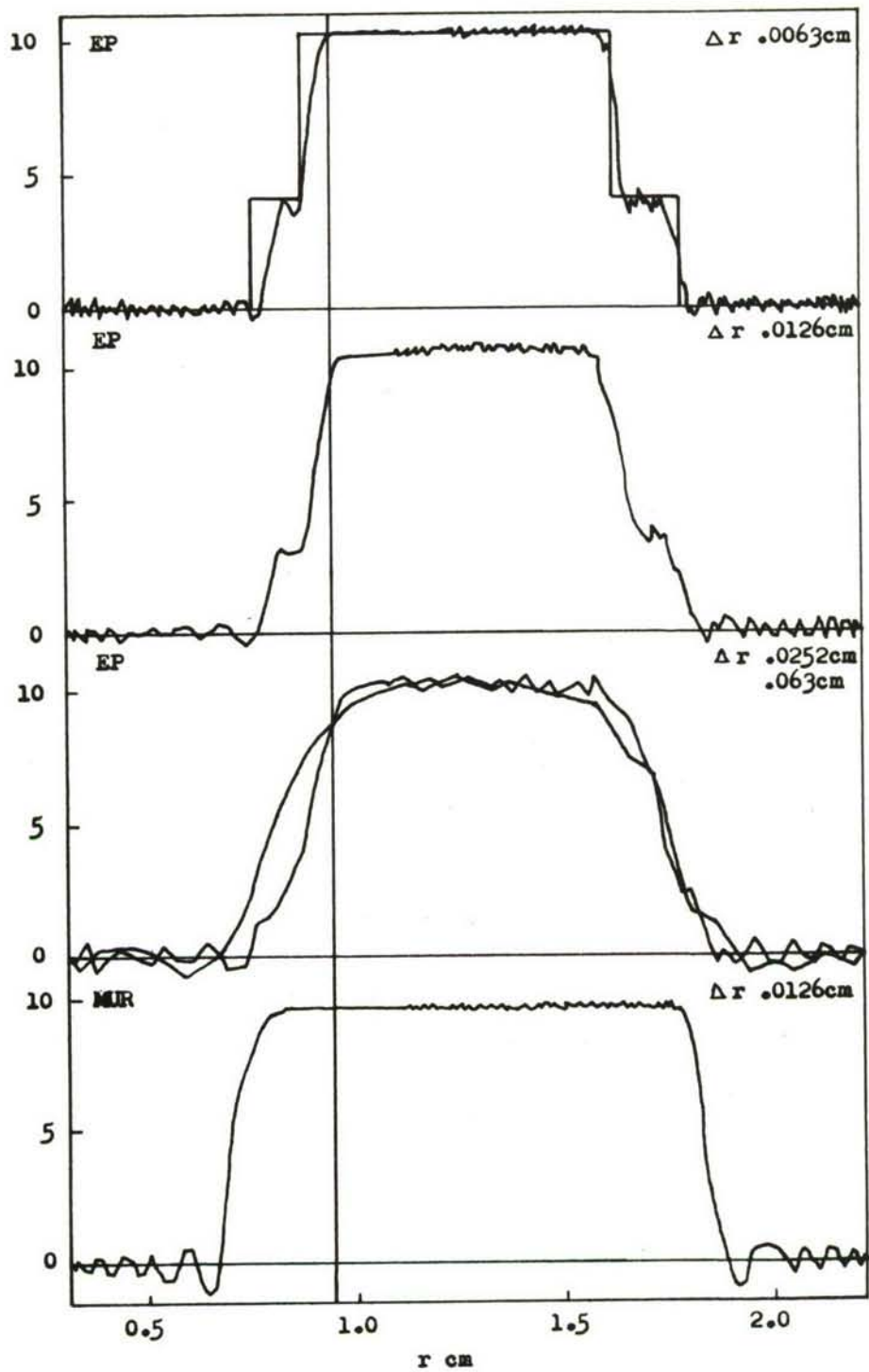


Fig. 5.2b. Wave Profiles Continued. At 3 μ sec After Impact

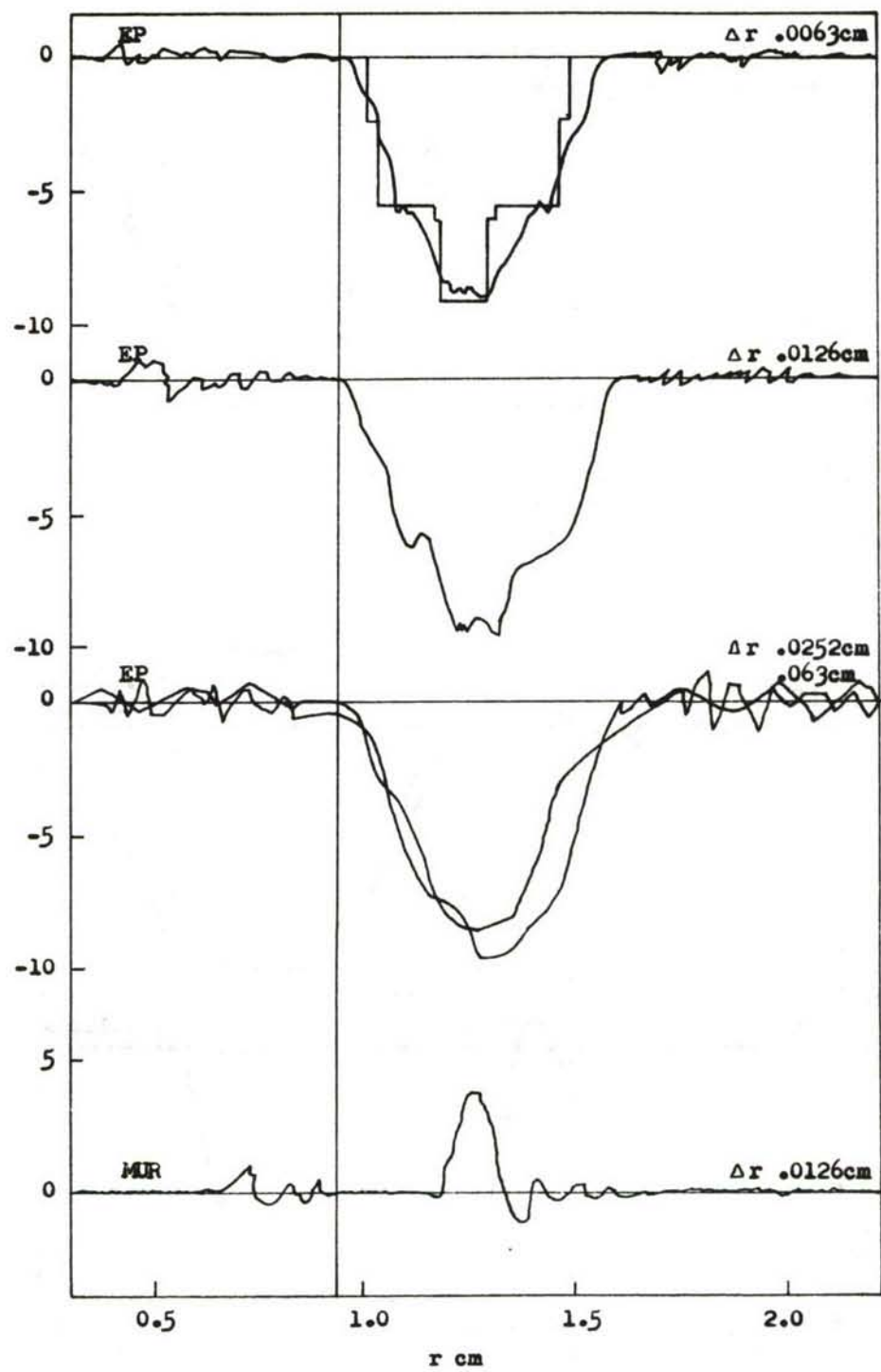


Fig.5.2c. Wave Profiles Continued. At 4 μ sec After Impact

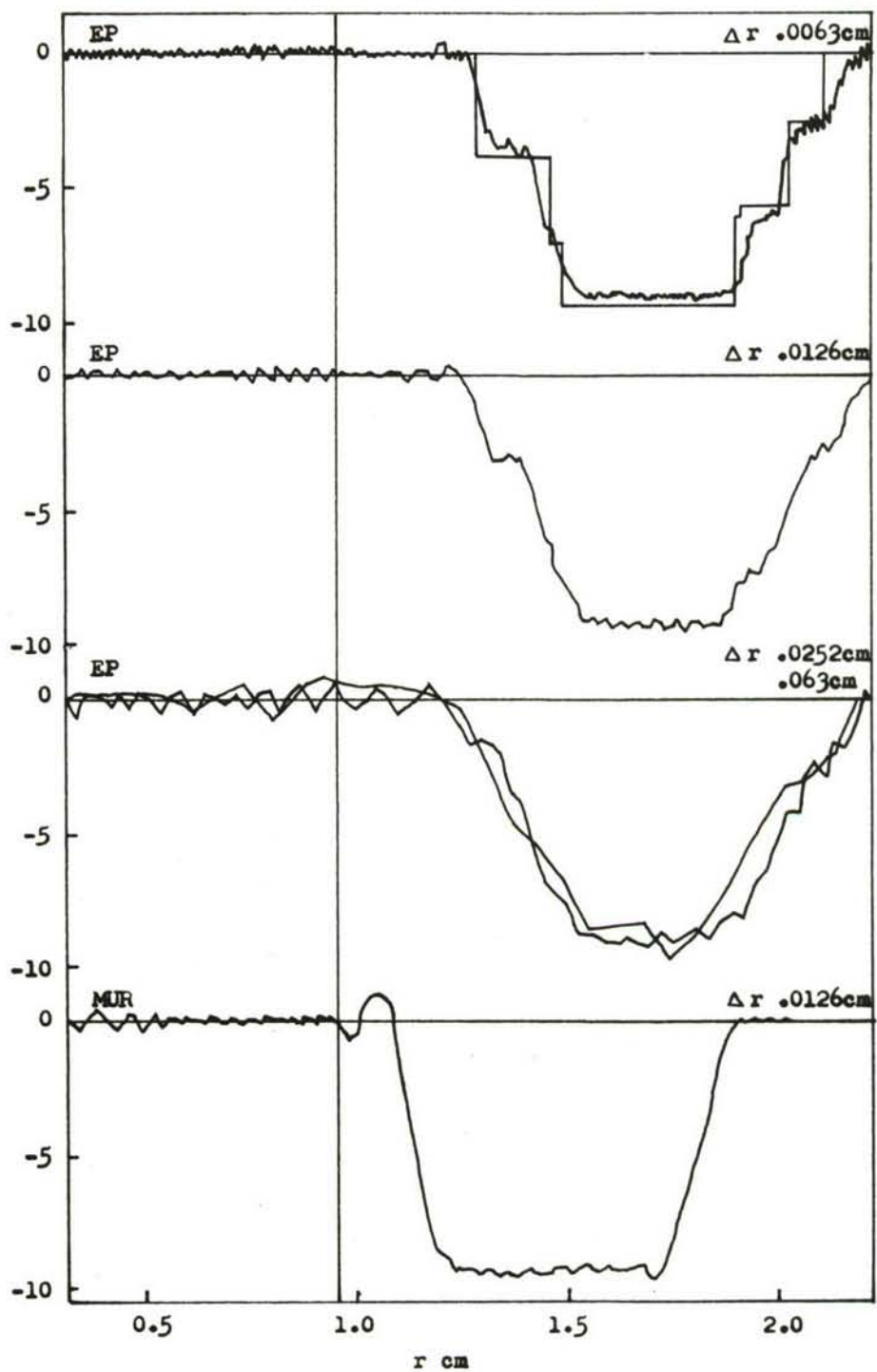


Fig.5.2d. Wave Profiles Continued. At 5 μ sec After Impact

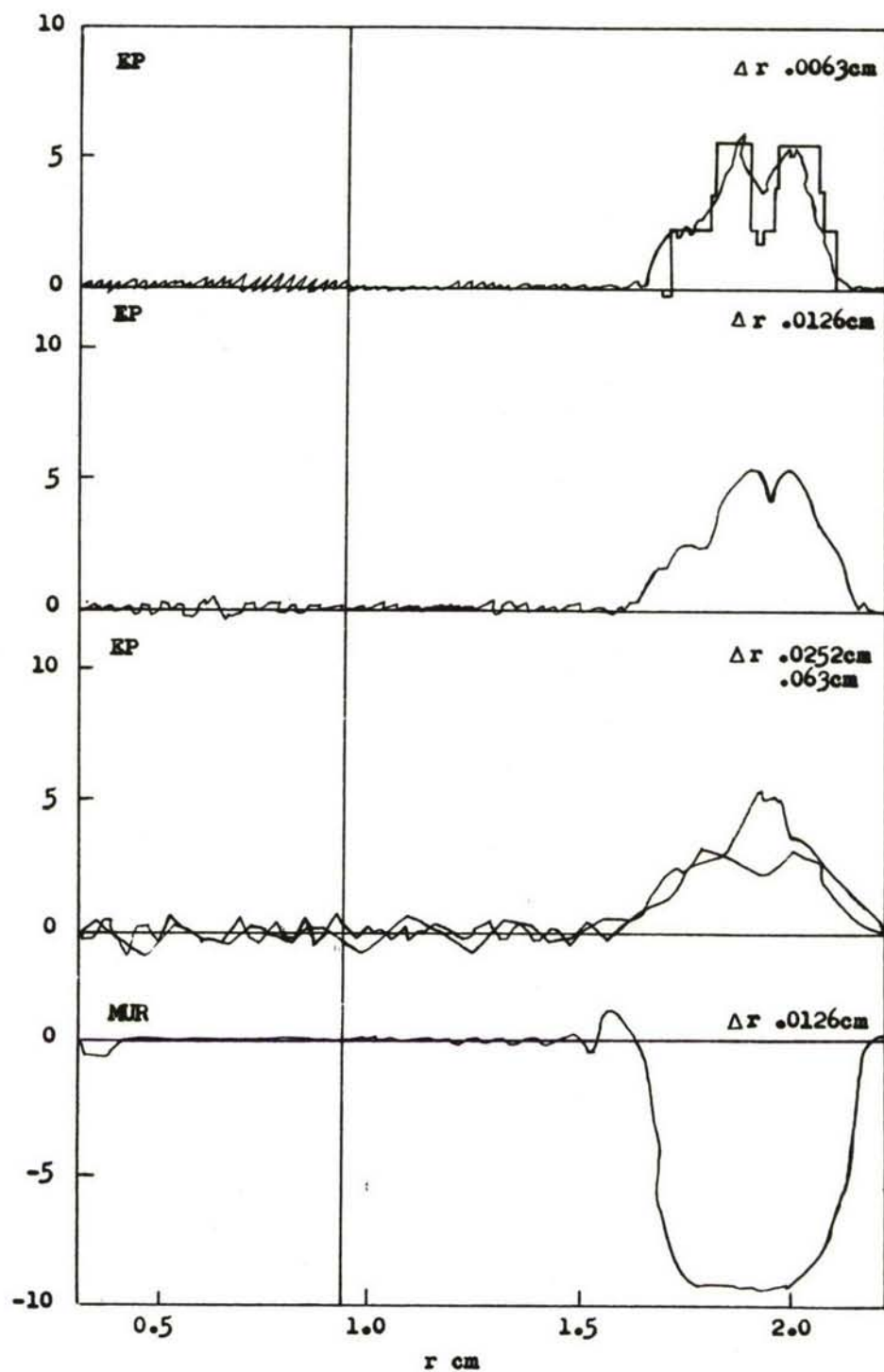


Fig.5.2e. Wave Profiles Continued. At $6 \mu\text{sec}$ After Impact

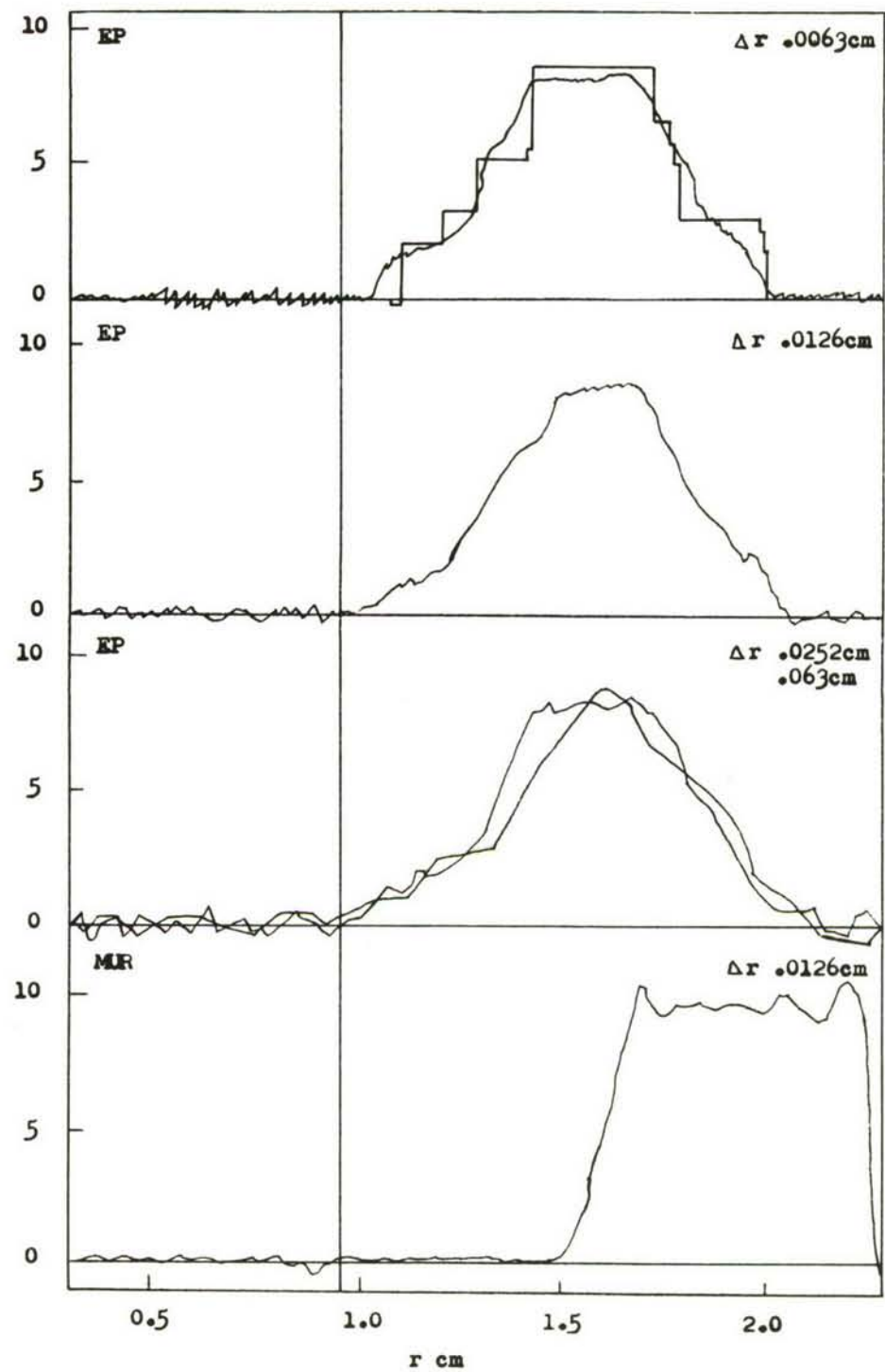


Fig. 5.2f. Wave Profiles Concluded. At 7 μsec After Impact

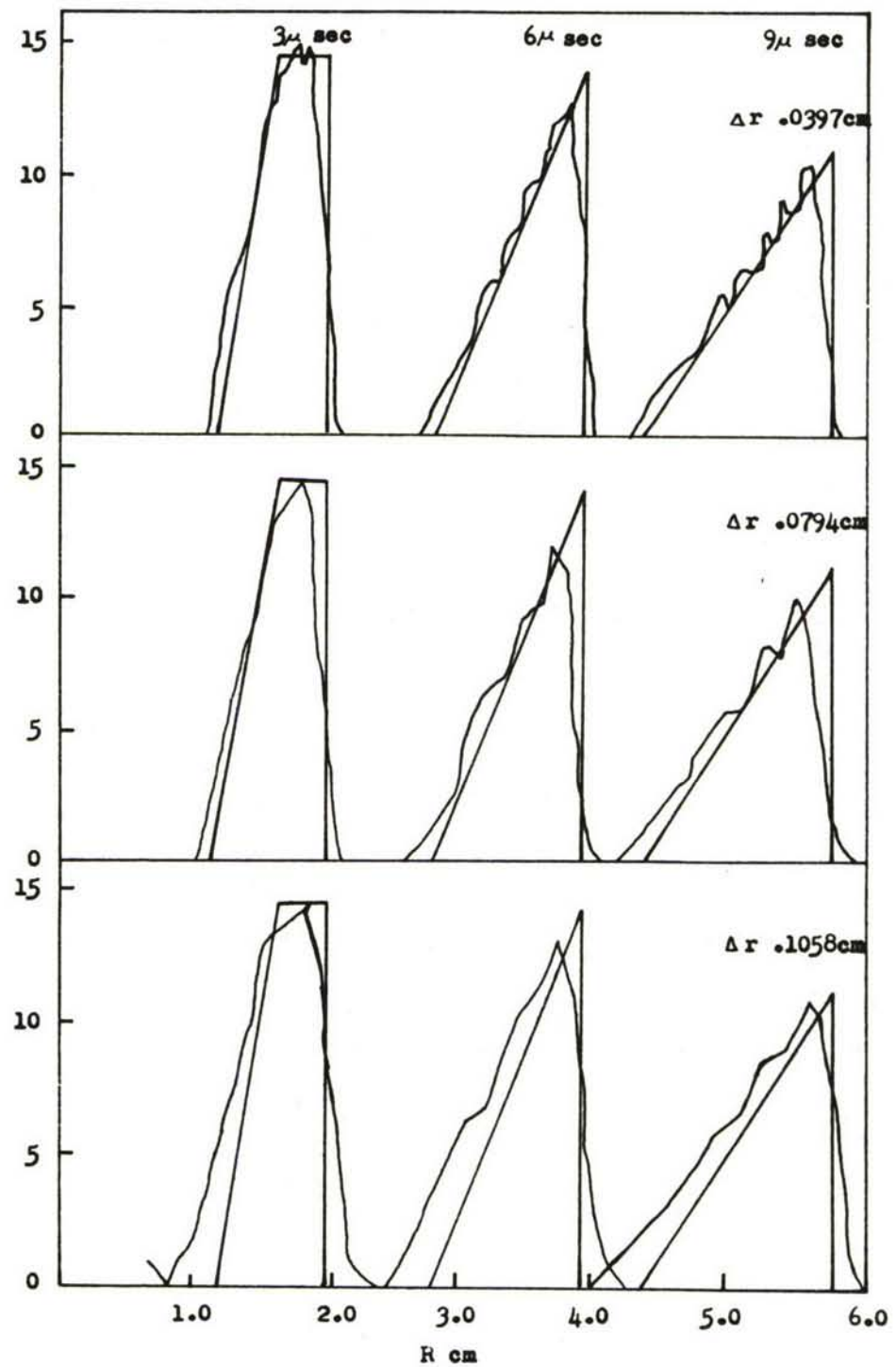


Fig.5.3a. Comparison of Characteristic and Finite Difference Methods for Plate Impact Using the Murnaghan Equation

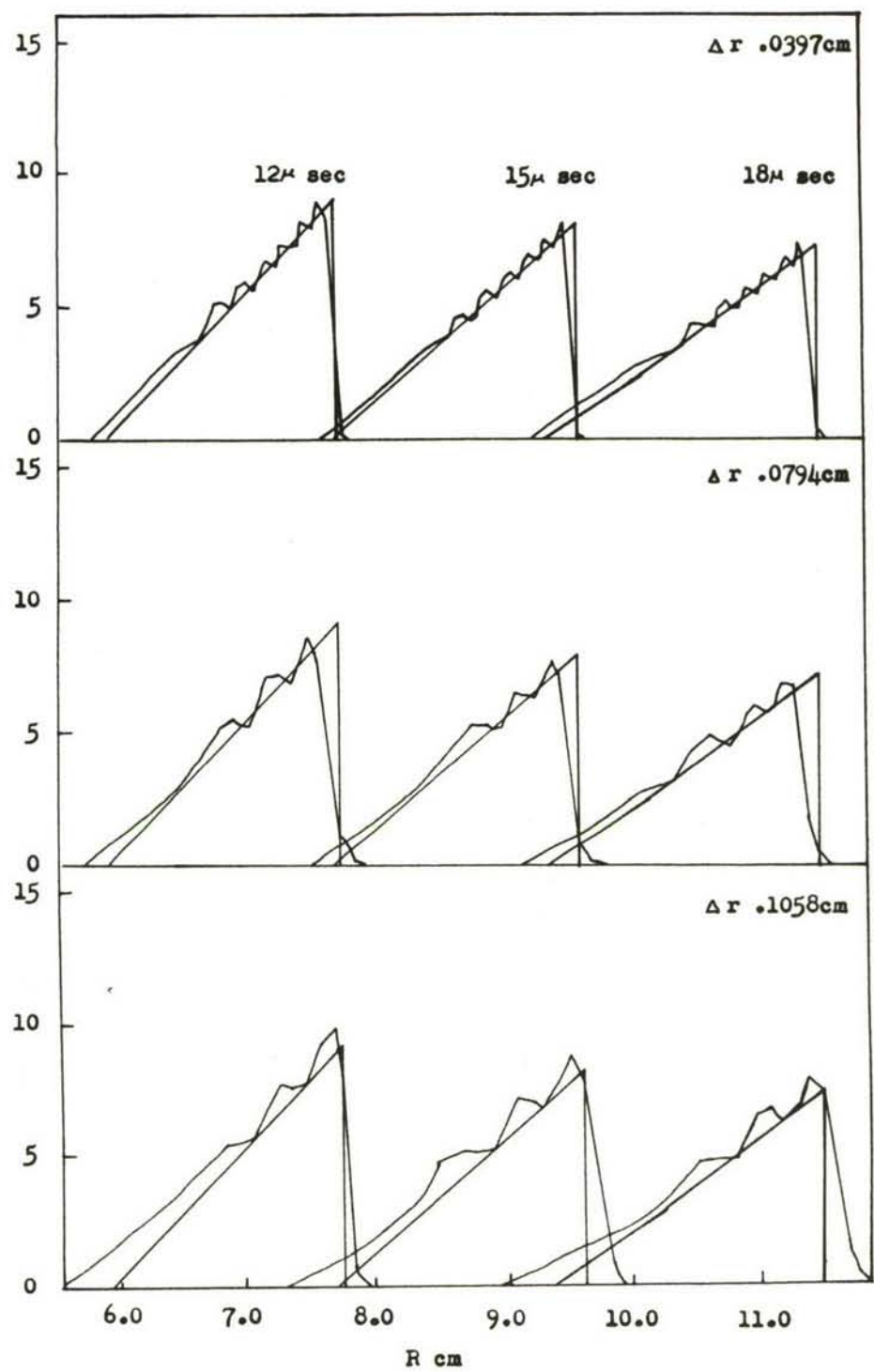
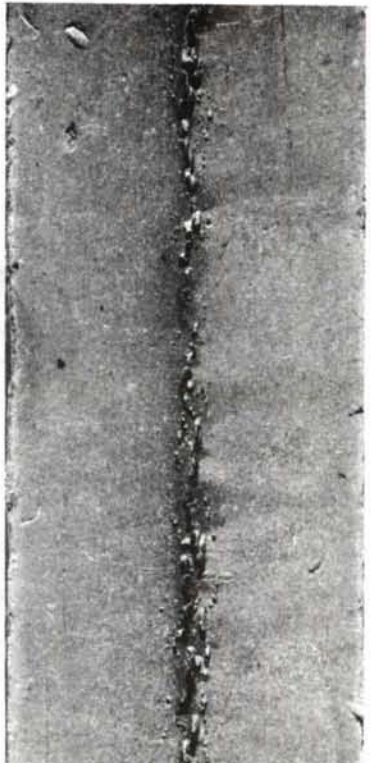


Fig.5.3b. Concluded



0.896×10^4 cm/sec



1.222×10^4 cm/sec



0.521×10^4 cm/sec



0.994×10^4 cm/sec

Fig. 6.1 Sections Through 1/4-inch-thick E.T.P Half-Hard Copper Target Plates Struck by 1/8-inch-thick Driver Plates of the Same Material. Ferric Chloride Etch

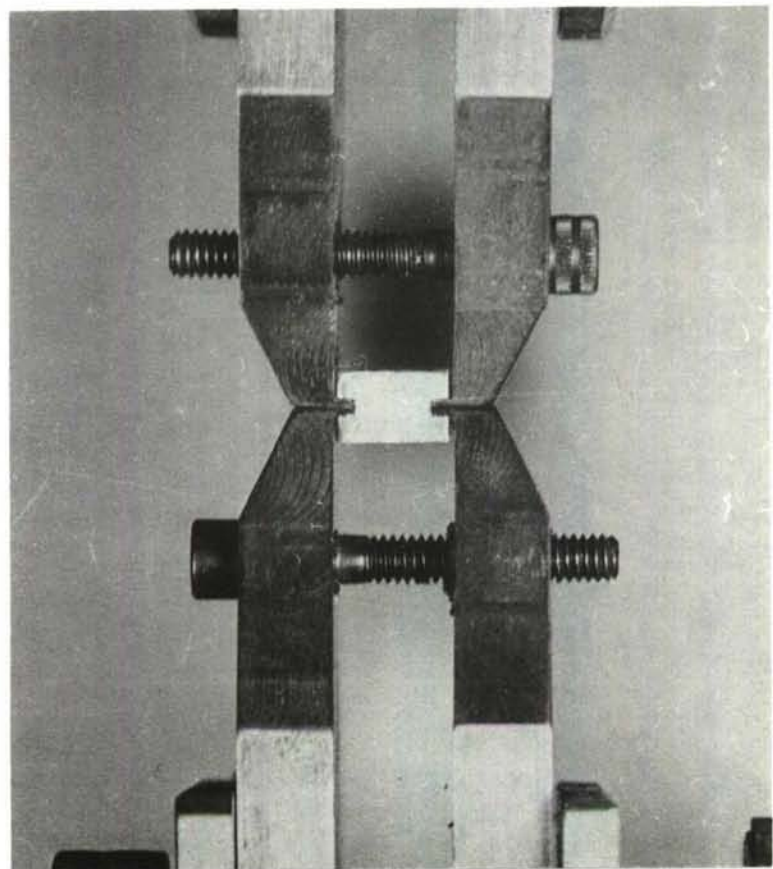


Fig.6.2 Tension Test Arrangement

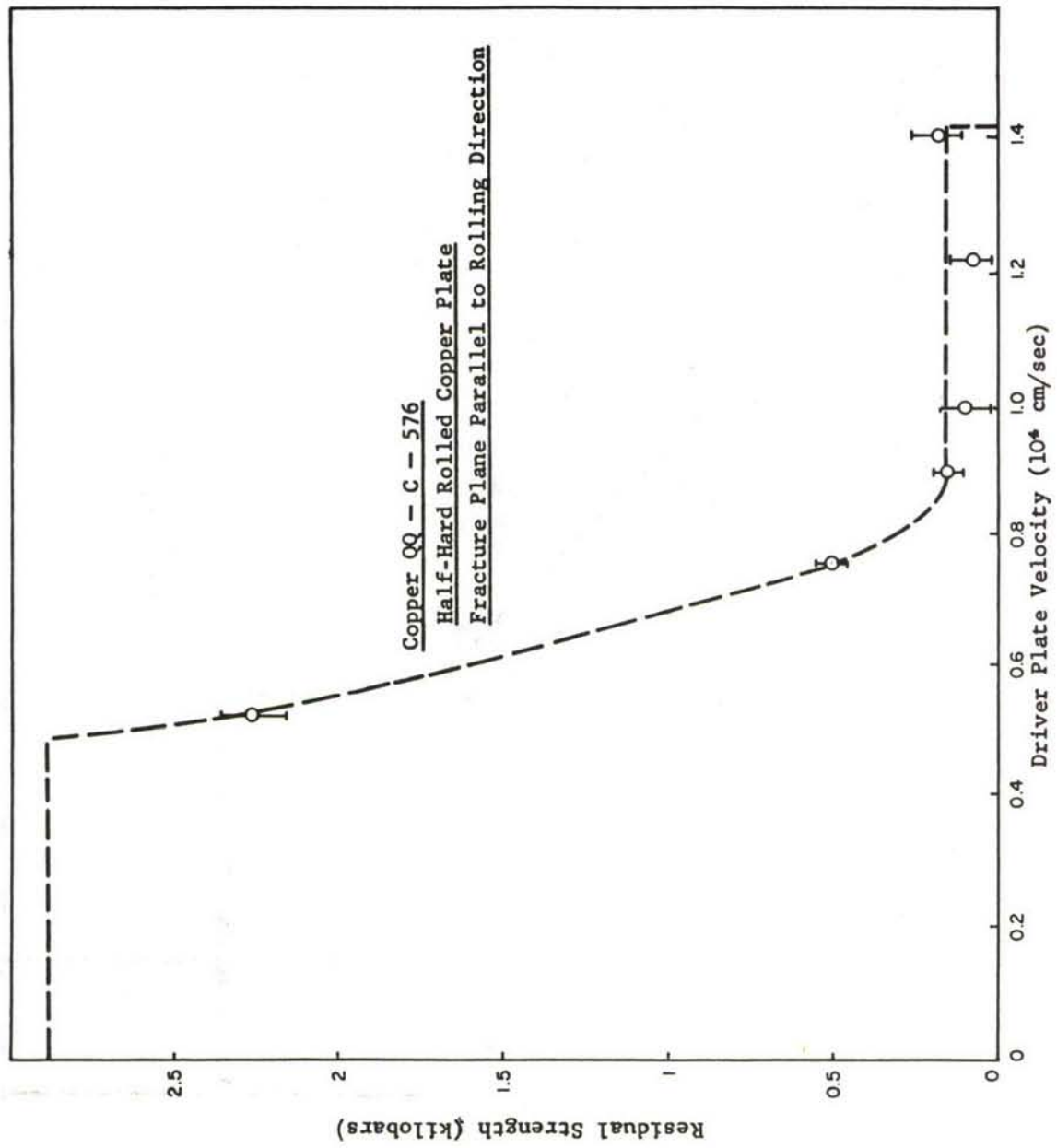


Fig.6.3 Residual Strength of Spalled Targets

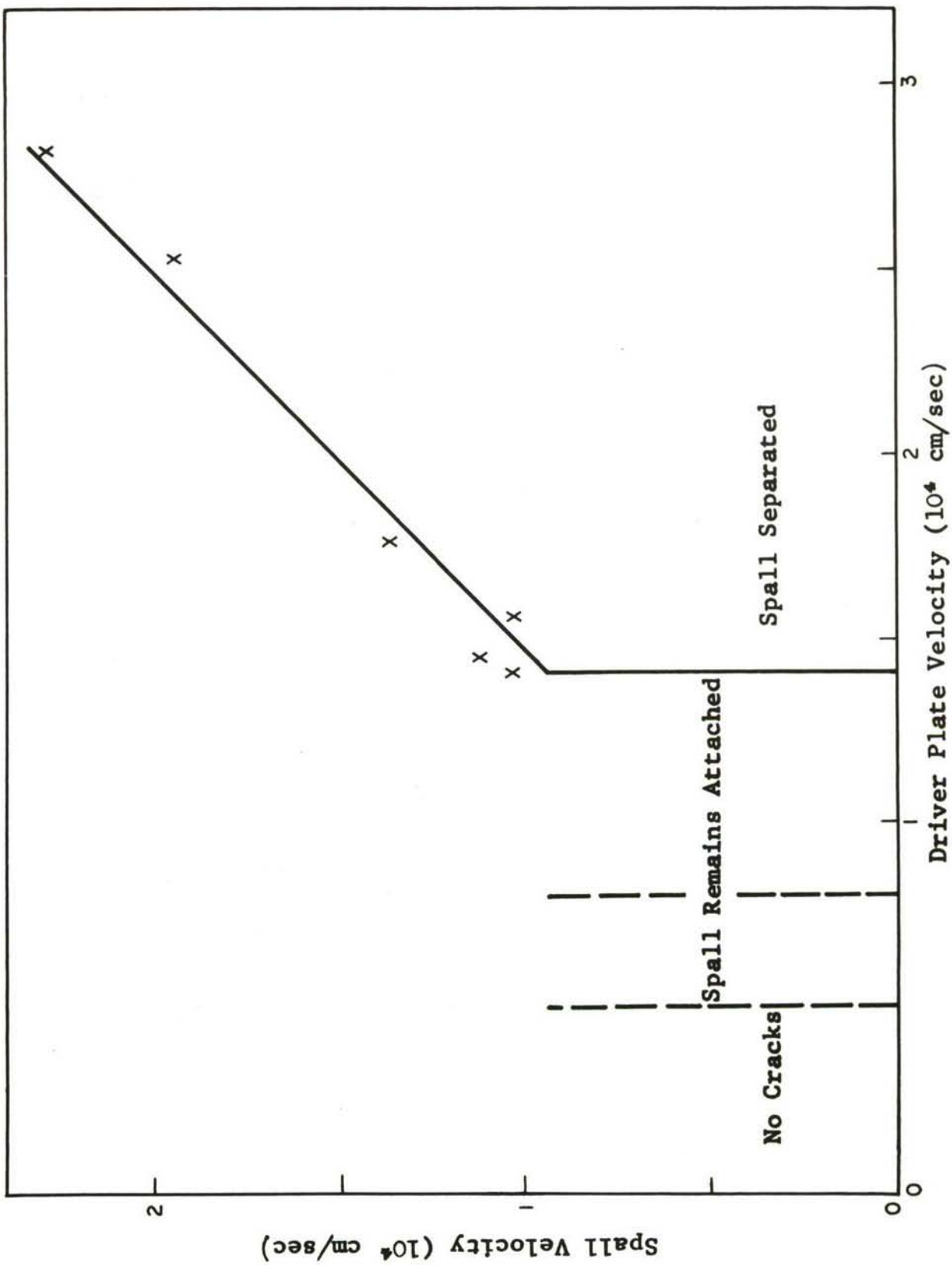


Fig. 6.4 Spall Velocity as a Function of Driver Plate Velocity

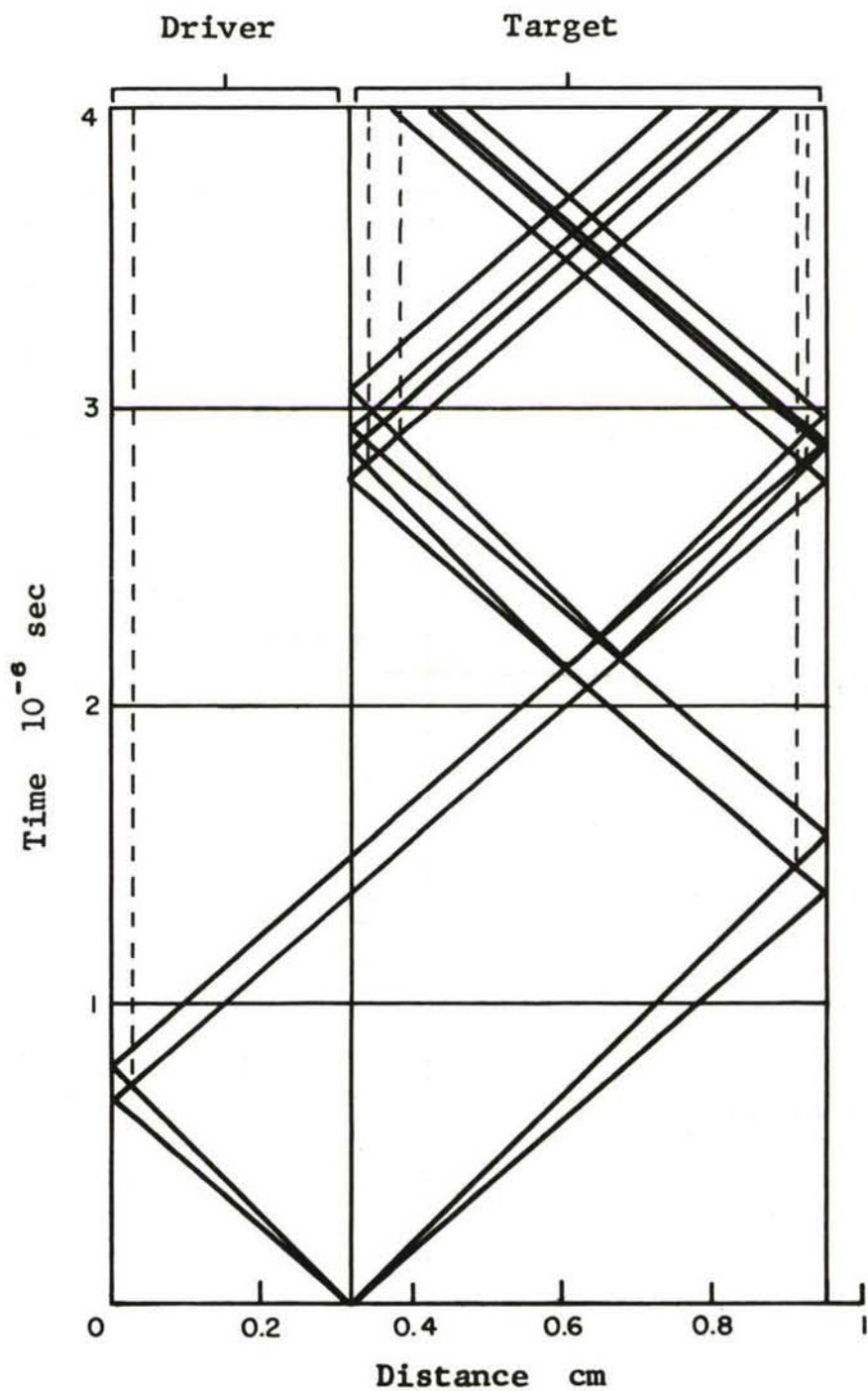


Fig. 6.5 Characteristic Mesh for the Elastic-Plastic Wave System in the Sandia Plate Experiments

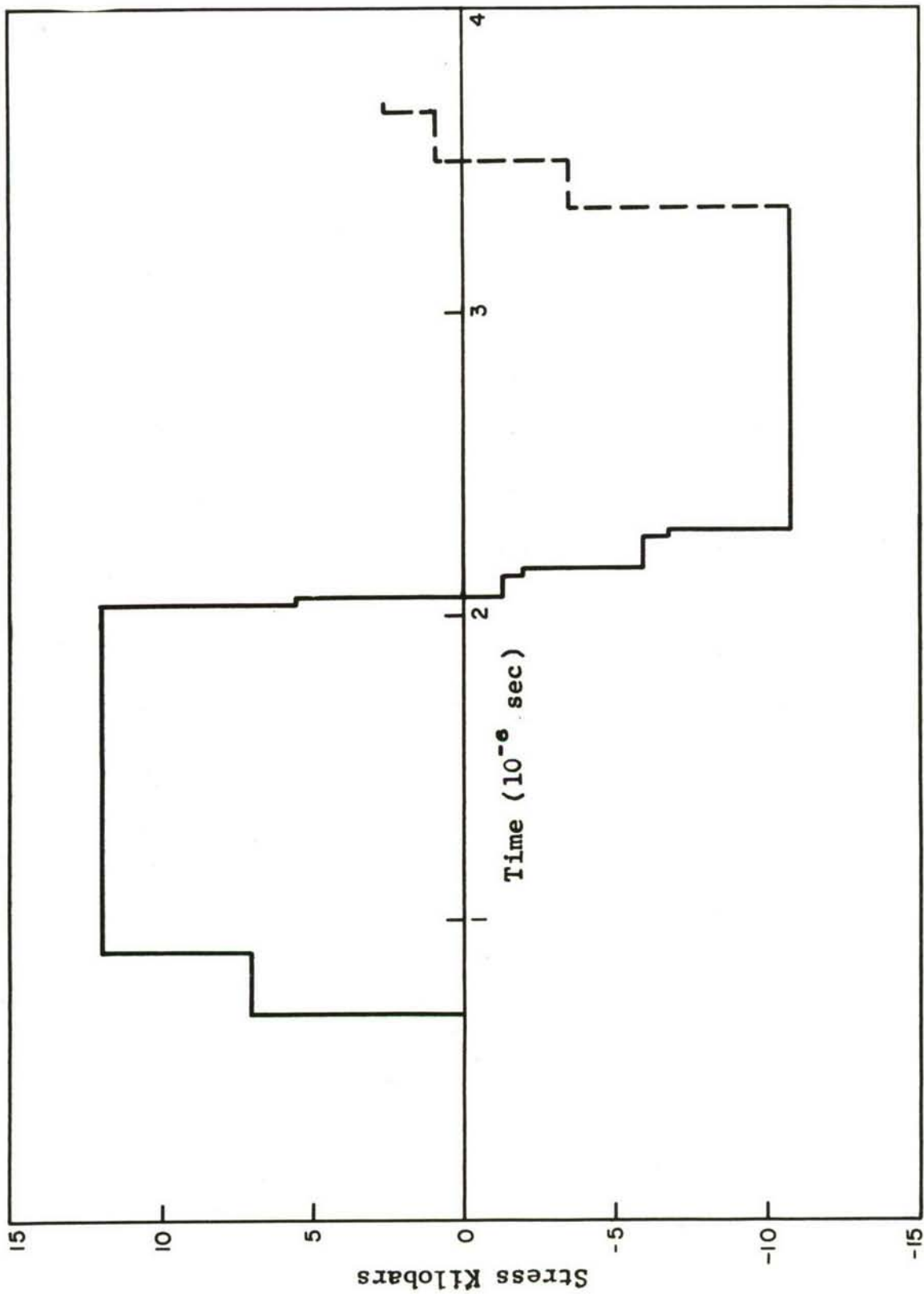


Fig.6.6a Stress-Time History at a Station at the Target Centre

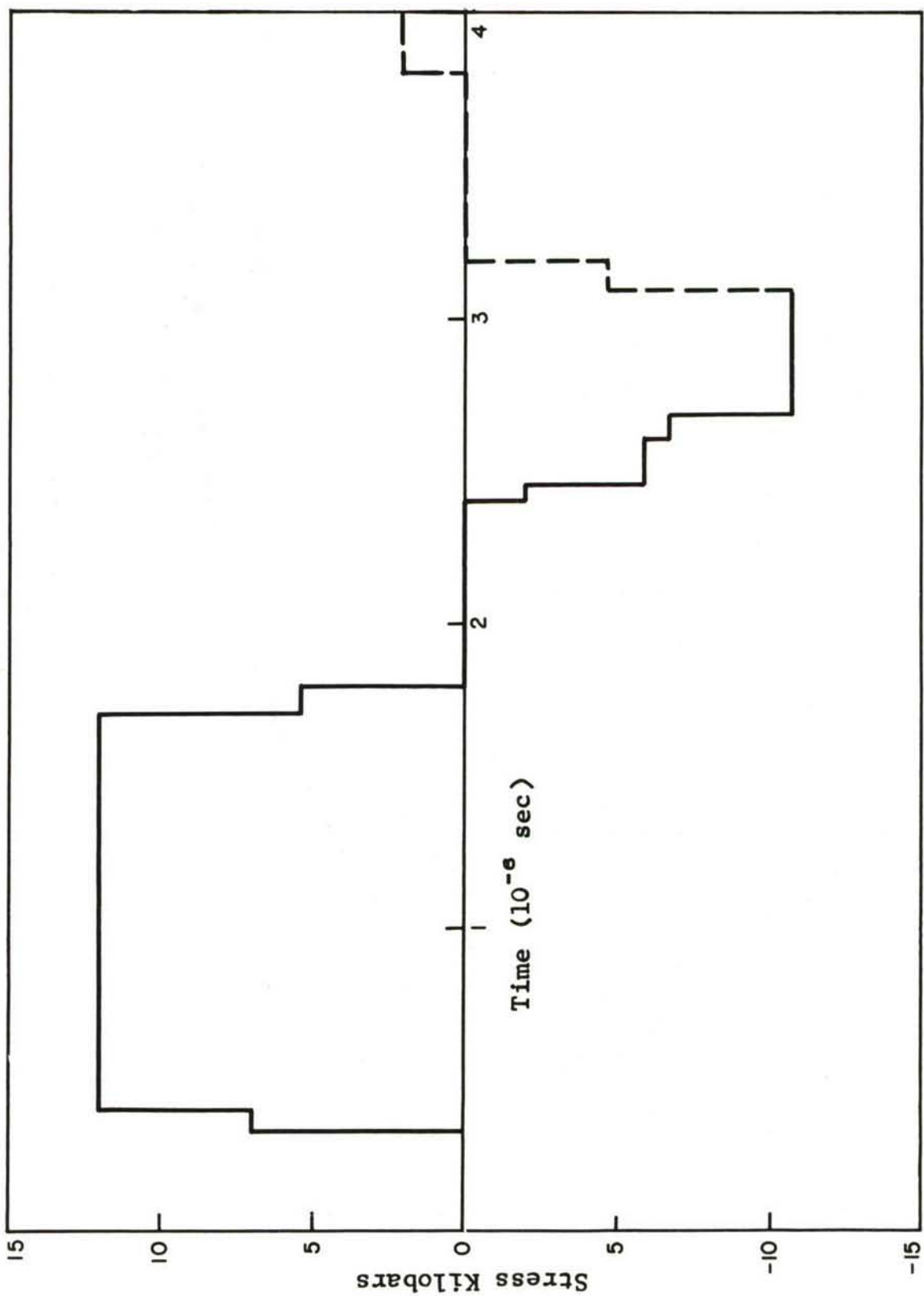


Fig. 6.6b Stress-Time History at a Station One Quarter of the Target Thickness from the Interface

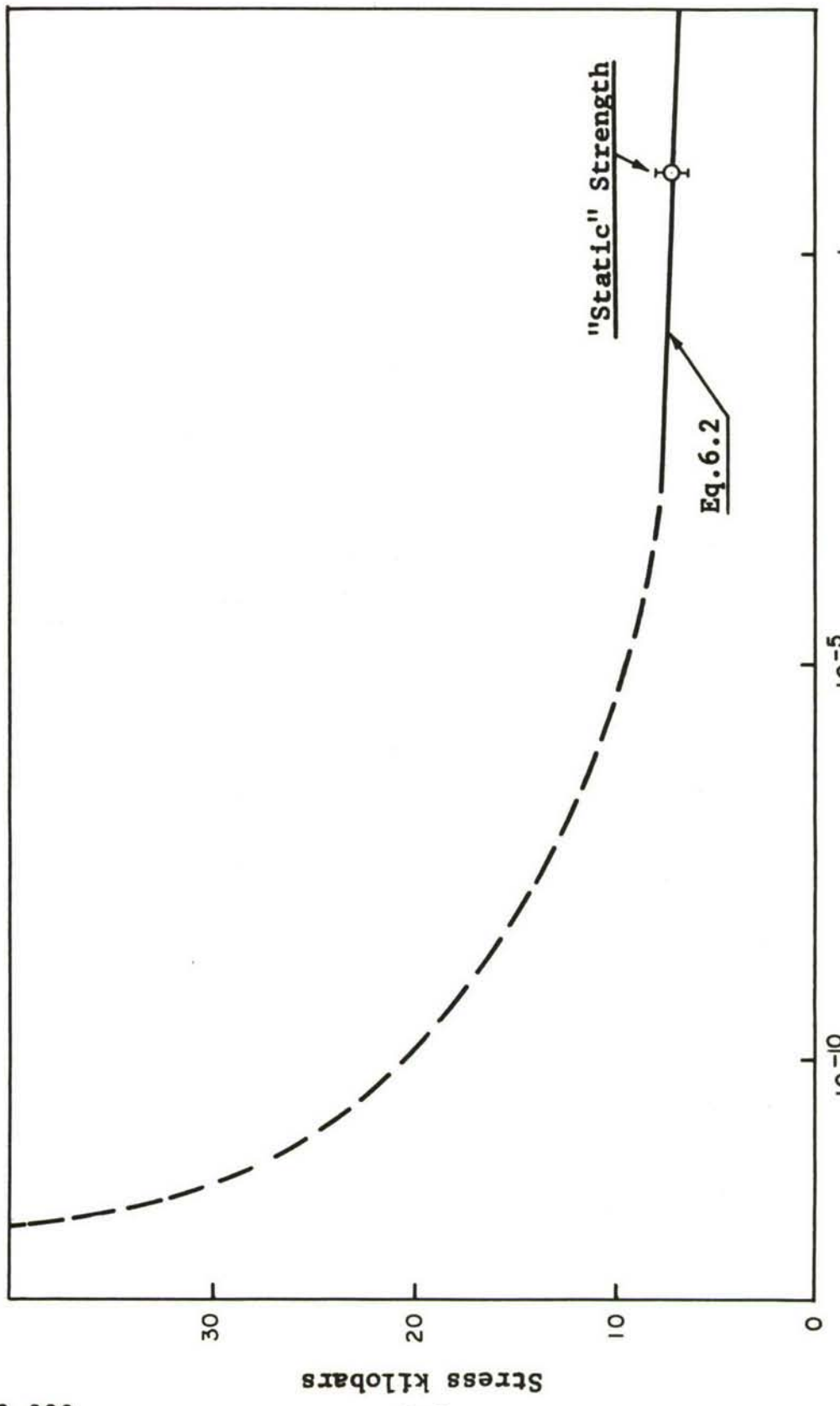


Fig. 6.7 Qualitative Upper Fracture Threshold Time Dependence for Half-Hard E.T.P. Copper

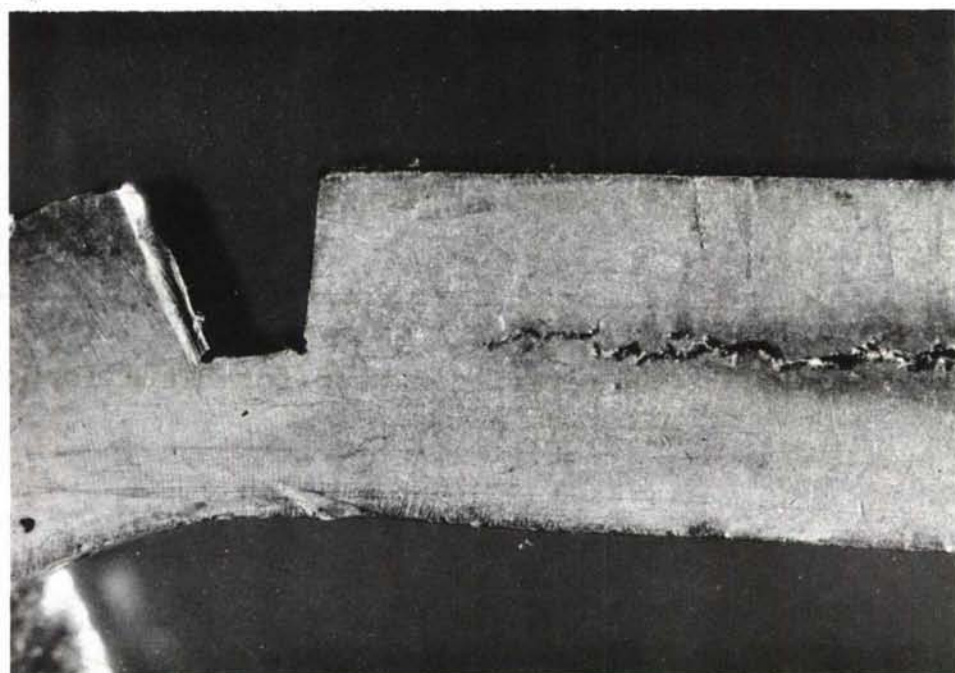


Fig.6.8 Edge Effect With Groove

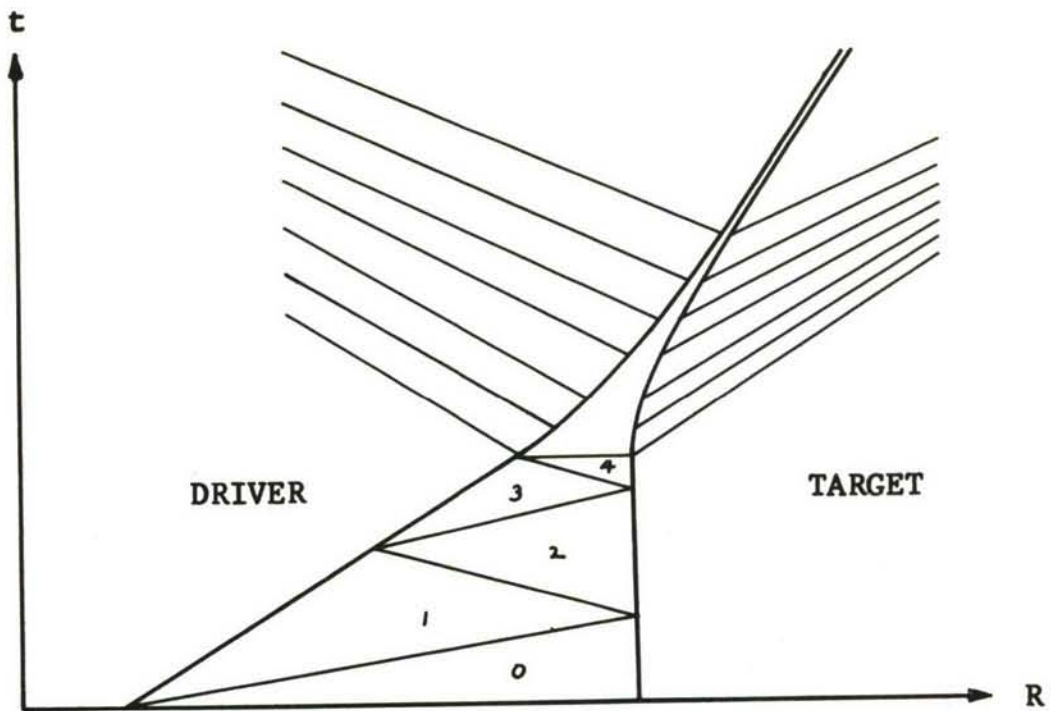


Fig. 7.1 Characteristic Mesh for Plate Impact with Air Present

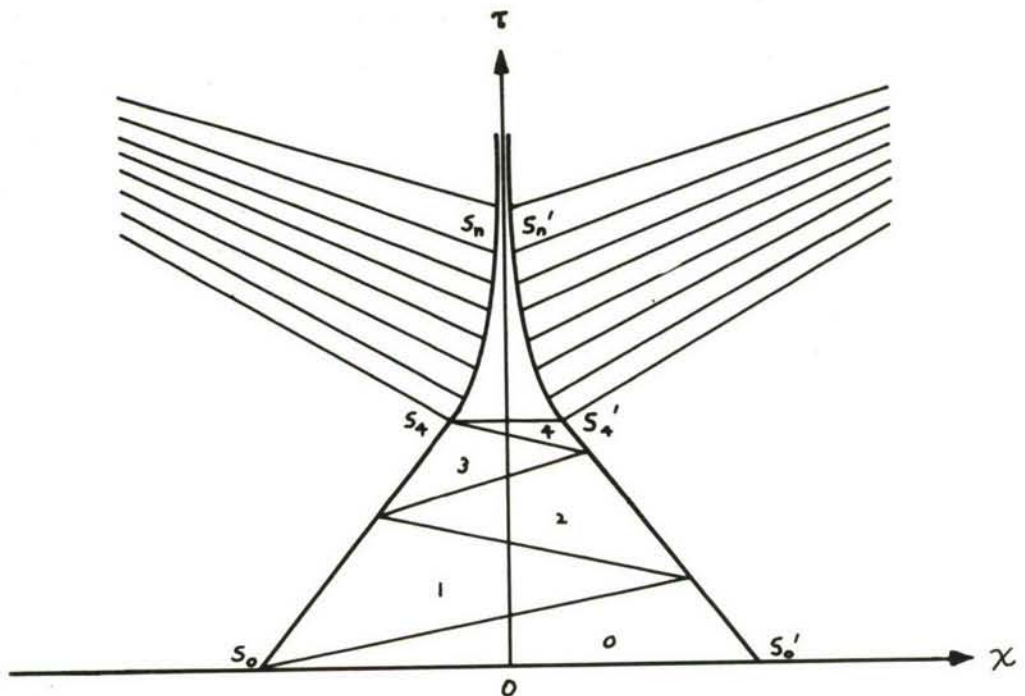


Fig. 7.2 Non-dimensionalised Characteristic Mesh
ASD-TDR-62-399

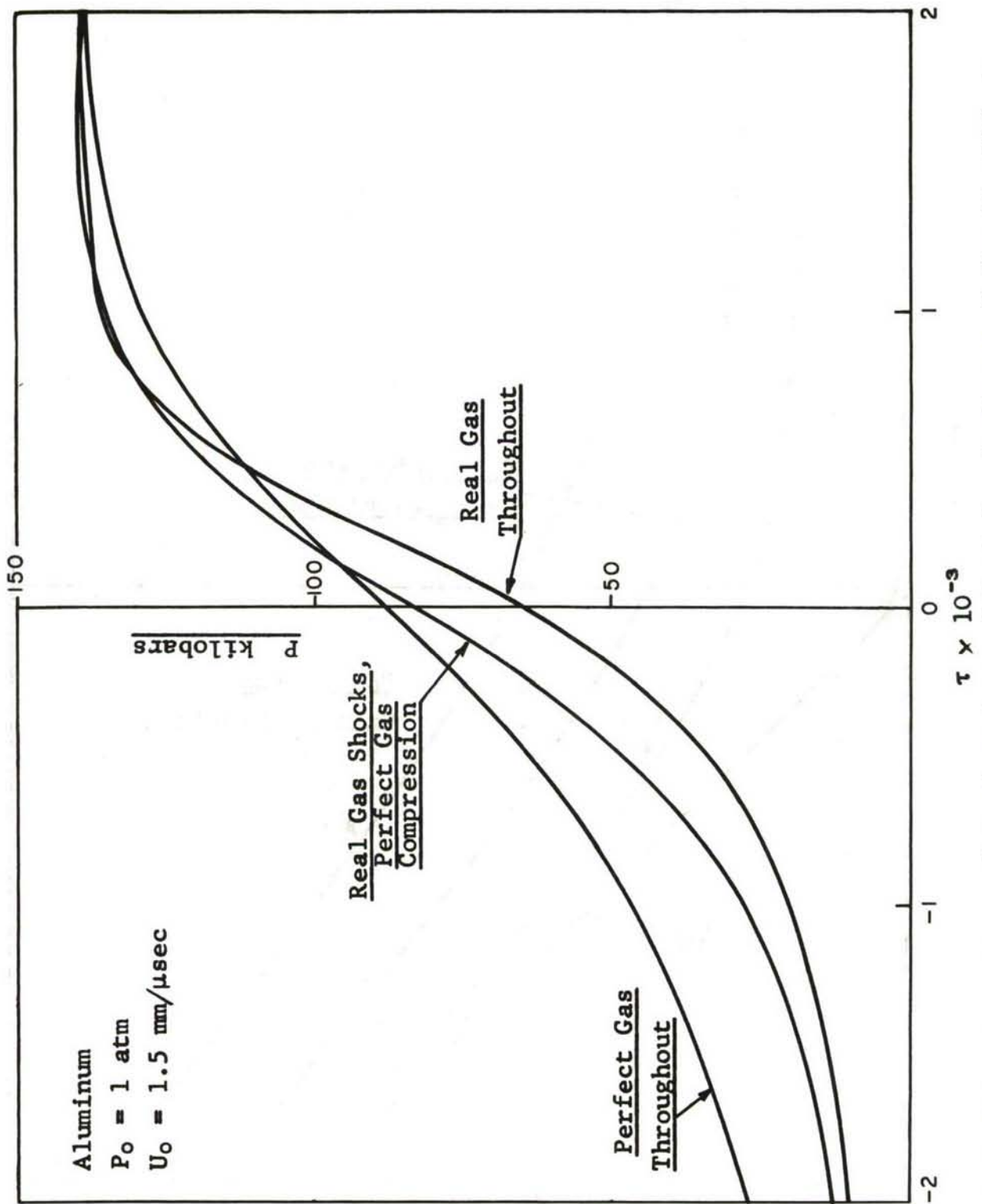


Fig. 7.3 Comparison of Perfect Gas and Real Gas Analyses of the Air Effect

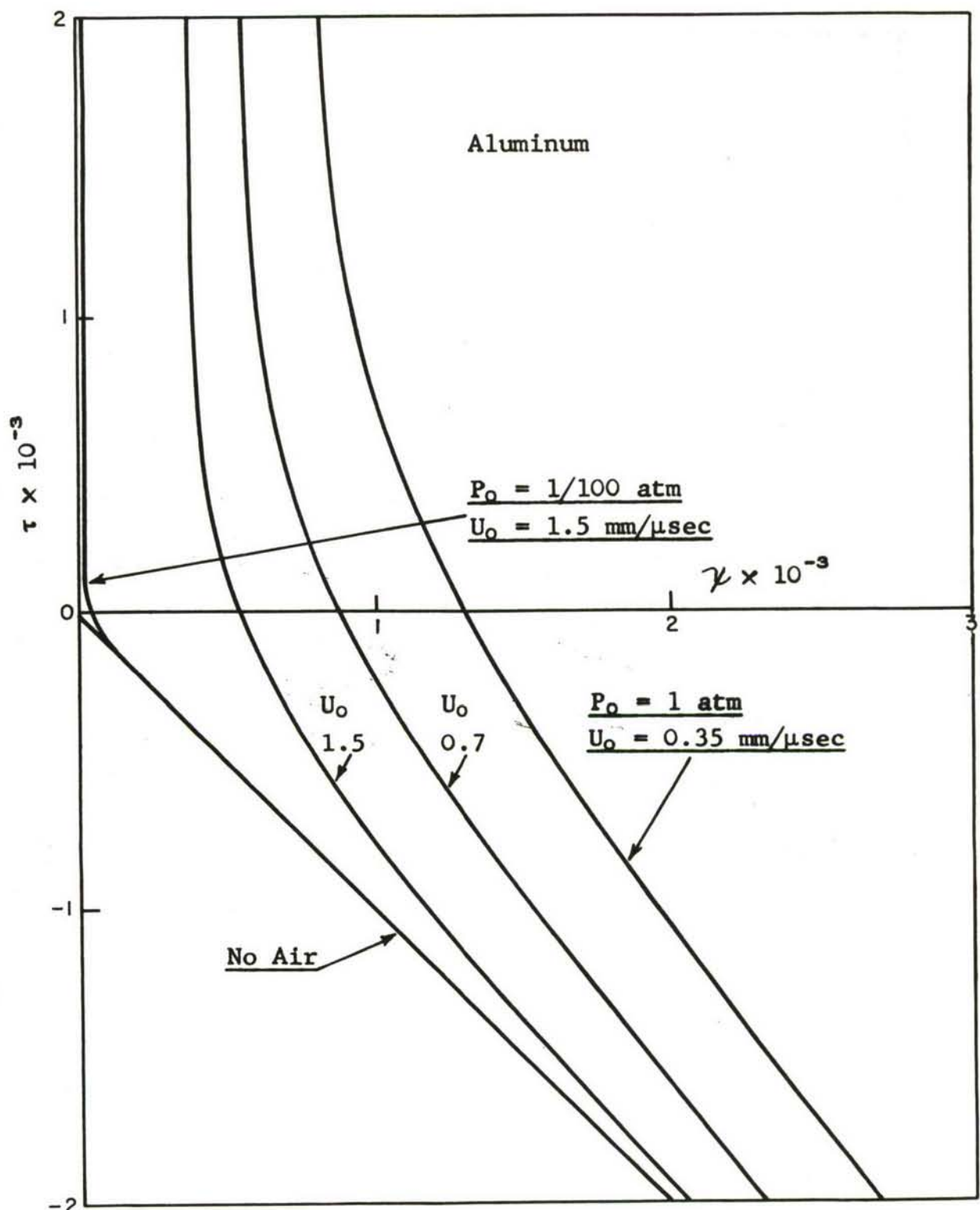


Fig. 7.4 Surface Trajectories in the Presence of Air

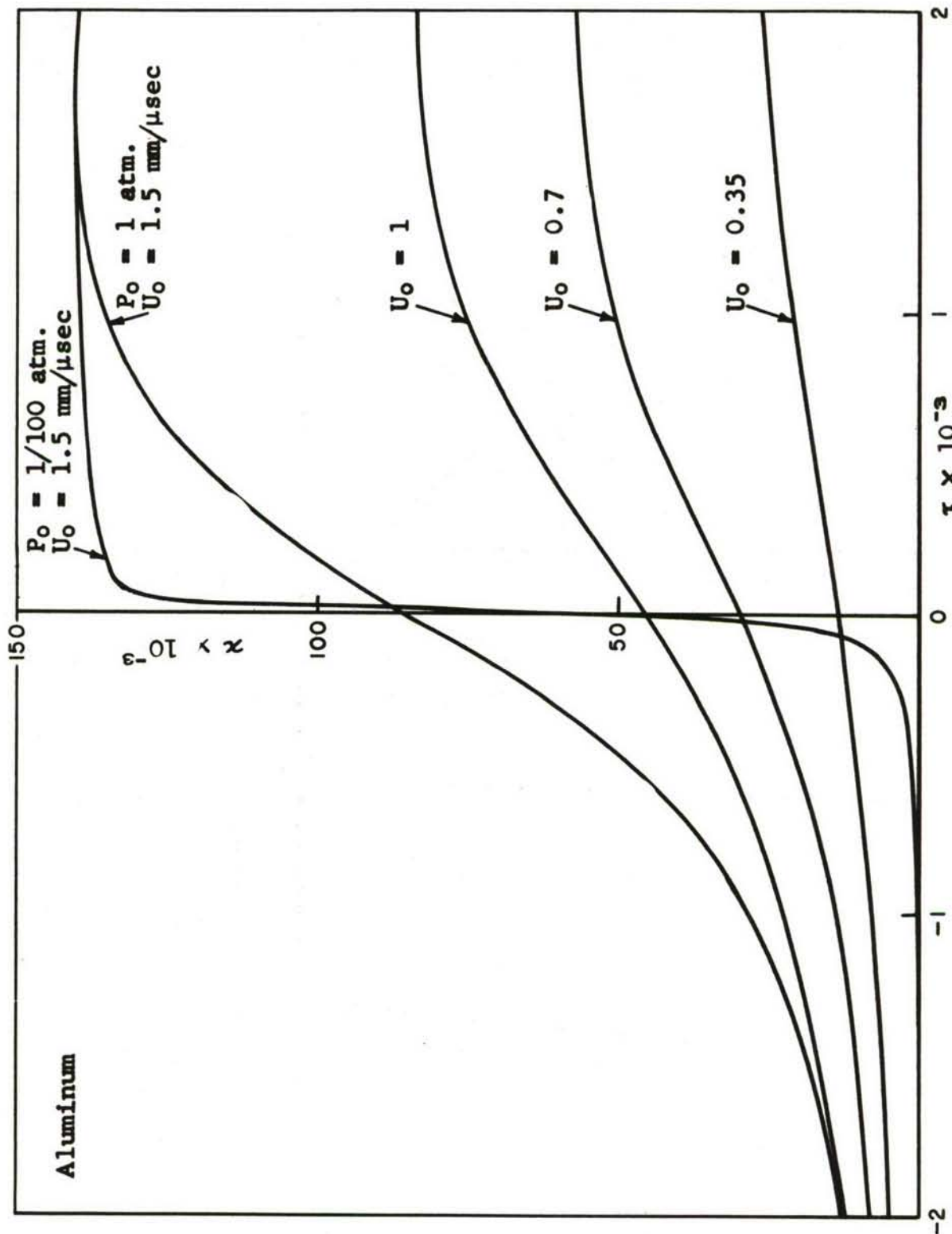


Fig. 7.5 Interface Pressure Profiles in the Presence of Air

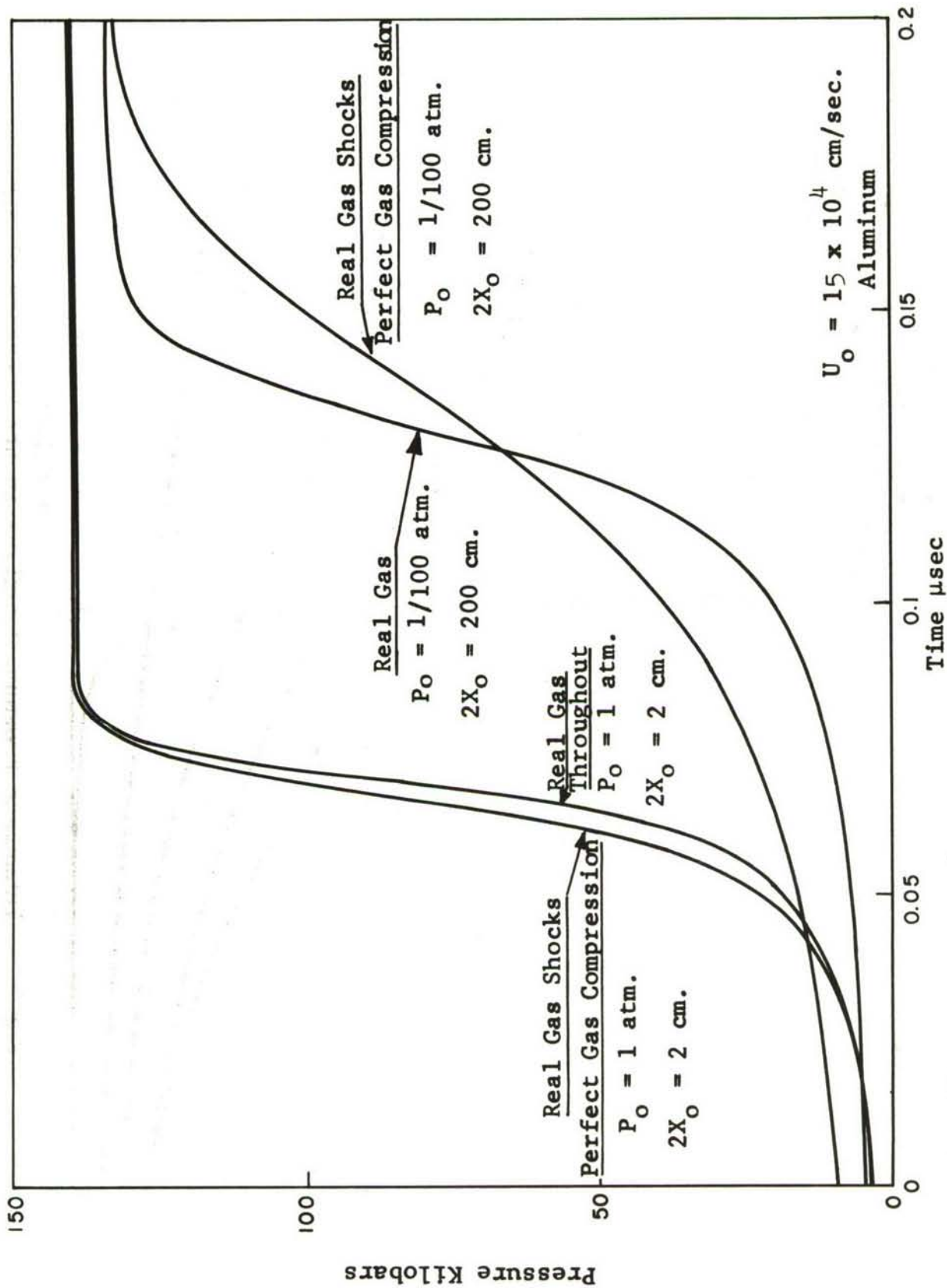


Fig. 7.6 Effect of Air Between Impacting Plates

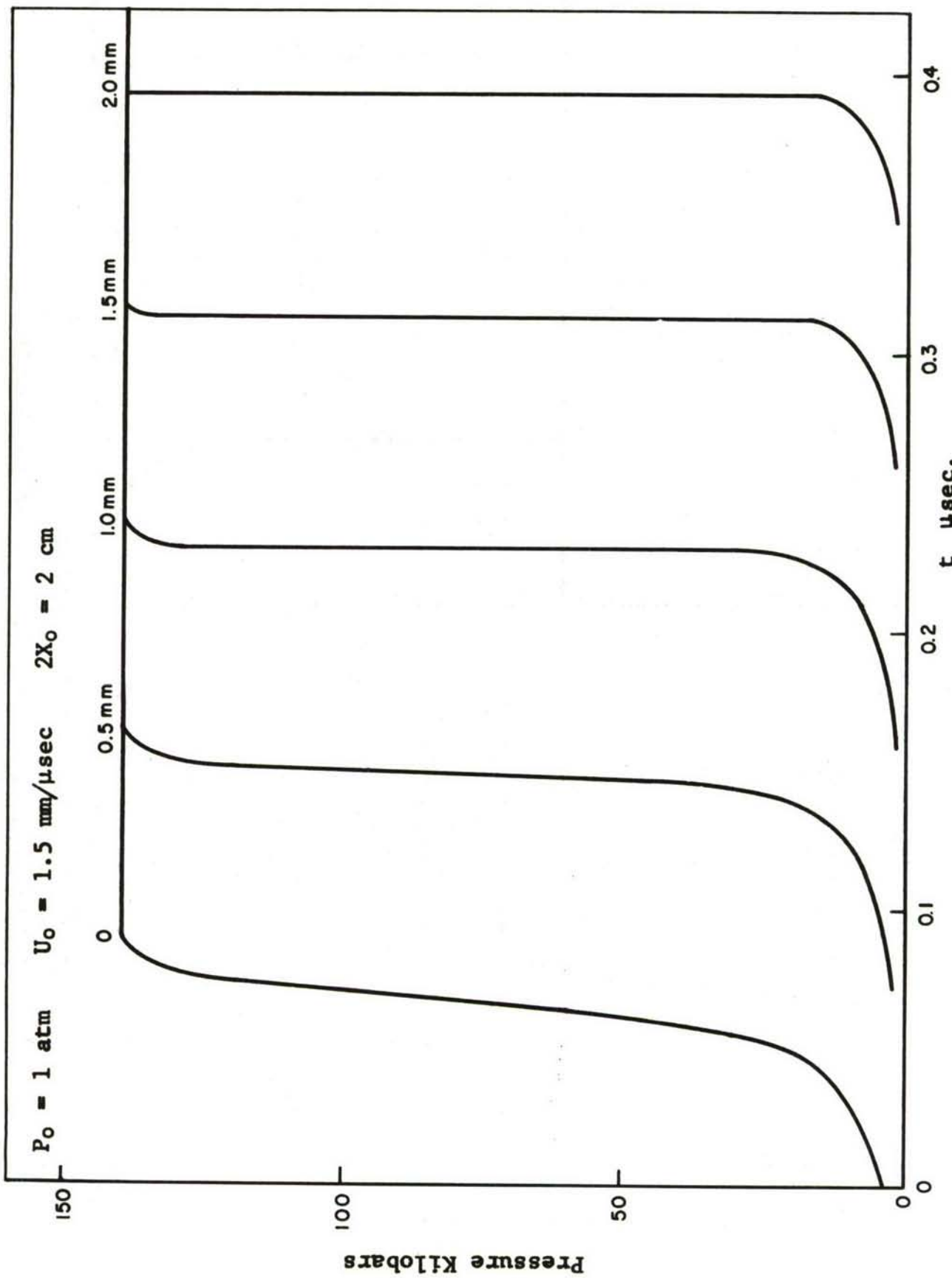


Fig. 7.7a Wave Profiles in the Target

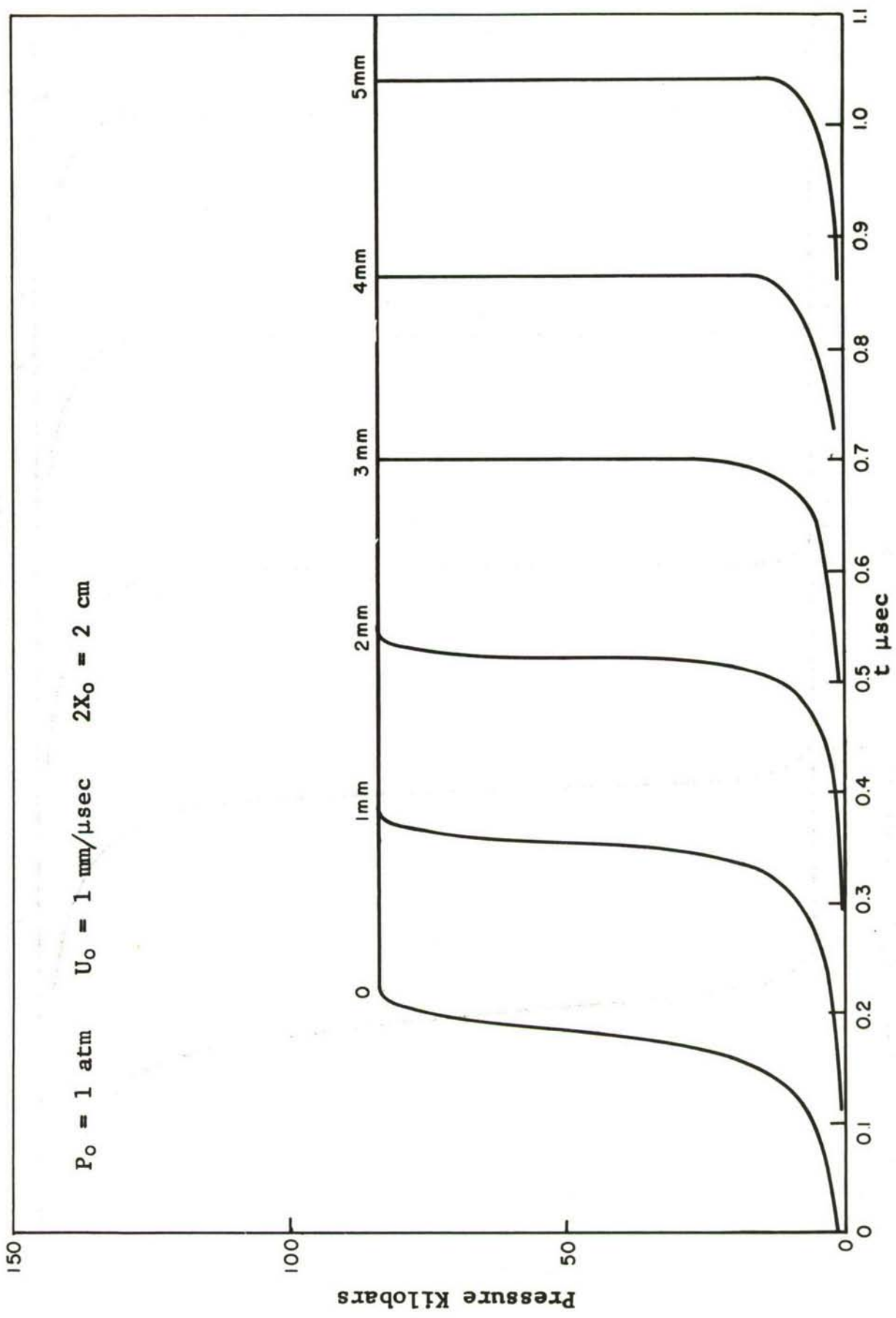
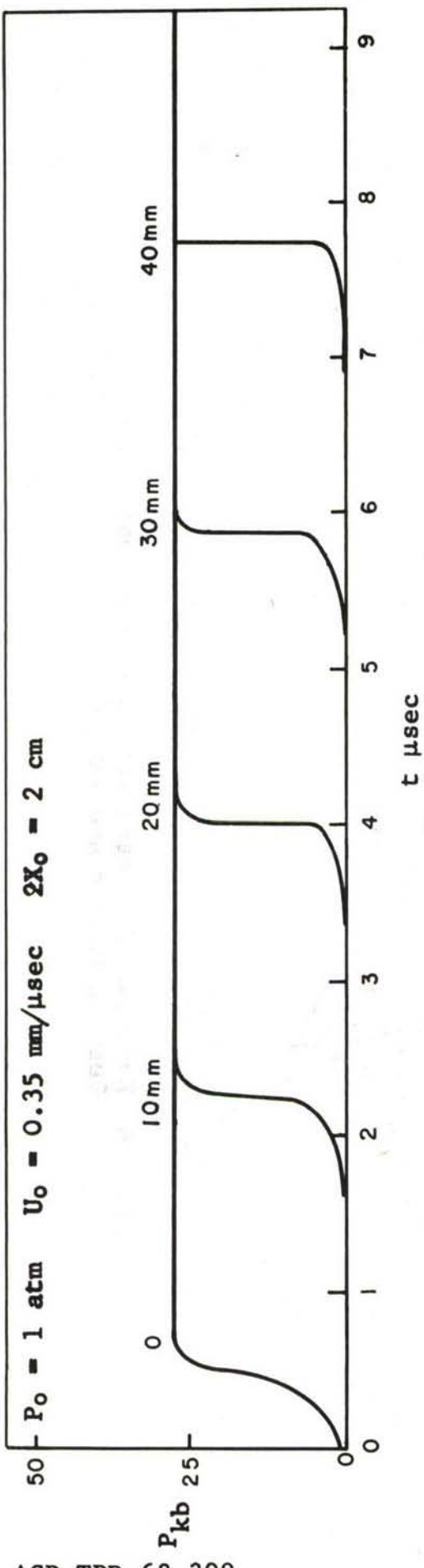
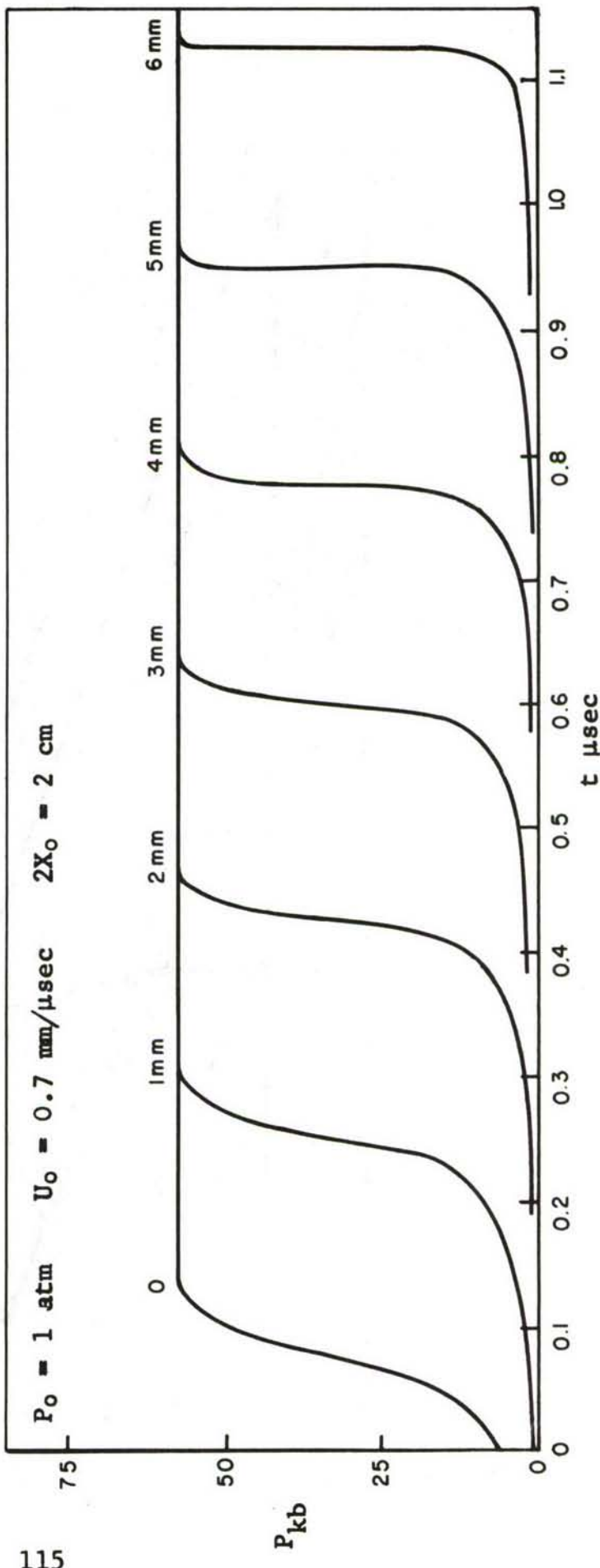


Fig. 7.7b Wave Profiles in the Target



ASD-TDR-62-399



115

Fig. 7.7c Wave Profiles in the Target

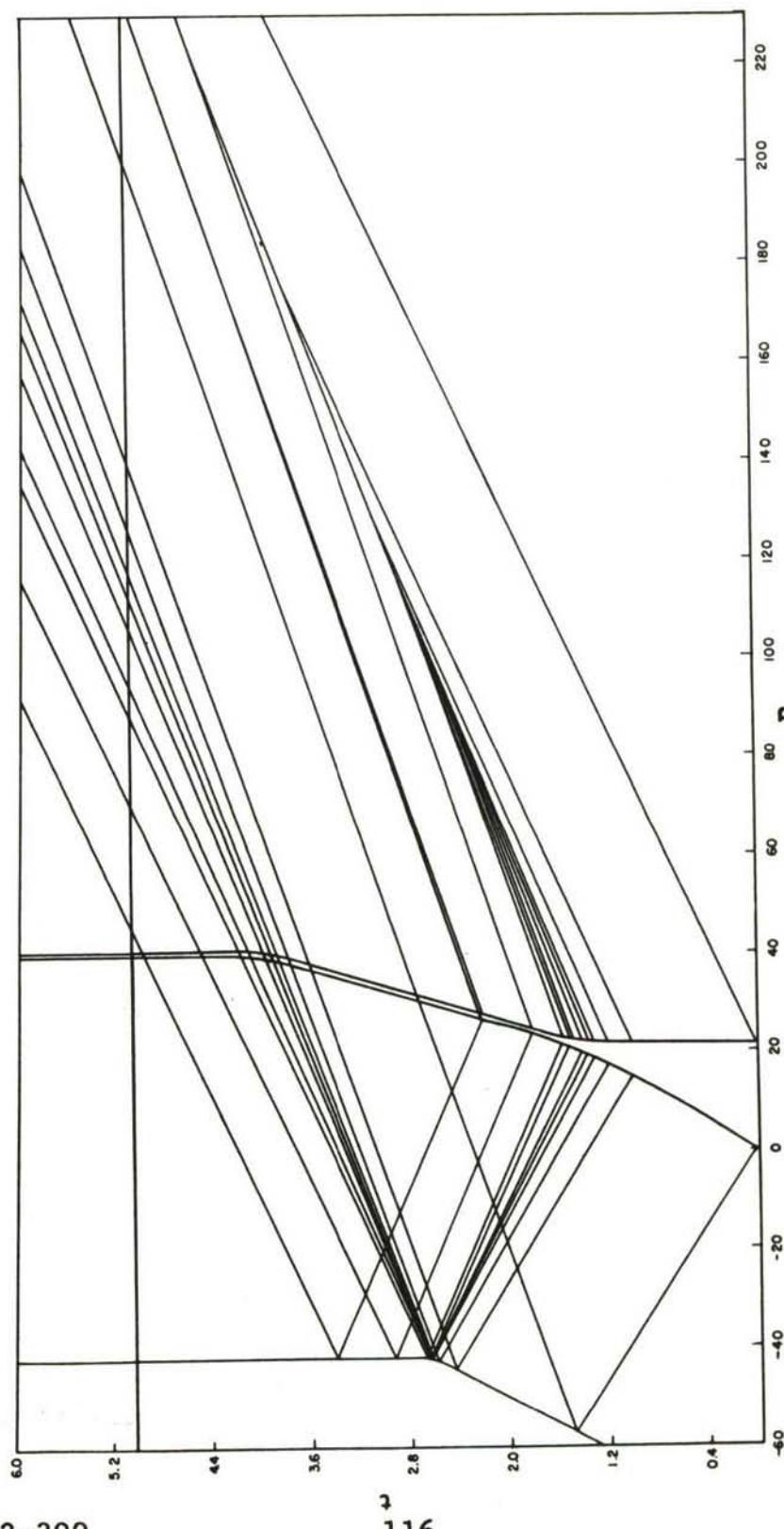


Fig. 7.8 Eulerian Characteristic Mesh for Impact with Air
Between Driver and Target

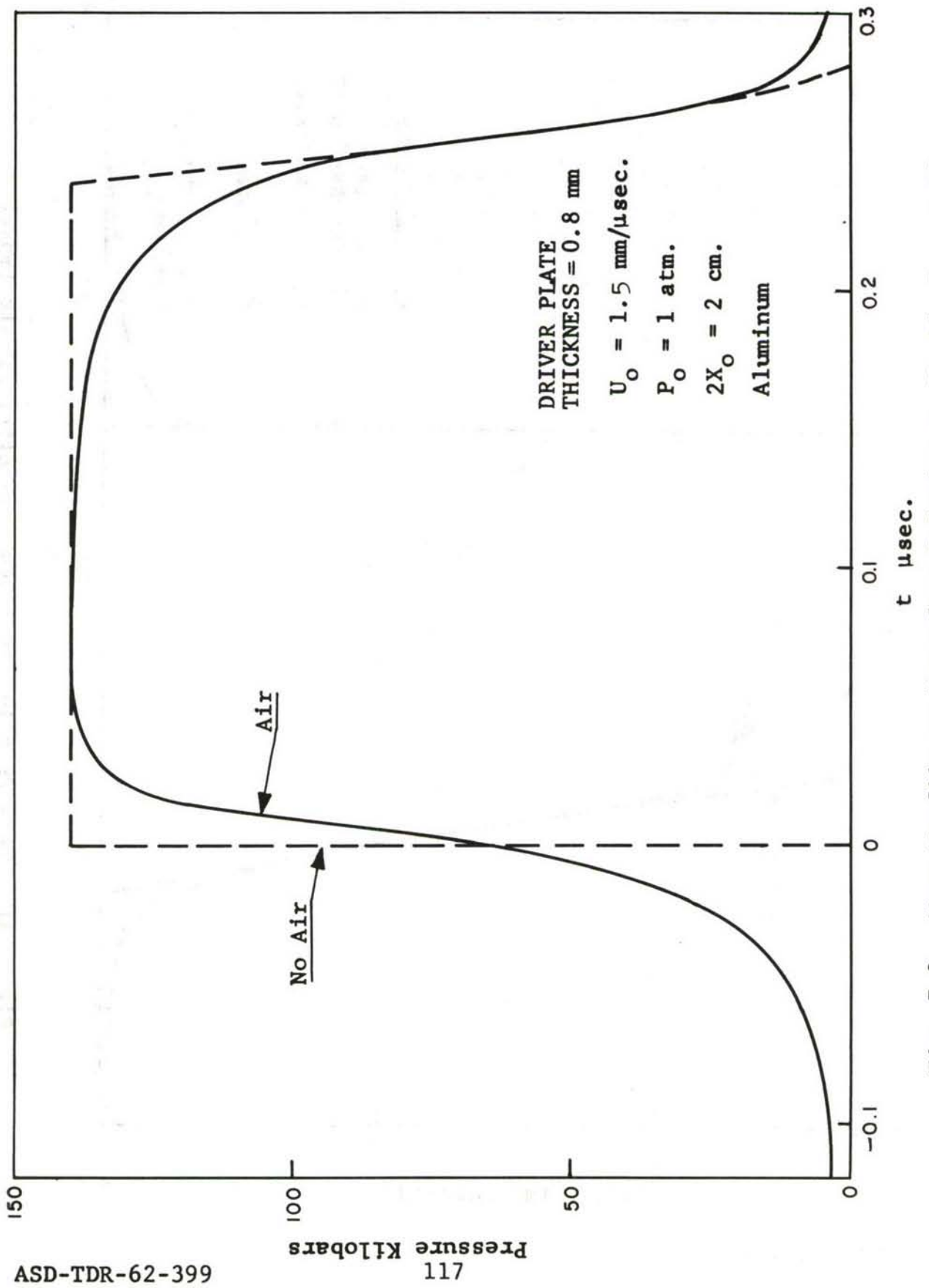


Fig. 7.9 Wave Profile at Interface Relative to No-Air Impact Time

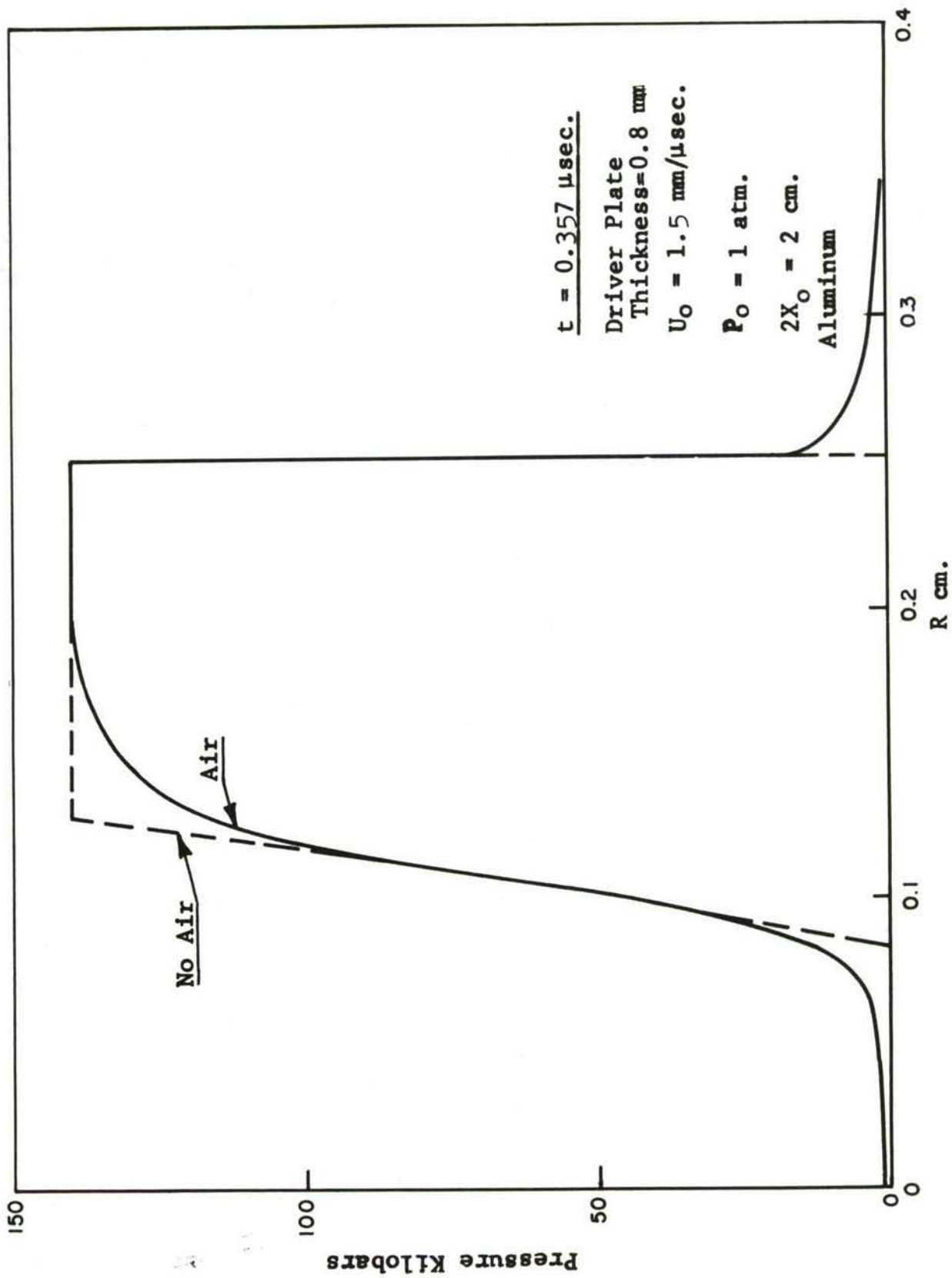


Fig. 7.10 Wave Profiles at Fixed Time After No-Air Impact

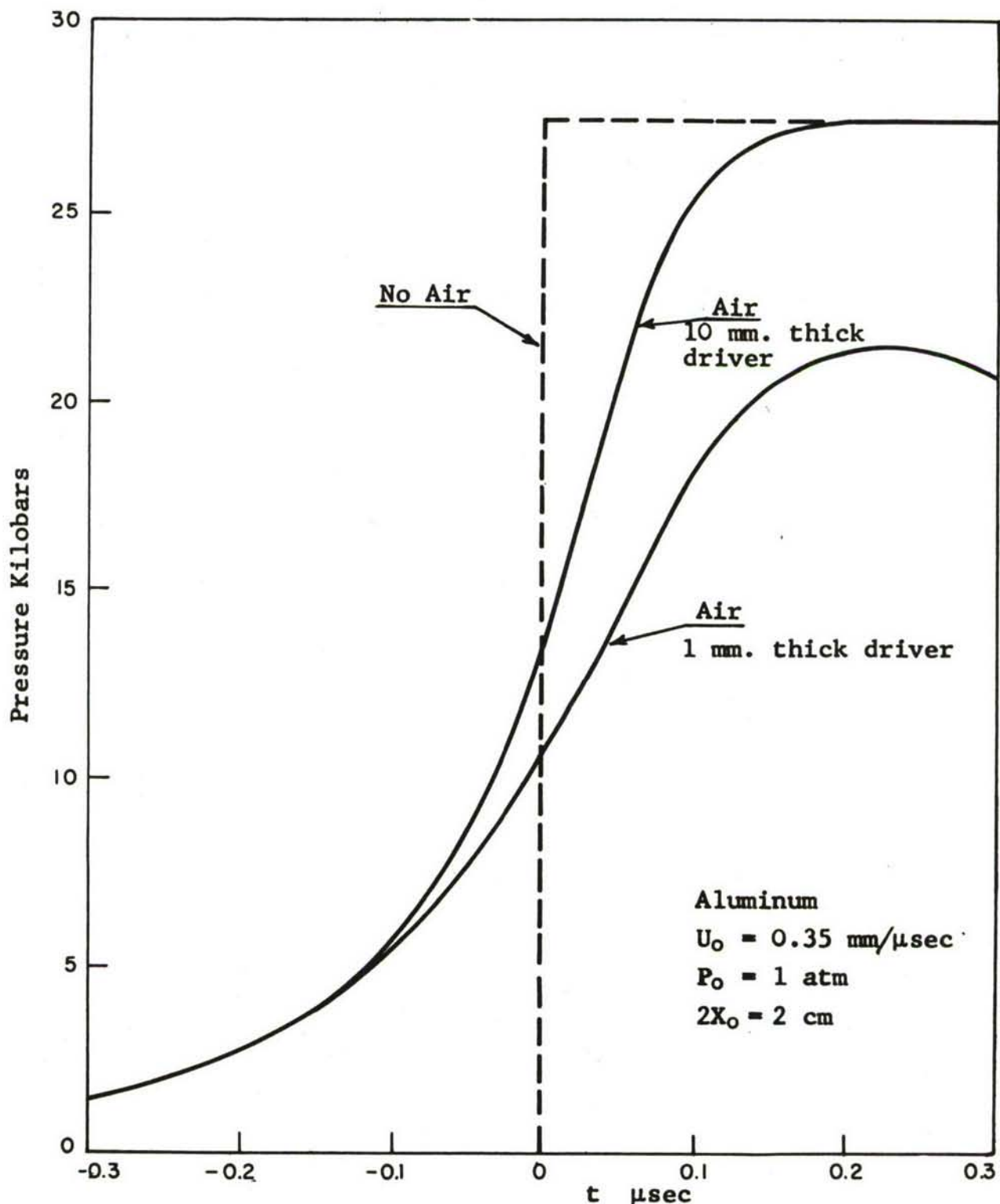


Fig. 7.11 Pressure Rise at the Interface for Thick and Thin Driver Plates

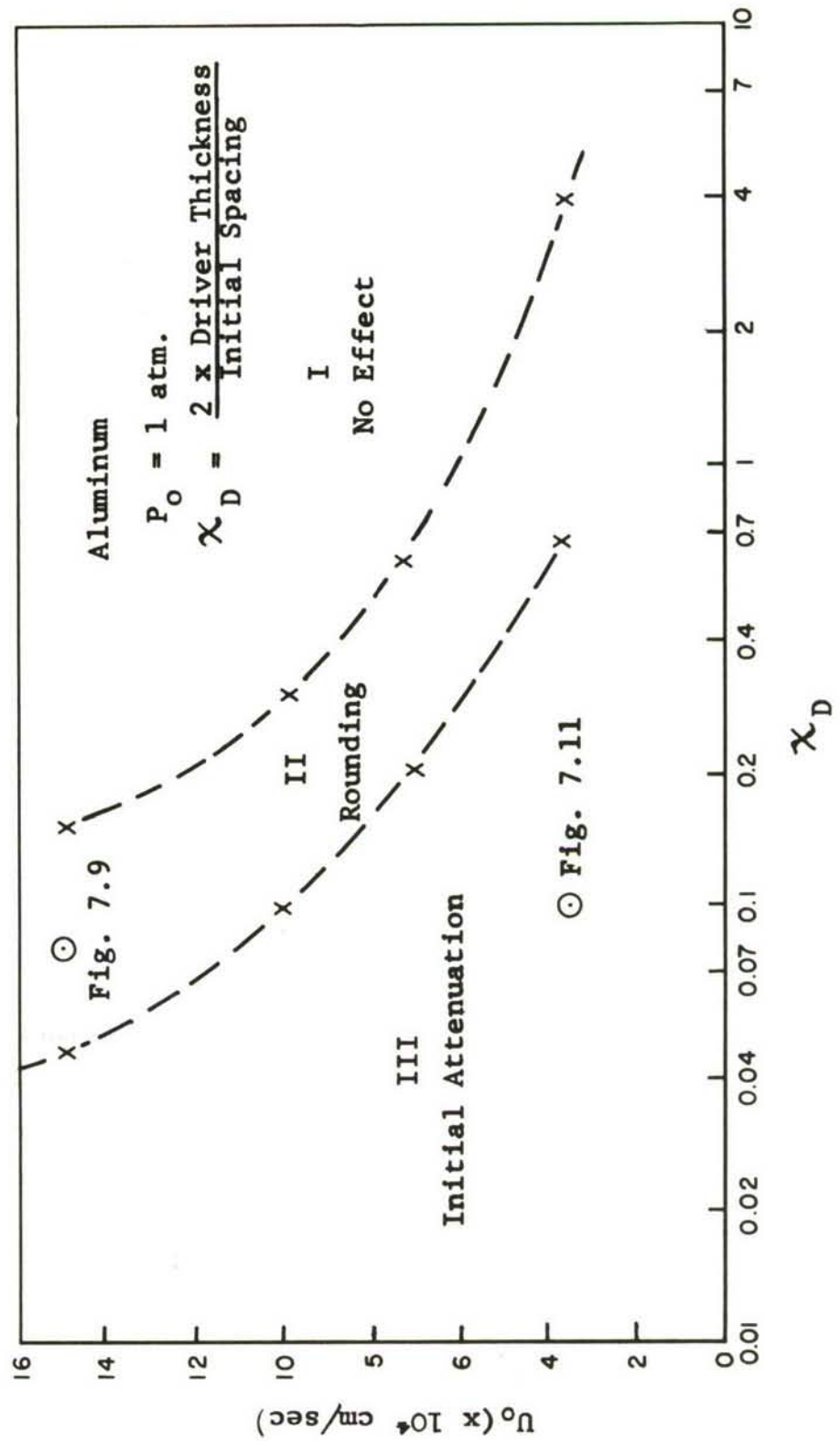


Fig. 7.12 Approximate Regions of Effects of Air in Plate Impact

Table I
Equation of State Data for Copper
(C.G.S. units throughout)

Hugoniot Data	Dugdale-MacDonald						Slater						Constant			Bridgeman Data		Thermo-Dynamic		Initial Conditions	
	\bar{V}_0	P_H	P_A	$P_T(298^\circ)$	P_K	γ	$E_{P=0}$	P_A	$P_T(298^\circ)$	P_K	γ	$E_{P=0}$	P_T	$E_{P=0}$	P_T	$E_{P=0}$	P_T	$E_{P=0}$	Quantity	Source	
1.06	-70.1	$\times 10^9$	$\times 10^9$	$\times 10^9$	$\times 10^9$	$\times 10^9$	$\times 10^9$	$\times 10^9$	$\times 10^9$	$\times 10^9$	$\times 10^9$	$\times 10^9$	$\times 10^9$	$\times 10^9$	$\times 10^9$	$\times 10^9$	$\times 10^9$	$\times 10^9$	$\times 10^9$	$\times 10^9$	$\times 10^9$
1.05	-60.0	-72.4	2.161	4.87	-82.2	2.132	4.26	-83.8	2.489	4.36	-73.7	2.376	3.91	-81.3	1.994	5.20	4.93	c	Data fit	3.96×10^6	
1.04	-49.3	-61.9	2.105	3.62	-61.9	2.277	3.41	-62.9	2.277	3.41	-62.9	2.277	3.41	-71.6	1.994	4.49	4.27	c	Bridge-man	3.92×10^6	
1.03	-37.9	-50.9	2.079	2.95	-50.9	2.054	2.25	-51.5	2.189	2.84	-51.5	2.189	2.84	-61.3	1.994	3.77	3.62	V_0	$298^\circ K$.1124	
1.02	-25.9	-39.1	2.054	2.25	-39.1	2.030	1.51	-39.5	2.116	2.20	-39.5	2.116	2.20	-50.3	1.994	3.04	2.93	$E_0 K$	$0^\circ K$	0	
1.01	-13.1	-26.6	2.030	1.51	-26.6	0	0	-26.8	2.057	1.51	-26.8	2.057	1.51	-38.7	1.994	2.29	2.18	E_0	Debye	7.52×10^9	
1.00	0	0	-13.3	1.994	.75	0	0	-13.3	1.994	.75	0	-13.3	1.994	-26.3	1.994	1.53	1.43	δ_0	Thermo-dynamic	1.983	
.9903	13.9	13.9	13.5	0	1.984	0	13.9	13.5	0	1.984	0	13.9	13.5	0	1.994	0	0	δ_0	Dugdale-MacDonald	1.994	
.98	30.0	30.0	29.1	15.8	1.960	30.0	29.1	15.8	1.968	30.0	29.1	15.8	1.968	30.0	29.1	15.6	1.994	29.7	δ_0	Slater	2.227
.97	46.3	46.2	44.9	31.7	1.938	46.2	44.9	31.5	1.968	46.2	44.9	31.5	1.968	46.2	44.9	31.4	1.994	.75	δ_0	Slater	37.71
.96	63.6	63.4	61.7	48.7	1.917	63.4	61.6	48.2	1.980	63.4	61.6	48.2	1.980	63.4	61.6	48.2	1.994	0	δ_0	$\frac{\partial \delta_0}{\partial V_0}$	1.984
.95	81.9	81.6	79.5	66.6	1.897	81.6	79.4	65.8	2.002	81.6	79.4	65.9	1.994	81.6	79.4	65.9	1.994	29.7	δ_0	$\frac{\partial \delta_0}{\partial V_0}$	20.45
.94	103.6	101.0	98.4	85.7	1.877	101.0	98.2	84.4	2.031	101.0	98.2	84.8	2.031	101.0	98.2	84.8	1.994	.75	δ_0	Slater	12.90 $\times 10^{12}$
.93	122.4	121.5	118.5	105.9	1.859	121.5	104.1	2.064	121.5	104.1	2.064	121.5	104.1	2.064	121.5	104.8	1.994	.75	δ_0	Slater	37.71
.92	144.7	143.4	127.5	1.841	143.3	125.1	2.096	143.3	125.1	2.096	143.3	125.1	2.096	143.3	126.1	1.994	.75	δ_0	Slater	37.71	
.91	168.2	166.5	150.2	1.825	166.3	147.2	2.124	166.3	147.2	2.124	166.3	147.2	2.124	166.3	148.6	1.994	.75	δ_0	Slater	37.71	
.90	193.5	191.1	174.5	1.810	190.8	170.8	2.144	190.8	170.8	2.144	191.0	170.8	2.144	191.0	172.6	1.994	.75	δ_0	Slater	37.71	
.89	220.5	217.3	200.2	1.796	216.8	195.9	2.154	216.8	195.9	2.154	217.0	195.9	2.154	217.0	197.9	1.994	.75	δ_0	Slater	37.71	
.88	249.4	245.0	227.6	1.783	244.3	222.8	2.152	244.3	222.8	2.152	244.6	222.8	2.152	244.6	224.9	1.994	.75	δ_0	Slater	37.71	
.87	280.2	256.6	217.2	1.772	251.2	213.9	2.152	251.2	213.9	2.152	253.4	213.9	2.152	253.4	224.9	1.994	.75	δ_0	Slater	37.71	
.86	313.2	287.4	1.760	1.760	281.6	2.114	1.760	281.6	2.114	1.760	283.7	2.114	1.760	283.7	283.7	1.994	.75	δ_0	Slater	37.71	

TABLE II
Equation of State Data For Aluminum

Hugoniot Data		Dugdale-MacDonald				Slater				Constant				Bridgeman Data		Thermo-Dynamic		Initial Conditions		
V _o	P _H	P _A	P _T (298°)	P _K	γ	E _{P=0}	P _A	P _T (298°)	P _K	γ	E _{P=0}	P _A	P _T (298°)	P _K	γ	E _{P=0}	P _T	Quant- ity	Source	
1.05	-35.1	x10 ⁹	x10 ⁹	x10 ⁹	x10 ⁹	x10 ⁹	x10 ⁹	x10 ⁹	x10 ⁹	x10 ⁹	x10 ⁹	x10 ⁹	x10 ⁹	x10 ⁹	x10 ⁹	x10 ⁹	x10 ⁹	a	Data fit	1.339
1.04	-28.8	-36.5	-42.5	1.923	8.82	-43.3	2.147	8.10	-42.8	2.028	8.47	-36.7	2.028	7.13	6.45	7.55	c	Data fit	.537x10 ⁶	
1.03	-22.1	-30.2	-36.5	1.959	7.31	-37.1	2.117	6.90	-30.6	2.091	5.65	-30.3	2.028	5.77	5.33	6.45	c	Bridge- man	.522x10 ⁶	
1.02	-15.0	-23.5	-30.2	1.987	5.85	-30.6	2.068	4.34	-23.7	2.068	4.39	-23.5	2.028	4.39	4.15	5.33	V _o	298°K	.3591	
1.01	-7.6	-16.4	-16.4	2.019	3.00	-16.5	2.046	2.98	-16.3	2.028	3.00	-8.7	2.028	1.58	0	8.3	0	0°K	0	
1.00	0	0	-8.8	2.019	1.58	0	0	-8.8	2.026	1.58	0	9.3	8.9	0	2.028	0	8.3	0	Debye	1.583x10 ⁹
.989	9.3	9.3	8.9	0	2.005	0	9.3	8.9	0	2.005	0	17.2	16.6	7.7	2.028	15.5	15.5	Thermo- dynamic	2.028	
.98	17.2	17.2	16.6	7.8	1.983	17.2	16.6	7.8	1.988	16.7	1.969	26.4	25.4	16.6	2.028	24.0	24.0	Dugdale- MacD.	1.678	
.97	26.4	26.4	25.5	16.9	1.947	26.4	25.5	16.7	1.969	26.4	1.948	36.1	34.8	26.0	2.028	32.9	32.9	Slater	2.011	
.96	36.2	36.1	34.8	26.5	1.899	36.1	34.8	26.2	1.948	36.1	1.948	46.3	44.6	35.8	2.028	44.6	44.6	Dugdale- MacD.	7.83	
.95	46.5	46.3	44.8	36.7	1.840	46.3	44.7	36.3	1.926	46.3	1.926	57.1	55.0	46.3	2.028	55.0	55.0	Slater	9.96	
.94	57.3	57.1	55.3	47.6	1.773	57.1	55.1	46.9	1.903	57.1	1.877	68.5	66.0	57.3	2.028	66.0	66.0	0°K	2.005	
.93	68.8	68.5	66.4	59.1	1.700	68.5	66.2	58.1	1.877	68.5	1.849	80.4	77.5	68.9	2.028	77.5	77.5	0°K	.3550	
.92	81.0	80.5	78.2	71.2	1.623	80.5	77.8	69.9	1.849	80.4	1.820	93.0	89.7	81.1	2.028	89.7	89.7	0°K	-2.32x10 ¹²	
.91	93.9	93.2	90.6	84.1	1.548	93.1	90.1	82.4	1.820	93.0	1.789	106.3	102.5	94.0	2.028	102.5	102.5	0°K		
.90	107.5	106.6	103.8	97.7	1.476	106.4	103.1	95.5	1.789	109.5	1.758	120.3	107.5	94.0	2.028	107.5	107.5	0°K		
.89	122.	120.7	112.0	1.411	120.5	120.5	120.5	120.5	120.5	124.2	1.726	135.1	121.8	121.8	2.028	121.8	121.8	0°K		
.88	137.	135.7	127.1	1.355	135.4	135.4	135.4	135.4	135.4	139.7	1.695	150.6	136.9	136.9	2.028	136.9	136.9	0°K		
.87	153.	151.5	143.0	1.311	151.0	151.0	151.0	151.0	151.0	156.1	1.666	166.9	152.7	152.7	2.028	152.7	152.7	0°K		
.86	170.	168.3	159.7	1.280	167.6	167.6	167.6	167.6	167.6	173.4	1.638	184.1	169.4	169.4	2.028	169.4	169.4	0°K		
.85	189.	185.9	177.3	1.261	185.0	185.0	185.0	185.0	185.0	191.6	1.612	202.1	186.9	186.9	2.028	186.9	186.9	0°K		
.84	208.	204.6	195.7	1.254	203.5	203.5	203.5	203.5	203.5	210.9	1.589	221.1	205.3	205.3	2.028	205.3	205.3	0°K		
.83	229.	224.3	215.2	1.255	223.0	223.0	223.0	223.0	223.0	243.4	1.568	241.1	224.7	224.7	2.028	224.7	224.7	0°K		
.82	251.	245.1	235.7	1.264	243.4	243.4	243.4	243.4	243.4	243.4	1.568	241.1	224.7	224.7	2.028	224.7	224.7	0°K		

TABLE III
Summary of Data for the Second Order U_s/U_p Relation for Aluminum
(C.G.S. units throughout)

$\frac{V}{V_{0H}}$	Hugoniot	Constant	Bridgman	Birch	Constant	Thermo-dynamic
	$P_H \times 10^9$	$P_T \times 10^9$	$P_T \times 10^9$	$P_T \times 10^9$	$E_{P=0} \times 10^9$	$E_{P=0} \times 10^9$
1.05	- 32.80		-33.4	8.014	7.551	0.86
1.04	- 26.92		-27.3	6.772	6.452	0.84
1.03	- 20.71		-20.9	5.509	5.334	0.82
1.02	- 14.12		-14.2	4.223	4.146	0.80
1.01	- 7.15		- 7.2	2.914	2.857	0.78
1.00	0	0	0	1.583	1.583	0.76
0.9891	8.77	8.41	8.35	8.6	0	0.74
0.98	16.33	15.69	15.51	16.2		0.72
0.97	25.11	24.13	23.99	24.8		0.70
0.96	34.43	33.10	32.86	33.8		0.68
0.95	44.31	42.62	42.62	43.4		0.66
0.94	54.82	52.77	52.77	53.3		0.64
0.93	65.98	63.56	63.56	64.0		0.62
0.92	77.85	75.01	75.01	75.1		0.60
0.91	90.48	87.25	87.25	86.7		0.5882
0.90	103.9	100.2	99.0	99.0		3.88

TABLE IV
High Pressure Equation of State of Copper
(C.G.S. units throughout)

$\frac{V}{V_{0H}}$	Hugoniot	McQueen, Marsh	Altshuler
	$P_H \times 10^{12}$	$P_K \times 10^{12}$	$P_K \times 10^{12}$
1.05	0.315	0.288	1.73
1.04	0.388	0.355	1.74
1.03	0.474	0.429	1.74
1.02	0.566	0.514	1.73
1.01	0.689	0.611	1.70
1.00	0.825	0.725	1.68
0.9891	0.978	0.857	1.66
0.98	1.000	1.000	1.63
0.97	1.17	1.17	1.63
0.96	1.167	1.167	1.60
0.95	2834	1.179	1.61
0.94		1.375	1.57
0.93		1.601	1.54
0.92		1.858	1.53
0.91		2.158	1.53
0.90		2.504	1.53

Initial Conditions	
γ	2.028
c	5.218×10^5 cm/sec
s	1.436
h	-0.0118×10^{-5} sec/cm
λ	591×10^9 dy/cm ²
μ	250×10^9 dy/cm ²

TABLE V
Principal Components of Stress Increment and Strain Increment in Uniaxial Strain

		Principal Components	Spherical Component	Deviatoric Principal Components
Stress Increment	Elastic	$d\sigma_x$; $\frac{3K-2G}{3K+4G} d\sigma_x$; $\frac{3K-2G}{3K+4G} d\sigma_x$	$\frac{3K}{3K+4G} d\sigma_x$	$\frac{4G}{3K+4G} d\sigma_x$; $\frac{-2G}{3K+4G} d\sigma_x$; $\frac{-2G}{3K+4G} d\sigma_x$
	Plastic* $\sigma_x - \sigma_y = \pm \gamma$	$d\sigma_x$; $d\sigma_x \mp d\gamma$; $d\sigma_x \mp d\gamma$	$d\sigma_x \mp \frac{2}{3} d\gamma$	$\pm \frac{2}{3} d\gamma$; $\mp \frac{1}{3} d\gamma$; $\mp \frac{1}{3} d\gamma$
Strain Increment	Elastic	de_x ; 0; 0	$\frac{1}{3} de_x$	$\frac{2}{3} de_x$; $-\frac{1}{3} de_x$; $-\frac{1}{3} de_x$
	Plastic; Elastic Component	de_x^e ; $\frac{1}{2} de_x^p$; $\frac{1}{2} de_x^p$	$\frac{1}{3} de_x$	$\frac{1}{3} (2de_x^e - de_x^p)$; $-\frac{1}{6} (2de_x^e - de_x^p)$; $-\frac{1}{6} (2de_x^e - de_x^p)$
	Plastic; Plastic Component	de_x^p ; $-\frac{1}{2} de_x^p$; $-\frac{1}{2} de_x^p$	0	de_x^p ; $-\frac{1}{2} de_x^p$; $-\frac{1}{2} de_x^p$

*The upper sign is appropriate when $d\sigma_x$ is positive; the lower sign when $d\sigma_x$ is negative.

TABLE VI
 Multiple Shock Reflection Parameters
 (C.G.S. units throughout)

U_o $\times 10^4$	Region	PERFECT GAS			REAL GAS		
		P $\times 10^6$	ρ $\times 10^{-3}$	T °K	P $\times 10^6$	ρ $\times 10^{-3}$	T °K
15	0	1.013	1.173	300	*	*	*
	1	34.54	5.998	2000	*	*	*
	2	233.4	19.53	4151	213.8	25.70	3300
	3	971.0	49.91	6760	902.9	70.78	4650
	4	3084.9	109.1	9820	2796.0	195.0	5900
10	0	1.013	1.173	300	*	*	*
	1	16.17	5.169	1086	*	*	*
	2	93.27	15.640	2071	*	*	*
	3	357.8	38.19	3255	327.8	40.26	2600
	4	1080.1	80.93	4636	978.6	83.16	3800
7	0	1.013	1.173	300	*	*	*
	1	8.931	4.267	727	*	*	*
	2	41.91	11.63	1251	*	*	*
	3	143.2	26.57	1872	*	*	*
	4	400.6	53.70	2591	359.4	57.53	2250
3.5	0	1.013	1.173	300	*	*	*
	1	3.541	2.714	453	*	*	*
	2	10.05	5.538	630	*	*	*
	3	24.70	10.31	832	*	*	*
	4	54.48	17.88	1058	*	*	*

* Same as perfect gas conditions.

1. Solids
2. Solid dynamics
3. Pressure studies
I. AFSC Project 6906.
Task 690601
II. Contract AF 33
(616)-6373
III. Massachusetts Institute of Technology, Cambridge, Mass.

A discussion of the analytical methods of predicting uniaxial stress wave propagation and spall as a result of uniformly distributed intense impulsive loading is given. For the materials for which data currently exists, no strain-rate effects are observed on yield (i.e. two aluminum alloys) and the strain-rate

(over)

IV. W. Herrmann, et al.
V. Aval fr OTS
VI. In ASTIA collection

Aeronautical Systems Division, Dir/Aeronautics, Flight Dynamics Lab, Wright-Patterson AFB, Ohio.
Rpt Nr ASD-TDR-62-399. STRESS WAVE PROPAGATION AND SPAILLATION IN UNIAXIAL STRAIN. Final report, Sept 62, 125p. incl illus., tables, 41 refs.

Unclassified Report

1. Solids
2. Solid dynamics
3. Pressure studies
I. AFSC Project 6906.
Task 690601
II. Contract AF 33
(616)-6373
III. Massachusetts Institute of Technology, Cambridge, Mass.

A discussion of the analytical methods of predicting uniaxial stress wave propagation and spall as a result of uniformly distributed intense impulsive loading is given. For the materials for which data currently exists, no strain-rate effects are observed on yield (i.e. two aluminum alloys) and the strain-rate

(over)

effect on the fracture threshold is found to be small (copper). For such materials a detailed analytical treatment is possible, once the constants associated with the constitutive equation and fracture criterion are evaluated. The plate impact experiment provides a convenient means of evaluating these constants. Considerations entering into the interpretation of the plate impact experiment and a detailed analysis of the effect of air between the impacting plates, are given.

effect on the fracture threshold is found to be small (copper). For such materials a detailed analytical treatment is possible, once the constants associated with the constitutive equation and fracture criterion are evaluated. The plate impact experiment provides a convenient means of evaluating these constants. Considerations entering into the interpretation of the plate impact experiment and a detailed analysis of the effect of air between the impacting plates, are given.

1. Aeronautical Systems Division, Dir/Aeromechanics, Flight Dynamics Lab, Wright-Patterson AFB, Ohio.

Rpt Nr ASD-TDR-62-399. STRESS WAVE PROPAGATION AND SPALLATION IN UNIAXIAL STRAIN. Final report, Sept 62, 125p. incl illus., tables, 41 refs.

Unclassified Report

A discussion of the analytical methods of predicting uniaxial stress wave propagation and spall as a result of uniformly distributed intense impulsive loading is given. For the materials for which data currently exists, no strain-rate effects are observed on yield (i.e. two aluminum alloys) and the strain-rate

IV. W. Herrmann, et al.
V. Aval fr OTS
VI. In ASTIA collection

(over)

effect on the fracture threshold is found to be small (copper). For such materials a detailed analytical treatment is possible, once the constants associated with the constitutive equation and fracture criterion are evaluated. The plate impact experiment provides a convenient means of evaluating these constants. Considerations entering into the interpretation of the plate impact experiment and a detailed analysis of the effect of air between the impacting plates, are given.

1. Solids
2. Solid dynamics
3. Pressure studies
I. AFSC Project 6906.
Task 690601
II. Contract AF 33
(616)-6373
III. Massachusetts Institute of Technology, Cambridge, Mass.

Aeronautical Systems Division, Dir/Aeromechanics, Flight Dynamics Lab, Wright-Patterson AFB, Ohio.

Rpt Nr ASD-TDR-62-399. STRESS WAVE PROPAGATION AND SPALLATION IN UNIAXIAL STRAIN. Final report, Sept 62, 125p. incl illus., tables, 41 refs.

Unclassified Report

A discussion of the analytical methods of predicting uniaxial stress wave propagation and spall as a result of uniformly distributed intense impulsive loading is given. For the materials for which data currently exists, no strain-rate effects are observed on yield (i.e. two aluminum alloys) and the strain-rate

3. Pressure studies
I. AFSC Project 6906.
Task 690601
II. Contract AF 33
(616)-6373
III. Massachusetts Institute of Technology, Cambridge, Mass.

3. Pressure studies
I. AFSC Project 6906.
Task 690601
II. Contract AF 33
(616)-6373
III. Massachusetts Institute of Technology, Cambridge, Mass.

3. Pressure studies
I. AFSC Project 6906.
Task 690601
II. Contract AF 33
(616)-6373
III. Massachusetts Institute of Technology, Cambridge, Mass.

IV. W. Herrmann, et al.
V. Aval fr OTS
VI. In ASTIA collection

(over)

(over)

(over)

(over)